

**High-precision Strontium Isotope Measurements**  
—  
**From the Early Solar System to the Age of the Moon**

Dissertation

Zur Erlangung des mathematisch-naturwissenschaftlichen Doktorgrades

"Doctor rerum naturalium"

der Georg-August-Universität Göttingen  
im Promotionsstudiengang Geowissenschaften  
der Georg-August University School of Science (GAUSS)

vorgelegt von

**Jonas Michel Schneider**

aus Stralsund

Göttingen, 2024

### Betreuungsausschuss

Prof. Dr. Thorsten Kleine

Abteilung Planetenwissenschaften, Max-Planck-Institut für Sonnensystemforschung, Göttingen

Dr. Christoph Burkhardt

Abteilung Planetenwissenschaften, Max-Planck-Institut für Sonnensystemforschung, Göttingen

Prof. Dr. Andreas Pack

Abteilung Geochemie und Isotopengeologie, GZG, Georg-August-Universität Göttingen

### Mitglieder der Prüfungskommission

Prof. Dr. Thorsten Kleine

Abteilung Planetenwissenschaften, Max-Planck-Institut für Sonnensystemforschung, Göttingen

Prof. Dr. Andreas Pack

Abteilung Geochemie und Isotopengeologie, GZG, Georg-August-Universität Göttingen

Weitere Mitglieder der Prüfungskommission:

Prof. Dr. Matthias Willbold

Abteilung Geochemie und Isotopengeologie, GZG, Georg-August-Universität Göttingen

Prof. Dr. Doris Breuer

Abteilung Planetenphysik, Deutsches Zentrum für Luft- und Raumfahrt e.V. (DLR), Berlin

Dr. Thomas S. Kruijer

Division of Cosmochemistry and Nuclear Forensics, Lawrence Livermore National Laboratory,

Livermore, California, U.S.A

Dr. Christoph Burkhardt

Abteilung Planetenwissenschaften, Max-Planck-Institut für Sonnensystemforschung, Göttingen

Tag der mündlichen Prüfung: 19.06.2024





# Abstract

Variations in the isotopic composition of extraterrestrial rocks provide crucial information about the nature and evolution of planetary building blocks, the Earth, and the Moon. In this thesis, strontium isotopic compositions of terrestrial rocks, meteorites, and lunar samples are used to investigate the origin of isotope anomalies in solar system materials as well as the time of Moon formation. For this purpose, a multi-dynamic method for strontium (Sr) isotope measurements using thermal ionization mass spectrometry (TIMS) was set up, which enables measurement of all four stable Sr isotopes ( $^{84}\text{Sr}$ ,  $^{86}\text{Sr}$ ,  $^{87}\text{Sr}$ ,  $^{88}\text{Sr}$ ) with higher precision than traditional static measurements.

The first part of this thesis investigates the effect of Faraday cup deterioration by thermal ionization mass spectrometry. TIMS measurements are widely used to measure  $^{84}\text{Sr}$  and  $^{87}\text{Sr}$  variations in geological samples. Therefore, a thorough understanding of analytically induced uncertainties is important. The study reveals that dynamic measurement routines yield more consistent, precise, and accurate results than traditional static routines and further demonstrates that previously observed residual correlations in static chromium isotope data might largely result from cup aging in TIMS instruments.

In the second part of the thesis, the established dynamic measurement routines are used to assess the distribution of nucleosynthetic  $^{84}\text{Sr}$  anomalies (expressed as  $\mu^{84}\text{Sr}$ ) among meteorites, Earth, Mars, and the Moon. Nucleosynthetic isotope anomalies in meteorites reveal a dichotomy between the non-carbonaceous (NC) and carbonaceous (CC) meteorite reservoirs, but its origin remains debated. It either reflects the thermal processing of presolar dust or an inherited heterogeneity from the parental molecular cloud. Previous  $\mu^{84}\text{Sr}$  data was interpreted to represent thermal processing of presolar grains based on small differences among and between NC and CC meteorites. However, the precision and number of samples in previous studies do not allow this conclusion to be drawn unequivocally. In addition, the thermal processing origin of  $^{84}\text{Sr}$  anomalies is difficult to reconcile with nucleosynthetic isotope anomalies observed in other elements. The new  $\mu^{84}\text{Sr}$  data reveals that the inner solar system, represented by NC meteorites, Mars, Earth, and the Moon,

displays a remarkable homogeneity in  $^{84}\text{Sr}$  anomalies. Moreover, the NC and CC reservoirs are not clearly separated as observed for other elements. This study shows that counterbalancing nucleosynthetic contributions from *s*-, *r*-, and *p*- process isotopes are the reason for this homogeneity in the inner solar system and for the absence of a clear NC-CC separation. The characteristic  $^{84}\text{Sr}$ -excess observed in the CC-reservoir is balanced by *s*-process variations for NC samples. Collectively, the antagonistic *s*-, *r*-, and *p*-process variations argue against the thermal processing of presolar dust as the origin of Sr isotope anomalies among meteorites and planets. They instead support an initial isotopic heterogeneity of the solar system accretion disk as the origin for the NC-CC dichotomy.

The last part of this thesis focuses on the Moon and how strontium isotopes can be used to unravel the timing of Moon's formation. The Moon formed in the aftermath of a giant impact of the proto-planet Theia onto proto-Earth, which marks the final step in Earth's accretion and thus the beginning of the Earth as a habitable planet. Despite its importance, the age of the Moon is one of the biggest uncertainties in lunar research and a variety of methods including radiogenic dating of lunar rocks or thermochemical and dynamical modelling yield conflicting results for the time of the giant impact and the subsequent solidification of the lunar magma ocean (LMO).

The solidification timescale of the LMO and the age of the moon can potentially be inferred from the age of lunar ferroan anorthosites (FANs). The new high-precision  $^{87}\text{Sr}/^{86}\text{Sr}$  data for FANs presented here reveal that all investigated lunar FANs share the same formation age of  $4.360 \pm 0.028$  billion years (Ga) ago. However, this age does not necessarily equal the age of the Moon itself. Independently from the absolute age, these samples are used to derive a new and precise initial  $^{87}\text{Sr}/^{86}\text{Sr}$  ratio for the Moon, which is now based on five FANs instead of only one as in previous studies. This ratio is then used to calculate new Rb-Sr model ages for the age of the Moon within the framework of newer impact scenarios and including all possible uncertainties. Consistent with independently derived results from radiometric dating of zircons, constraints from Hf-W, and numerical modeling, these new model calculations result in a consistent Rb-Sr model age for the Moon of  $\sim 4.5$  Ga.

# Kurzfassung

Unterschiede in der Isotopenzusammensetzung von extraterrestrischen Gesteinen liefern wichtige Informationen über die Entwicklung der planetaren Bausteine, der Erde und des Mondes. In dieser Arbeit wurde die Strontium-Isotopenzusammensetzung von terrestrischen Gesteinen, Meteoriten und Mondproben ermittelt. Dies ermöglicht es den Ursprung von Isotopenanomalien in Materialien des Sonnensystems sowie den Zeitpunkt der Mondbildung zu untersuchen. Zu diesem Zweck wurde eine multidynamische Messmethode mittels thermischer Ionisationsmassenspektrometrie (TIMS) aufgesetzt, die die Messung aller vier stabilen Sr-Isotope ( $^{84}\text{Sr}$ ,  $^{86}\text{Sr}$ ,  $^{87}\text{Sr}$ ,  $^{88}\text{Sr}$ ) mit wesentlich höherer Präzision ermöglicht als herkömmliche statische Messungen.

Der erste Teil dieser Doktorarbeit befasst sich mit der Untersuchung der analytischen Unsicherheiten, die durch die Abnutzung der ‚Faraday Cups‘ bei statischen TIMS-Messungen verursacht werden. Diese Methode wird häufig angewandt, um  $^{84}\text{Sr}$ - und  $^{87}\text{Sr}$ -Isotopenvariationen in geologischen Proben zu bestimmen. Daher ist ein Verständnis von analytischen Methoden und damit verbundener Unsicherheiten wichtig. Die Studie zeigt, dass dynamische Messroutinen besser vergleichbare und präzisere Ergebnisse liefern und dass zuvor beobachtete residuale Korrelationen in Chrom-Isotopendaten zu einem großen Teil auf die Alterung der ‚Faraday Cups‘ in TIMS-Instrumenten zurückzuführen sein könnten.

Im zweiten Teil der Arbeit werden die dynamischen Messroutinen verwendet, um die Verteilung der nukleosynthetischen  $^{84}\text{Sr}$ -Anomalien ( $\mu^{84}\text{Sr}$ ) in Meteoriten, dem Mars, der Erde und dem Mond zu untersuchen. Nukleosynthetische Isotopenanomalien in Meteoriten zeigen eine Dichotomie zwischen den ‚nicht-kohligen‘ (engl. non-carbonaceous: ‚NC‘, repräsentativ für das innere Sonnensystem) und ‚kohligen‘ (engl. carbonaceous: ‚CC‘, repräsentativ für das äußere Sonnensystem) Meteoritenreservoirs, dessen Ursprung jedoch umstritten ist. Diese Dichotomie ist entweder das Resultat thermischer Prozessierung von präsolarem Staub oder einer vererbten Heterogenität aus der ursprünglichen Molekülwolke. Frühere  $\mu^{84}\text{Sr}$ -Daten wurden dahingehend interpretiert, dass die Dichotomie die thermische Verarbeitung präsolarer Körner reflektiert, da sie geringe

$\mu^{84}\text{Sr}$ -Unterschiede innerhalb und zwischen dem NC- und CC-Reservoir aufzeigten. Die Genauigkeit und die Anzahl der Proben in früheren Studien lassen jedoch keine eindeutige Schlussfolgerung zu. Darüber hinaus lässt sich ein Ursprung der  $\mu^{84}\text{Sr}$ -Anomalien in Meteoriten durch thermische Prozessierung nur schwer mit nukleosynthetischen Isotopenanomalien anderer Elemente vereinbaren. Die neuen  $\mu^{84}\text{Sr}$ -Daten zeigen, dass alle NC-Meteorite, Mars, Erde, Mond und demnach das gesamte innere Sonnensystem durch eine bemerkenswerte  $\mu^{84}\text{Sr}$ -Homogenität charakterisiert ist. Außerdem sind die NC- und CC-Reservoirs nicht klar voneinander getrennt, wie dies bei anderen Elementen beobachtet wird. Diese Studie zeigt, dass sich ausgleichende nukleosynthetische Beiträge von *s*-, *r*- und *p*-Prozess Isotopen der Grund für die Homogenität im inneren Sonnensystem und das Fehlen einer klaren NC-CC-Trennung sind. Der charakteristische  $^{84}\text{Sr}$ -Überschuss, der sich im CC-Reservoir zeigen lässt, wird durch *s*-Prozess-Variationen in NC-Proben ausgeglichen. Zusammengefasst sprechen die gegensätzlichen *s*-, *r*- und *p*-Prozessvariationen gegen eine thermische Prozessierung von präsolarem Staub als Ursprung der Sr-Isotopenanomalien. Stattdessen sprechen sie für eine inhärente isotopische Heterogenität der Akkretionsscheibe des Sonnensystems als Ursache für die NC-CC-Dichotomie.

Der letzte Teil dieser Arbeit befasst sich mit der Entstehung des Mondes und damit, wie Strontiumisotope genutzt werden können, um das Alter des Mondes zu entschlüsseln. Der Mond entstand als Folge eines gigantischen Impakts des Protoplaneten Theia auf die Proto-Erde. Dieser gigantische Einschlag kann somit als letzter Schritt in der Akkretion der Erde angesehen werden und markiert somit auch den Beginn der Erde als bewohnbaren Planeten. Der Zeitpunkt dieses Impakts (und damit das Alter des Mondes) ist jedoch eine der größten Unsicherheiten in der Mondforschung und verschiedenste Methoden, wie die radiometrische Datierungen von Mondgestein oder thermochemische und dynamische Modellierungen liefern widersprüchliche Ergebnisse für den Zeitpunkt des letzten großen Impakts und der anschließenden Kristallisierung des lunaren Magmaozeans (LMO).

Die relativen Zeitskalen des LMO, sowie das Alter des Mondes können theoretisch aus den Altern von lunaren eisenreichen Anorthositen (engl. ferroan anorthosites: FANs) abgeleitet werden. In dieser Doktorarbeit werden neue hochpräzise  $^{87}\text{Sr}/^{86}\text{Sr}$ -Daten für

FANs vorgestellt, die zeigen, dass alle untersuchten lunaren FANs das gleiche Bildungsalter von  $4,360 \pm 0,028$  Milliarden Jahren haben. Dieses Alter entspricht jedoch nicht unbedingt dem Alter des Mondes selbst, wie neue Rb-Sr Modellalter zeigen. Unabhängig vom absoluten Alter werden die neuen Daten verwendet, um ein neues, präzises initiales  $^{87}\text{Sr}/^{86}\text{Sr}$  Verhältnis des Mondes zu bestimmen. Dieser Wert basiert hierbei auf fünf Proben, anstatt wie bisher nur auf einer Probe, und wird zur Berechnung neuer Rb-Sr-Modellalter für das Alter des Mondes im Rahmen neuerer Einschlagszenarien und unter Berücksichtigung aller möglichen Unsicherheiten verwendet. In Übereinstimmung mit unabhängig voneinander abgeleiteten Ergebnissen aus der radiometrischen Datierung von Zirkonen, Ergebnissen aus Hf-W-Studien und numerischer Modellierung führen diese neuen Modellrechnungen zu einem konsistenten Rb-Sr-Modellalter für den Mond von  $\sim 4,5$  Milliarden Jahren.



# Table of Content

<b>Abstract</b>	<b>5</b>
<b>Kurzfassung</b>	<b>7</b>
<b>1. Introduction</b>	<b>15</b>
<b>1.1. From the start of the solar system to the formation of the Earth</b>	<b>16</b>
<b>1.2. Isotope anomalies in meteorites</b>	<b>17</b>
1.2.1 Meteorites as a window to the past	17
1.2.2 The meteorite dichotomy and its implications for early solar system dynamics	19
<b>1.3. The origin of the Earth-Moon system</b>	<b>22</b>
1.3.1 The origin of the Moon in a giant impact	22
1.3.2 The lunar magma ocean and the age of the Moon	24
<b>1.4. Strontium isotope cosmochemistry</b>	<b>26</b>
1.4.1 Nucleosynthetic Sr isotope anomalies	27
1.4.2 Radiogenic Sr isotope variations	29
<b>1.5. Objectives of the thesis</b>	<b>32</b>
<b>2. Effects of Faraday cup deterioration on Sr and Cr isotope analyses by thermal ionization mass spectrometry</b>	<b>35</b>
<b>Abstract</b>	<b>35</b>
<b>2.1. Introduction</b>	<b>36</b>
<b>2.2. Materials and Methods</b>	<b>37</b>
2.2.1 Materials and standards	37
2.2.2 Instrumental setup and measurement series	37
2.2.3 Strontium isotope measurements	38
2.2.4 Chromium isotope measurements	41
<b>2.3. Results and Discussion</b>	<b>42</b>
2.3.1 Effects of cup deterioration on Sr isotope measurements	42
2.3.2 Effects of cup deterioration on Cr isotope measurements	46
<b>2.4. Conclusions</b>	<b>51</b>
<b>3. Distribution of s-, r-, and p-process nuclides in the early solar system inferred from Sr isotope anomalies in meteorites</b>	<b>53</b>
<b>Abstract</b>	<b>53</b>
<b>3.1. Introduction</b>	<b>54</b>
<b>3.2. Samples and analytical methods</b>	<b>56</b>

<b>3.3. Nucleosynthetic Sr isotope variations among meteorites</b>	<b>57</b>
<b>3.4. Origin of <sup>84</sup>Sr variations in the solar system</b>	<b>61</b>
3.4.1 <sup>84</sup> Sr homogeneity of the inner solar system	61
3.4.2 <sup>84</sup> Sr offset between NC and CC meteorites	65
3.4.3 Origin of <sup>84</sup> Sr variations among carbonaceous chondrites	66
<b>3.5. Implications for the origin of nucleosynthetic variability in the disk</b>	<b>67</b>
<b>3.6. Appendix Chapter 3</b>	<b>69</b>
<b>4. Strontium isotope evidence for formation of the Moon ~ 4.5 billion years ago</b>	<b>71</b>
<b>Abstract</b>	<b>71</b>
<b>4.1. Introduction</b>	<b>72</b>
<b>4.2. Results</b>	<b>74</b>
<b>4.3. Discussion</b>	<b>77</b>
<b>4.4. Materials and Methods</b>	<b>85</b>
4.4.1 Sample preparation and chemical separation	85
4.4.2 Rb-Sr isotope measurements	87
4.4.3 Rb-Sr age in case of Earth-Moon equilibration	87
4.4.4 Rb-Sr age in non-equilibrium models	88
4.4.5 Choice of parameters for model age calculations	90
<b>4.5. Appendix Chapter 4</b>	<b>93</b>
<b>5. Synthesis and Outlook</b>	<b>101</b>
<b>References</b>	<b>105</b>
<b>List of Figures</b>	<b>116</b>
<b>List of Tables</b>	<b>119</b>
<b>Declaration of Author Contributions</b>	<b>121</b>
<b>Acknowledgements</b>	<b>123</b>
<b>Curriculum Vitae</b>	<b>125</b>





# 1. Introduction

Understanding our origin and place in the universe is a basic human need. This curiosity and intrinsic desire for knowledge is why we study the cosmos with telescopes and space probes and why we sent astronauts to the Moon. By exploring the isotopic composition of the extraterrestrial samples brought by such missions, as well as by looking at meteorites invaluable information about the dynamics and chronology of the solar system's evolution can be obtained. For instance, small variations in the isotopic makeup of meteorites tracing back to the forging of elements in previous star generations enable us to investigate the evolution and dynamics within the disk of gas and dust from which our solar system emerged. Likewise, isotopic variations induced by radioactive decay systems allow us to study chronological aspects of solar system formation and evolution, like the timing of planetary accretion and the subsequent differentiation of planets into core, mantle, and crust.

Despite > 60 years of research and significant progress, some key issues about the formation and evolution of the solar system and the Earth remain poorly understood. By obtaining new high-precision strontium isotope data of a comprehensive set of meteorites and lunar samples from the Apollo missions, this thesis aims to provide novel insights into two of such issues, namely (i) the mixing and processing of dust in the solar accretion disk and (ii) the age of the Moon. The following introductory chapter provides an overview of the fundamental concepts behind these research topics and is organized as follows: After a broad overview of the solar system and planet formation (1.1), the research topics of this thesis are introduced, which occupy isotope anomalies in meteorites (1.2) as well as the origin and age of the Moon (1.3). Then, the use of Sr isotopes in the context of the two research topics is explained (1.4) and finally, the objectives of this thesis are presented (1.5).

## 1.1. From the start of the solar system to the formation of the Earth

In the beginning of our solar system, 4.567 billion years ago, the center of a molecular cloud collapsed, whose chemical and isotopic composition was the result of  $\sim 9$  billion years of galactic chemical evolution (Bouvier and Wadhwa, 2010; Frebel, 2014). A part of this initial molecular cloud became gravitationally unstable and collapsed within itself, forming the proto-Sun at its center. By conservation of angular momentum, a fast-rotating disk of gas and dust (the solar nebula) formed, through which the proto-Sun accreted further mass from the infalling cloud (Greaves, 2005). At the end of the infall, a fraction of mass survived in the disk and served as the building material for planetesimals and protoplanets. These protoplanets are formed in three general stages (Chambers et al., 2014). Initially,  $\mu\text{m}$ -sized dust agglomerated into bigger-sized particles until they reached the size of sub-mm to cm-sized pebbles. In streaming instabilities in the disk, some of the dust and pebbles then got enriched and gravitationally collapsed into 10-100 km-sized planetesimals (Youdin and Goodman, 2005; Johansen and Youdin, 2007). In a second stage, these planetesimals grew by mutual collisions into Moon- to Mars-sized protoplanets. The timescales for these first steps seem to be very fast, and several studies have revealed that planetesimals and planets began to form within the first million years of solar system history (Spitzer et al., 2021; Kruijer et al., 2017). Many of these early-formed planetesimals experienced melting and differentiation through the radioactive decay of short-lived radioactive isotopes (e.g.,  $^{26}\text{Al}$ ) while later-formed planetesimals often consist of unprocessed material and hence can be understood as agglomerates of primitive disk materials. There is no consensus on how exactly the final step of planet formation proceeds, and there seem to be multiple possible pathways. However, at least in the formation region of the terrestrial planets, there is evidence that the protoplanets grew further on a more protracted timescale of tens of millions of years by giant collisions among each other, causing destruction and sometimes global melting. The Earth-Moon system is thought to represent the most prominent example of such a late-stage giant impact event, as it is assumed that the Moon formed from the debris of the impact of a protoplanet and the proto-Earth (Warren, 1985; Canup and Asphaug, 2001). The formation of the Moon therefore marked the end of Earth's accretion and set the stage for its evolution to the habitable planet it is today.

## 1.2. Isotope anomalies in meteorites

### 1.2.1 Meteorites as a window to the past

While most of the matter from the earliest stage of solar system history is lost to the Sun or is incorporated in the planetary bodies and therefore inaccessible, some planetesimals escaped planetary accretion and survived in the orbital area between Mars and Jupiter known as the asteroid belt. Pieces of these objects sometimes arrive on the surface of the Earth and are then known as meteorites. Meteorites can be seen as solar fossils and provide a snapshot of the dust in the solar nebula at the time and place of the formation of their parent bodies. Hence, they are of fundamental importance to investigate the chemical and dynamical properties of the early solar system (Chapter 3).

Different classification schemes have been proposed based on chemical, petrological, or isotopic characteristics (Bischoff, 2001; Weisberg et al., 2006). In general, meteorites can be divided into two groups: The first is undifferentiated meteorites that have never been heated over 900 °C and have therefore never been fully molten. Thereby, they still contain more or less unaltered nebular material. These meteorites are also called ‘chondrites’. The second group is differentiated meteorites, which stem from bodies that experienced melting and are therefore chemically differentiated and evolved (Fig. 1).

### Classification of meteorites

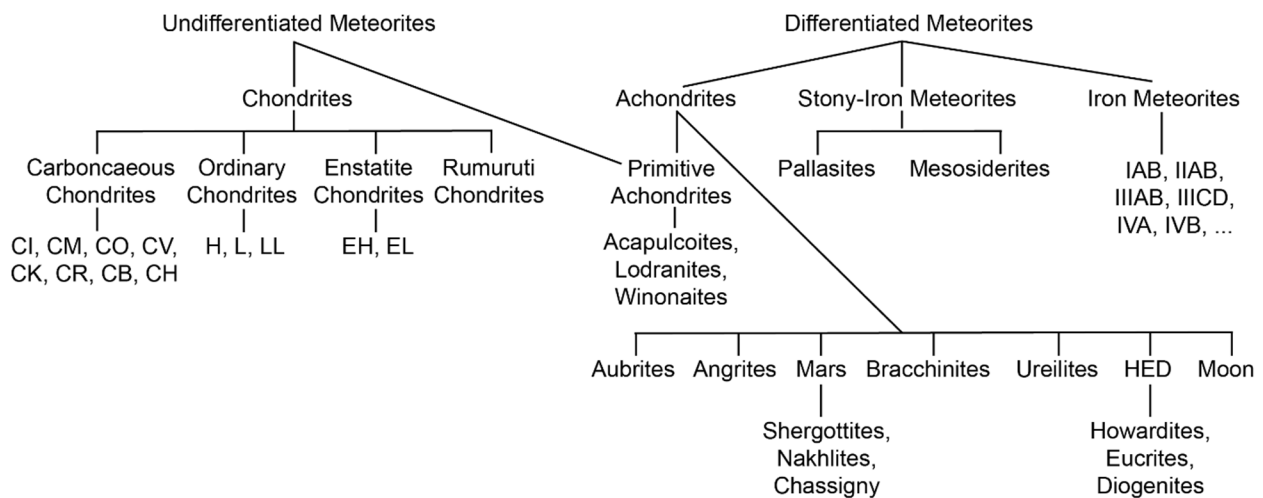


**Figure 1:** Meteorite classification scheme after Bischoff (2001).

Each subgroup of undifferentiated and differentiated meteorites within the meteorite classification is based on unique chemical and petrological features and is believed to sample one distinct parent body. However, some subgroups belong to the same parent body and sample different lithologies of Mars, Vesta, and the Moon.

Chondrites provide the unique opportunity to investigate primitive material that formed in the protoplanetary disk. They consist mainly of silicate spherules called chondrules, a fine-grained matrix, some iron-nickel metal bits, and refractory inclusions, which occur in different assemblages in each chondrite group (Scott, 2007). The eponymous chondrules are sub-mm to cm-sized and have once been free-floating melt droplets, which may have directly formed from transient heating of dust in the solar nebula (Scott, 2007; Russell et al., 2018). Refractory inclusions, namely amoeboid olivine aggregates (AOAs) and calcium-aluminum-rich inclusions (CAIs) have a mineralogy matching the predictions for the first condensates forming from a cooling gas of solar composition (Grossman, 1972). With an age of  $4,567.30 \pm 0.16$  million years (Ma) CAIs are the oldest dated objects formed in the solar system (Bouvier and Wadhwa, 2010; Connelly et al., 2012). The various components are held together in a fine-grained matrix, which often experienced secondary processing such as alteration and metamorphism (McSween and Richardson, 1977; Huss et al., 1981; Zolensky et al., 1993). Additionally, the matrix hosts occasional presolar grains, which have distinct chemical and isotopic characteristics that allow to identify them as extrasolar material from the interstellar medium dispersed in the solar nebula and caught in the meteorite matrix (Hoppe and Zinner, 2000; Lodders and Amari, 2005).

Collectively, the different meteorite groups provide samples from a wide range of early solar system materials. From the first solar nebula condensates, through cosmic sediments from accretionary leftovers, to planetesimal cores and crustal samples from other celestial bodies, such as Martian, Vestian, or lunar meteorites. Thus, meteorites give the unique opportunity to study the history of our solar system and open up a window to the past, that would otherwise remain closed.

### 1.2.2 The meteorite dichotomy and its implications for early solar system dynamics

Meteorites are not only distinct in their petrographic features but can also be classified and investigated using isotope anomalies among bulk meteorites and their components. These nucleosynthetic isotope anomalies originate from the heterogeneous distribution of presolar phases from different stellar environments in the solar nebula (Poole, 2013; Kleine et al., 2020). Based on differences in nucleosynthetic anomalies, it was found that meteorites display a ubiquitous isotopic dichotomy, which led to the genetic classification of meteorites into non-carbonaceous (NC) and carbonaceous (CC) supergroups (Warren, 2011). The dichotomy is visible in the isotope composition of elements with different cosmochemical and geochemical affinities (e.g., Ca, Cr, Ti, Ni, Zn, Sr, Mo, Zr, and Ru). However, it is best to be seen when isotopic anomalies of different elements are compared in multi-isotope space, which is exemplarily shown for  $\epsilon^{54}\text{Cr}$  versus  $\epsilon^{50}\text{Ti}$  as displayed in Figure 2 (Trinquier et al., 2009; Warren, 2011).

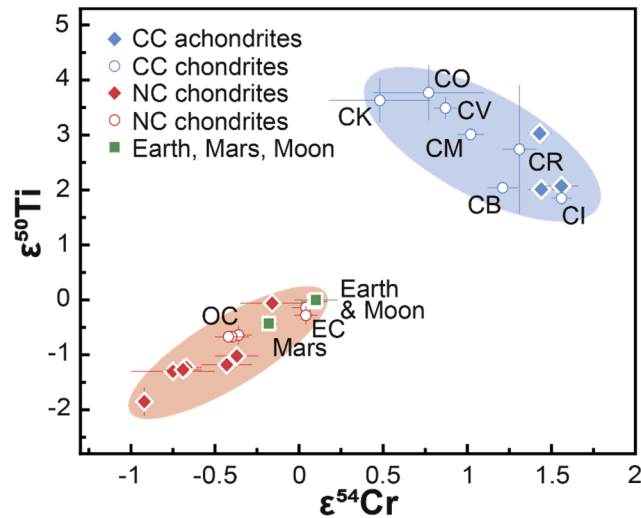


**Figure 2:** Plot of  $\epsilon^{54}\text{Cr}$  versus  $\epsilon^{50}\text{Ti}$  displaying the NC-CC dichotomy (Warren, 2011). Figure modified from Kleine et al. (2020).

Similar observations can be made from plots of e.g.,  $\epsilon^{48}\text{Ca}$  vs.  $\epsilon^{96}\text{Zr}$ ,  $\epsilon^{62}\text{Ni}$  vs.  $\epsilon^{100}\text{Ru}$ , or  $\epsilon^{54}\text{Cr}$  vs.  $\epsilon^{94}\text{Mo}$  (Burkhardt et al., 2021). An important feature of the dichotomy is the existence of a gap between the NC and CC reservoirs in multi-isotope space and the fact that both reservoirs contain differentiated and undifferentiated meteorites. This implies that the separation of the reservoirs has a spatial origin and lasted at least one million years, possibly due to the early growth of Jupiter (Warren, 2011; Kruijer et al., 2017; Kruijer et al., 2020).

The ultimate origin of the isotopically distinct reservoirs in the disk is debated. Current hypotheses mainly favor two different approaches. The dichotomy could be the result of thermal processing of presolar phases in the nebular phase of the protoplanetary disk (Trinquier et al., 2009; Paton et al., 2013; Van Kooten et al., 2016; Poole et al., 2017). Different locations in the solar nebular would therefore experience different degrees of thermal processing and hence result in an isotopic gradient varying with distance to the Sun. This explanation, however, is difficult to reconcile with the co-occurrence of the isotopic dichotomy in elements with fundamentally different nucleosynthetic heritage, chemical properties, and geochemical affinities (Burkhardt et al., 2019; Jacquet et al., 2019; Nanne et al., 2019). For instance, the dichotomy is evident in isotopes of Zn, which is a lithophile volatile element, as well as in isotopes of Ru, which is a refractory highly siderophile element (Steller et al., 2023; Hopp et al., 2020). Thus, thermal processing would have had to affect carrier phases with completely different thermochemical properties selectively.

Hence, an alternative scenario explains the origin of the dichotomy as a change in isotopic composition during the initial infall of the molecular cloud on the disk (Burkhardt et al., 2019; Nanne et al., 2019, Fig. 3). While the early infall was characterized by a CAI-like composition ('enriched in supernova-derived nuclides') and material was transported outwards due to viscous expansion of the disk, the later infall had an NC-like isotopic composition ('depleted in supernova-derived nuclides'). This was then mixed progressively with the already existing material (Fig. 3). By this, intermediate compositions between the isotopic endmembers were created, which ultimately resulted in the typical NC and CC isotopic reservoirs. The reservoirs were then separated and prevented from progressive homogenization by a physical barrier. While the early formation of Jupiter is a likely candidate for such a barrier (Kruijer et al., 2017), the location of the water-snow line, a

pressure maximum in the disk, or a combination of these could also account for the early separation of NC and CC materials (Brasser and Mojzsis, 2020; Lichtenberg et al., 2021). Because of orbital resonances and planet migration, outer solar system bodies were later scattered to the inner solar system (Walsh et al., 2011; Raymond and Morbidelli, 2014), where they probably contributed to the volatile budget of inner solar system bodies and planets (Budde et al., 2019; Steller et al., 2023).

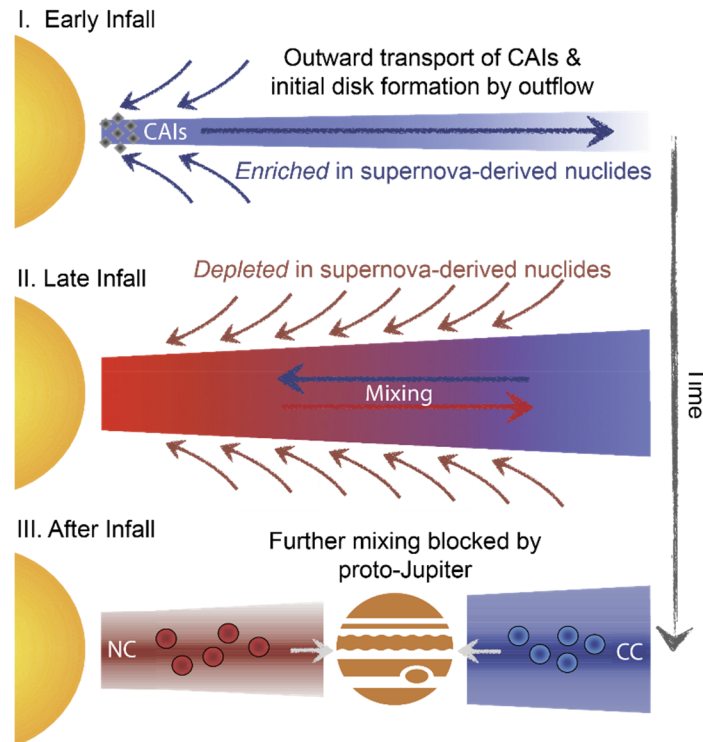


**Figure 3:** Qualitative model of the dynamical evolution of the early solar nebula that explains the relative observations from nucleosynthetic isotope variations in meteorites. Figure modified from Nanne et al. (2019).

The meteorite dichotomy demonstrates that nucleosynthetic isotope anomalies can be used to, for example, investigate dynamic processes in the early solar system and the formation locations of planetary building blocks. As such, meteorites can be utilized to investigate the origin of the Earth. However, the origin of the Earth is closely related to the formation of the Moon, because the Moon-forming impact marks the end of Earth's accretion and might have played a substantial role in the history of Earth's volatile budget and orbital evolution, both of which are crucial for making the Earth a habitable planet.

### 1.3. The origin of the Earth-Moon system

The Earth-Moon system is special compared to other planet-satellite pairs in the solar system. The Moon's size is large for an Earth-sized planet, and the angular momentum of the Earth-Moon system is comparably high (Canup et al., 2023). The Moon strongly affects the Earth by dictating the tides and stabilizing its spin axis, which thus directly influences the rhythm of life on Earth. Without the Moon the Earth might have never become a habitable planet (Nakajima et al., 2022). Consequentially, the origin, timing, and formation history of the Moon remains an intense area of scientific research. During the last 60 years of scientific lunar research, beginning with the Apollo program, substantial advances in understanding the Moon through remote sensing via spacecrafts, numerical modeling, and sample-based science from returned lunar samples were made. However, basic questions like *how* and *when* Earth's celestial companion formed are still not satisfactorily answered.

#### 1.3.1 The origin of the Moon in a giant impact

Constraining the age of the Moon is firmly connected to the question of how the Moon formed in the first place. Theories of lunar origin involve scenarios in which the Moon could be a captured planetesimal (See, 1909; Urey, 1952), was created by fission of a fast-spinning proto-Earth (Darwin, 1879; Wise, 1963), or simply co-accreted with Earth in a nearby orbit (Morishima and Watanabe, 2001). Consensus arose with the hypothesis of an origin of the Moon by a highly energetic giant impact of a roughly Mars-sized object called 'Theia' on proto-Earth (Hartman and Davis, 1975; Cameron and Ward, 1976; Canup and Asphaug, 2001). This allows to explain several key features of the Earth-Moon system, such as the system's angular momentum, the mass and core-size distribution, the Moon's depletion of volatile elements, and a hot start for the Moon as required by sample petrology (see reviews by Canup et al., 2023; Gaffney et al., 2023). However, this 'canonical' giant impact hypothesis predicts the Moon to have formed mainly from impactor material (Canup, 2014). This is difficult to reconcile with the observation of a striking isotopic similarity between Earth and the Moon because the mass-independent isotopic signatures would be expected to differ for Theia and proto-Earth (as they, for instance, differ between Earth and Mars). An isotopic similarity was first observed for oxygen isotopes (Clayton and Mayeda, 1975), and while

newer work might suggest tiny lithology-dependent differences of a few parts per million (ppm) (Herwartz et al., 2014; Cano et al., 2020), a general similarity was subsequently confirmed by multiple studies measuring oxygen isotopes on lunar and terrestrial samples with increasing precision (e.g., Wiechert et al., 2001; Young et al., 2016; Fischer, 2021). Additional studies of lunar rocks extended this common isotopic composition to chromium (Qin et al., 2010; Mougél et al., 2018), titanium (Zhang et al., 2012), calcium (Schiller et al., 2018), strontium (Schneider et al., 2023, Chapter 3 of this thesis), or tungsten (Kruijer et al., 2015; Touboul et al., 2015).

To explain these geochemical constraints together with the physical constraints, the giant impact models had to be customized and developed further. Newer, reasonably successful models propose scenarios such as canonical giant impacts into a terrestrial magma ocean (Hosono et al., 2019) and hit-and-run collisions with larger mass impactors (Reufer et al., 2012; Canup, 2012). In general, high angular momentum and high energy impacts (such as the half Earth scenario or fast-spinning Earth scenario) seem to be more successful in reproducing the observed physical, chemical, and isotopic constraints (Canup, 2012; Ćuk and Stewart, 2012; Lock et al., 2018). Some of these newer scenarios involve large-scale vaporization of the impactor-proto-Earth system and the subsequent condensation of the material, ultimately forming the Moon in post-impact high-T state termed ‘synestia’ (Lock et al. 2018). Whereas the canonical giant impact scenario has difficulties in accounting for geochemical key observations, the likelihood of these more ‘extreme’ scenarios is debated (see review by Canup et al., 2023). In general, the isotopic similarity would be easiest reconciled with the Moon primarily formed from Earth’s mantle and/or if Theia had an Earth-like isotopic composition (Dauphas et al., 2014a), although this scenario might be difficult to account for the observed  $\epsilon^{182}\text{W}$  values for Earth and Moon. Yet, the likelihood of Theia having the same isotopic composition for a range of lithophile to siderophile elements is estimated to be  $< 1\%$  (Canup et al., 2023).

As shown, the details of the Moon-forming impact are still uncertain. However, little doubt exists for the hot start of the Moon from an (almost) completely molten state, as this is required by lunar sample petrology (Gaffney et al., 2023). This first stage after the Moon’s accretion is termed the lunar magma ocean (LMO) and is thought to be a direct result of the

enormous amounts of energy released in a giant impact. As the LMO marks the first stage of lunar evolution, dating the Moon essentially requires dating the LMO and its solidification process.

### **1.3.2 The lunar magma ocean and the age of the Moon**

The Moon is certainly younger than 4.567 Ga, which is the age of the solar system as defined by CAIs (Bouvier and Wadhwa, 2010; Connelly et al., 2012). Whether it is much older than 4.36 Ga, which is the mean age of the oldest lunar rock suites, is under considerable debate (Borg and Carlson, 2023). The bombardment history of the Moon repeatedly modified the initial chemical and isotopic composition of lunar rocks. This complicates traditional isochron dating, as isotope systems can be disturbed (Borg et al., 2015; see section 1.4.2). Whether a sample dated by an isotopic decay system returns a meaningful age depends on the geochemical interpretation of the rock and its formation history. As a consequence, a geological model is needed that puts the formation age of a rock in a geological context. The favored petrological model for the differentiation of the Moon is the lunar magma ocean model.

Soon after their return to Earth, the mineral assemblages found in lunar samples were interpreted as direct crystallization products from sequentially cooling magma (Smith, 1970; Wood, 1970). After metals and siderophile elements sequestered quantitatively into the forming lunar core, the system continuously lost heat to space, and the LMO began to cool down. The solidification of the lunar magma ocean began with core formation and continuously progressed with the crystallization of olivine and orthopyroxene cumulates, which sank to the bottom of the LMO. This buildup of the lunar mantle continued while losing heat to space. When plagioclase began to crystallize after ca. 80% solidification, the buoyant plagioclase crystals floated to the surface and formed an insulating crust (Fig. 4). As a consequence, the heat loss regime changed to conductive heat transfer, which is much less efficient. Hence, further cooling was slowed down significantly.

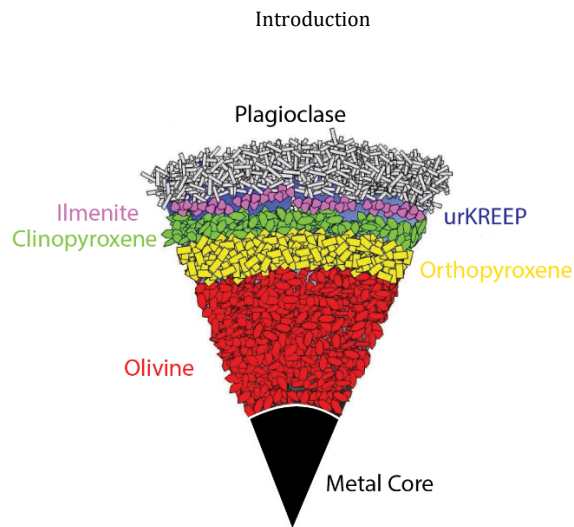


**Figure 4:** Schematic view of the structure of the solidified lunar magma ocean. The plagioclase floatation crust insulated the residual LMO and restrains cooling. Figure modified from Borg and Carlson (2023).

With progressive enrichment in incompatible elements, ilmenite and clinopyroxene crystallized (Fig. 4). As the crystallization sequence approached its end, a residual melt was left behind, which was highly enriched in incompatible elements and is termed urKREEP [uniformly enriched in potassium (K), rare earth elements (REE), and phosphorus (P); (Warren and Wasson, 1979; Warren, 1985; Snyder et al., 1995; Elkins-Tanton et al., 2011; Gaffney et al., 2023)].

The different suites of lunar rocks are testimonies of the sequentially cooled magma ocean. Assuming that the solidification until plagioclase saturation (the first 80% of LMO solidification) happened within a few thousand years (Elkins-Tanton et al., 2011), the age of the earliest lunar crust, represented by ferroan anorthosites (FAN), should in principle represent the age of the Moon. The Mg-suite rocks, which are volcanic products of ilmenite and clinopyroxene cumulate remelting (Prissel et al., 2016), KREEP-rich samples, and lunar zircons should be progressively younger (Borg and Carlson, 2023).

However, 60 years of dating lunar samples and the development of LMO solidification models did not come up with a unifying chronology that aligns both petrologic model constraints and sample ages. On the one hand, models disagree in solidification timescales, which range from 100,000 years (Elkins-Tanton et al., 2011) up to 200 Myr (Maurice et al., 2020) and thus require different geochemical evolution and interpretation of sample ages.

On the other hand, most of the FAN ages are not robust due to disturbances and resetting of the isotopic system by impacts, and the oldest ages are often the most uncertain (Borg et al., 2015). As displayed in Figure 5, reliable FAN ages overlap with the zircon peak age, as well as the KREEP model age, and the oldest Mg-Suite samples (Borg et al., 2011, 2015; Borg and Carlson, 2023). Additionally, the oldest single zircons and zircon spot ages are as old as  $4.417 \pm 0.006$  to  $4.460 \pm 0.031$  Ga (Nemchin et al., 2009; Greer et al., 2023) and are thus predating the oldest crustal ages (Fig. 5). This can hardly be reconciled with the classical LMO solidification model. The timing of lunar crust formation, which would provide the tightest constraints on the age of the Moon is far from clear and explicitly lacks precisely dated anorthosite samples, as these are believed to be the earliest crystallization products of the LMO.

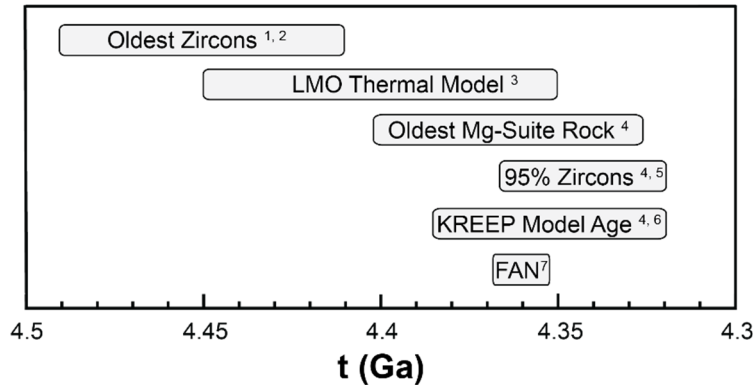


**Figure 5:** Schematic plot of ages for LMO products. References: 1) Nemchin et al. (2009); 2) Greer et al. (2023); 3) Maurice et al. (2020); 4) Borg and Carlson (2023); 5) Taylor et al. (2009); 6) Borg et al. (2015); 7) Borg et al. (2011).

## 1.4. Strontium isotope cosmochemistry

In this thesis, the origin and extent of isotope anomalies among meteorites and the origin of the Moon are investigated using strontium (Sr) isotopes. The diverse characteristics of the different Sr isotopes allow to address multi-faceted questions in cosmochemistry.

In general, there are two basic types of isotope variations: mass-dependent isotope variations and mass-independent isotope variations. As the name suggests, mass-dependent isotope variations are variations where the amount of isotopic fractionation scales with the

mass difference of the isotopes involved (Dauphas and Schauble, 2016). Chemical processes can change the mass-dependent isotopic composition of a sample. By studying those variations, information about chemical processes can be deduced. On the other hand, mass-independent isotope variations are, for example, of radiogenic and nucleosynthetic origin. These two kinds of naturally occurring isotope variations can be used to study early solar system chronology through isotopic dating or gain information about genetic relationships and mixing dynamics in the early solar system, respectively. As these are the tools used in this thesis to study meteorites and the Moon, an introduction to nucleosynthetic and radiogenic isotope variations is given in the following.

#### 1.4.1 Nucleosynthetic Sr isotope anomalies

The elements up until iron (Fe, mass 56) are produced in massive stars by fusion under the consumption of nuclei (carbon- and oxygen-burning in the shells of higher-mass stars). Heavier elements than iron cannot be produced by fusion because iron exhibits the greatest binding energy, and a fusion process would not yield energy after iron fusion. Instead, higher mass elements are created by different nucleosynthetic processes such as the *s*-process, *r*-process, and *p*-process (Burbidge et al., 1957; Käppeler et al., 2011). In the *s*-process ('slow neutron capture'), elements are produced by neutron addition to nuclides and subsequent  $\beta$ -decay in medium neutron density environments such as e.g. asymptotic giant branch (AGB) stars. The *r*-process ('rapid neutron capture') occurs only in extreme neutron density environments such as, e.g., supernovae or neutron star merging events where neutron-rich nuclei at the limit of stability are created by neutron addition to heavier nuclei and then undergo  $\beta$ -decay after the neutron flux ceases. The *p*-process ('proton capture') itself is debated, and the origin of *p*-nuclei is not well constrained. However, extreme neutron flux conditions are required, which might be indicated by the overall rare abundance of *p*-process isotopes (Woosley and Howard, 1978). Newer work also suggests a significant role of the so-called *y*-process (photodisintegration during supernovae core-collapse) as a feasible origin for the synthesis of heavy neutron-deficient isotopes (Roberti et al., 2023).

Strontium has four stable isotopes with different natural abundances:  $^{84}\text{Sr}$  (0.56%),  $^{86}\text{Sr}$  (9.81%),  $^{87}\text{Sr}$  (7.42%), and  $^{88}\text{Sr}$  (82.25%). These are created by the above-mentioned

different nucleosynthetic processes in different stellar environments (Lugaro et al., 2003; Travaglio et al., 2004; Liu et al., 2015; Fig. 5). While  $^{84}\text{Sr}$  is solely produced by the  $p$ -process,  $\sim 80\%$  of  $^{86}\text{Sr}$  and  $^{87}\text{Sr}$  are produced by the  $s$ -process and  $\sim 20\%$  by the so-called *weak s*-process. Additionally, some  $^{87}\text{Sr}$  is produced by the decay of  $^{87}\text{Rb}$  ( $T_{1/2} = 4.976 \times 10^{10}$  years; Fig. 5). Finally, the neutron-rich isotope  $^{88}\text{Sr}$  is produced  $\sim 20\%$  by the  $r$ -process and  $\sim 80\%$  by the  $s$ -process, with minor contributions from the *weak s*-process (Travaglio et al., 2004).

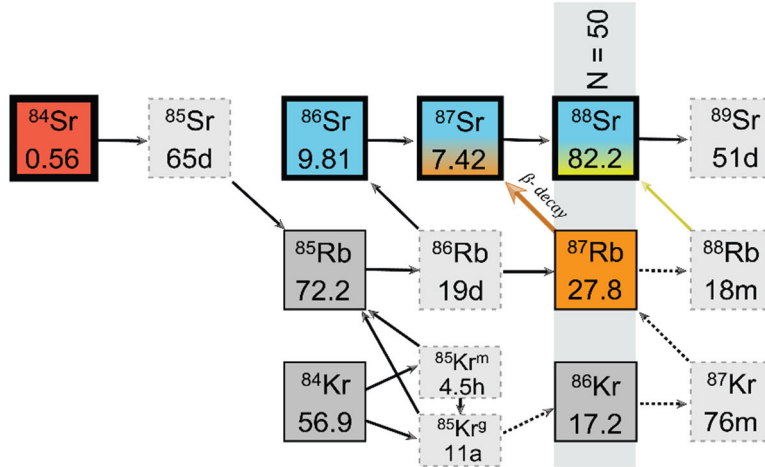


**Figure 5:** The different Sr isotopes are created by different pathways. The  $s$ -process path is shown in bold black arrows, and the main path in dashed lines. Stable isotopes are shown in gray with regular outlines and unstable isotopes with dashed outlines and shaded gray. For Sr, pure  $p$ -process isotopes are shown in red, the  $s$ -process in blue, the  $r$ -process in green, and radioactive decay in orange. Figure modified from Liu et al. (2015).

Nucleosynthetic Sr isotope anomalies among planetary materials are mass-independent isotope variations caused by the heterogeneous distribution of presolar phases from different stellar environments. Among bulk meteorites, these anomalies are inherited from the original material of the parental molecular cloud (Kleine et al., 2020) and are typically very small in comparison to mass-dependent or radiogenic isotope variations. However, with the advent of modern high-resolution multi-collector mass spectrometers like thermal ionization mass spectrometers (MC-TIMS) and inductively coupled plasma mass spectrometers (MC-ICP-MS), it is now possible to resolve differences of only a few parts per million. Nucleosynthetic isotope anomalies are expressed in  $\epsilon$ - or  $\mu$ -notation after internal normalization to a fixed isotope ratio to correct for natural, instrumental, or analytical mass

fractionation. The relative  $\varepsilon$ - or  $\mu$ -notation then describes the deviation of a sample to a standard in parts per ten thousand ( $\varepsilon$ ) or parts per million ( $\mu$ ) according to:

*Equation 1*

$$\mu^{84}\text{Sr} = \left( \frac{\left( \frac{^{84}\text{Sr}}{^{86}\text{Sr}} \right)_{\text{sample}}}{\left( \frac{^{84}\text{Sr}}{^{86}\text{Sr}} \right)_{\text{standard}}} - 1 \right) \times 10^6 .$$

Nucleosynthetic isotope anomalies became of particular importance because they allow to trace provenance, mixing, and transport processes among the earliest solar system objects (e.g., Dauphas, 2002; Trinquier et al., 2009; Burkhardt et al., 2012; Schneider et al., 2020). For instance, based on  $^{84}\text{Sr}$  anomalies ( $\mu^{84}\text{Sr}$ ), it has been argued that the gradient seen for nucleosynthetic anomalies among meteorites is caused by thermal processing of presolar grains (Paton et al., 2013; Moynier et al., 2012). However, whereas  $^{84}\text{Sr}$  anomalies in CAIs have been demonstrated (Charlier et al., 2021; Myojo et al., 2018), it is unclear to what extent  $^{84}\text{Sr}$  anomalies are present in bulk meteorites. Additionally, it is unclear which isotopes are responsible for creating apparent  $\mu^{84}\text{Sr}$  anomalies and how this influences the observed variability in the context of the meteorite dichotomy. Chapter 3 tackles these open questions by investigating the  $\mu^{84}\text{Sr}$ -signatures of inner and outer solar system material with unprecedented precision in a consistent dataset of samples from meteorites, Mars, Earth, and the Moon.

#### 1.4.2 Radiogenic Sr isotope variations

Strontium isotopes not only allow to search for nucleosynthetic isotope variations, but the radioactive decay of  $^{87}\text{Rb}$  to  $^{87}\text{Sr}$  also enables to date geologic events in the early solar system. The  $\beta$ -decay of  $^{87}\text{Rb}$  to  $^{87}\text{Sr}$  has a half-life of 49.67 Ga (Nebel et al., 2011) and therefore results in readily measurable differences in the Sr isotopic composition of  $\sim 4.5$  Ga old samples.

Rubidium (Rb) is a volatile ( $T_c = 800$  K) lithophile element that is highly incompatible, whereas Sr is a refractory ( $T_c = 1464$  K) lithophile element and less incompatible, especially in silica-rich melts (Faure and Powell, 1972; Nebel and Stammer, 2016). Because of their different geochemical affinities, minerals incorporate different amounts of the involved

elements and, therefore, differ in their  $^{87}\text{Rb}/^{86}\text{Sr}$  ratio at the time of crystallization. Measuring  $^{87}\text{Rb}/^{86}\text{Sr}$  and  $^{87}\text{Sr}/^{86}\text{Sr}$  in mineral fractions of a rock allows for the calculation of the crystallization age of this rock as outlined in the following.

The exponential decay of  $^{87}\text{Rb}$  to  $^{87}\text{Sr}$  can be expressed using the general decay equation (equation 2), where  $D^*$  = number of daughter isotopes,  $D_0$  = number of daughter isotopes to begin with,  $P$  = number of parent isotopes,  $\lambda$  = decay constant of  $P$ , and  $t$  = time:

*Equation 2*

$$D^* = D_0 + P \times (e^{\lambda \times t} - 1) .$$

As modern mass spectrometers are designed to measure isotope ratios instead of absolute abundances, it is practical to normalize the involved isotopes to a stable isotope of the same element ( $D_s$ ). As such, equation 2 can be rewritten as follows:

*Equation 3*

$$\frac{D^*}{D_s} = \frac{D_0}{D_s} + \frac{P}{D_s} \times (e^{\lambda \times t} - 1) .$$

In the case of the Rb-Sr chronometer, equation 3 would turn to:

*Equation 4*

$$\left( \frac{^{87}\text{Sr}}{^{86}\text{Sr}} \right)^* = \left( \frac{^{87}\text{Sr}}{^{86}\text{Sr}} \right)_{\text{initial}} + \left( \frac{^{87}\text{Rb}}{^{86}\text{Sr}} \right) \times (e^{\lambda \times t} - 1) .$$

If mineral fractions fall on one line in a plot of  $^{87}\text{Rb}/^{86}\text{Sr}$  vs.  $^{87}\text{Sr}/^{86}\text{Sr}$ , they will form an isochron (a line of the same age, Fig. 6). Equation 4 is linear in the form of  $y = m \times x + b$ , where  $y = ^{87}\text{Sr}/^{86}\text{Sr}$ ,  $m = (e^{\lambda \times t} - 1)$ ,  $x = ^{87}\text{Rb}/^{86}\text{Sr}$ , and  $b = ^{87}\text{Sr}/^{86}\text{Sr}_{\text{initial}}$ . Because  $\lambda$  is a known independently determined value (e.g., Nebel et al., 2011), solving for  $t$  allows to calculate an age for the sample. This requires two assumptions: *i*) The system was in isotopic equilibrium at  $t_0$ . (i.e., all minerals crystallized from the same parental magma source); and *ii*) The system remained closed and undisturbed. This means the system did not exchange parent or daughter isotopes outside the system, as it would be for example the case for remelting, weathering, or thermal metamorphism. Modification of the involved isotope ratios through secondary processes after crystallization would lead to scatter on the isochron or complete resetting of the isotopic system if the system reached equilibrium again.

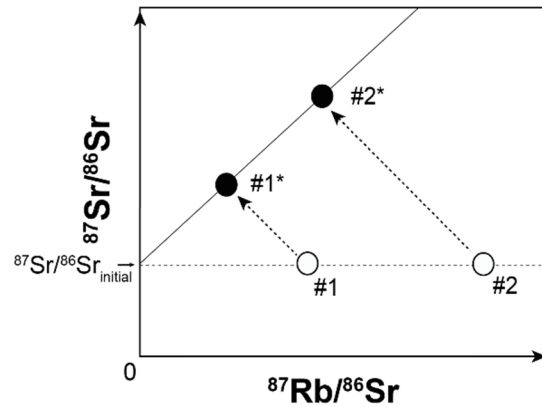


**Figure 6:** Schematic isochron diagram. Different minerals (open circles) evolve with different Rb/Sr ratios and form an isochron as displayed with the filled circles.

Because of its half-life and the relatively high abundance of Sr in lunar highland rocks, strontium isotopes are an especially useful tool for investigating the early history of the Moon. The Rb-Sr system has been widely used to date early solar system objects (Papanastassiou and Wasserburg, 1968) and has been one of the first tools to date lunar rocks returned from the Apollo missions. The isochron ages and low  $^{87}\text{Sr}/^{86}\text{Sr}_{\text{initial}}$  of lunar anorthosites proved the Moon to be extremely old, only slightly younger than the start of the solar system (e.g., Papanastassiou, 1970). This led several authors to use the Rb-Sr system to date lunar rocks, however, it must be noted that the Rb-Sr system can be relatively easy reset by impact metamorphism and hence whole rock isochrons are often disturbed (see e.g., compilation by Borg et al., 2015). In addition to isochron dating the Rb-Sr systematics can also be used to date volatile depletion events in the context of dating early solar system events (Hans et al. 2013) because Rb is volatile ( $T_c = 800 \text{ K}$ ) and Sr is refractory ( $T_c = 1464 \text{ K}$ ). Regarding the lunar chronology the Rb-Sr systematics can be used to constrain an Rb-Sr model age for the time of Moon formation, because the giant impact was associated with strong Rb-Sr fractionation (Halliday, 2008; Mezger et al., 2021; Borg et al., 2022). However, prior studies yielded contrary results using this approach, because such model ages rely not only on precise Sr-isotopic compositions of lunar rocks, but also on assumptions about the parameters of the Moon-forming Impact. Chapter 4 tackles these issues with new Sr-isotopic measurements and new Rb-Sr model age calculations.

## 1.5. Objectives of the thesis

Strontium isotopes have great potential to address several key issues in cosmochemistry, such as the origin of nucleosynthetic isotope anomalies or the time of Moon formation. This thesis makes use of the different characteristics of Sr isotopes and the recent advantages in high-precision isotope measurement techniques to investigate both nucleosynthetic anomalies among meteorites and the timing of Moon formation. The thesis consists of three separate scientific manuscripts organized as three different chapters, which cover the following objectives:

- I) In **Chapter 2**, current state-of-the-art mass spectrometry for Sr isotopes is scrutinized to explore and circumvent analytically induced uncertainties. Chapter 2 explores and highlights the importance of Faraday cup degradation in TIMS instruments and emphasizes the need to carefully assess measurement techniques when investigating isotopic variations at the ppm level. An understanding of potential analytically induced errors and the setup of precise and stable measurement conditions is crucial to investigate  $^{84}\text{Sr}$  and  $^{87}\text{Sr}$  variations with high precision.
- II) The isotopic dichotomy is visible in many elements. The currently available data for  $\mu^{84}\text{Sr}$  however, is inconsistent and does not allow for discussion of the range and extent of nucleosynthetic Sr isotope anomalies in the context of the dichotomy. In **Chapter 3**, a dynamic measurement routine is used to obtain new high-precision  $\mu^{84}\text{Sr}$  isotopic data for a comprehensive set of NC and CC meteorites, as well as several samples from Earth, Mars, and the Moon. Thereby the extent of nucleosynthetic Sr variability will be clarified in a consistent dataset with unprecedented precision, and the new results can be utilized to explore the origin of nucleosynthetic variability in the disk and the origin of nucleosynthetic Sr isotope anomalies. Hence, the new data can potentially contribute to a better understanding of the origin of nucleosynthetic Sr isotope variability and the isotopic dichotomy, as this was not possible with previous datasets.

III) The age of the Moon is one of the major open questions in cosmochemistry. Furthermore, the chronology of lunar crust formation, which would provide tight constraints on the age of the Moon, is far from clear and explicitly lacks precisely dated anorthosite samples. Models predict timescales of 10-200 Ma for the lifetime of the LMO. However, reliable age data for FANs are limited to one sample only, which overlaps in age with KREEP- and Mg-Suite samples, suggesting a short LMO solidification timescale. In **Chapter 4**, new high-precision multi-dynamic measurements of  $^{87}\text{Sr}/^{86}\text{Sr}$  for lunar ferroan anorthosites are presented, which allow to determine relative timescales of FAN formation with a precision of  $\pm 14$  Ma. This way, the formation history of the Moon and the solidification timescale of the lunar magma ocean can be explored with a new approach of relative dating using the  $^{87}\text{Sr}/^{86}\text{Sr}_{\text{initial}}$  of FANs. Additionally, the newly obtained high-precision initial  $^{87}\text{Sr}/^{86}\text{Sr}$  of the Moon can be used to calculate an Rb-Sr model age of the Moon within the framework of more recent impact scenarios because the widely used canonical impact model cannot explain the striking similarity of the Earth and the Moon and hence the full range of possibilities and uncertainties should be considered.

The results are summarized, and an outlook for future research directions is provided in **Chapter 5** at the end of the thesis.



## 2. Effects of Faraday cup deterioration on Sr and Cr isotope analyses by thermal ionization mass spectrometry

### Abstract

By comparing data from an extensive set of Sr and Cr isotope measurements performed on two different thermal ionization mass spectrometers (TIMS), using three sets of Faraday cups with different usage histories, we assess the effects of Faraday cup deterioration on high-precision isotope measurements by TIMS. We find that dynamic  $^{84}\text{Sr}/^{86}\text{Sr}$  and  $^{87}\text{Sr}/^{86}\text{Sr}$  measurements provide stable and reproducible results over the entire 56 months of this study, regardless of which set of Faraday cups is used. By contrast, static  $^{84}\text{Sr}/^{86}\text{Sr}$  and  $^{87}\text{Sr}/^{86}\text{Sr}$  measurements lead to deviant results, drifts over time, and in general exhibit larger scatter. For the most part, these differences can be attributed to changing Faraday cup efficiencies. For the instruments of this study we find that the center cup is most affected, consistent with this cup often receiving the highest ion beam intensities during measurements conducted in our laboratory. For Cr isotopes, we find that the correlation between mass fractionation-corrected  $^{53}\text{Cr}/^{52}\text{Cr}$  and  $^{54}\text{Cr}/^{52}\text{Cr}$  ratios observed for static measurements in several prior studies also reflects different Faraday cup efficiencies. Again, the changing efficiency of predominantly the center cup can account for the observed drift and correlation in  $^{53}\text{Cr}/^{52}\text{Cr}$  and  $^{54}\text{Cr}/^{52}\text{Cr}$ . Multi-static Cr isotope measurements reduce this drift, but still result in a residual correlation between the two ratios, suggesting this correlation in part also reflects unaccounted mass fractionation effects.

---

This chapter is submitted to the *Journal of Atomic Analytical Spectroscopy* as Schneider, J.M. and Kleine, T. (2024) 'Effects of Faraday cup deterioration on Sr and Cr isotope analysis in thermal ionization mass spectrometry'.

## 2.1. Introduction

Thermal ionization mass spectrometry (TIMS) is often the choice for high-precision isotope ratio measurements in geochemistry and cosmochemistry. This stems from the fact that the stability of the TIMS source allows for long-duration isotope analyses with small measurement uncertainties on individual isotope ratios. However, this in turn makes TIMS measurements susceptible to drifts in measured values that may be related to changes in instrument parameters during the course of an individual study. One such change is the deterioration of Faraday cups through the deposition of analyte atoms during measurements conducted with high ion beam intensities (Di et al., 2021). Primarily due to different usage histories, the deterioration of individual cups likely varies over time, and so can result in a drift of measured isotope ratios on timescales of weeks to months, introducing systematic uncertainties in the final measured isotopic compositions of samples (Fukai et al., 2017; Qin et al., 2011).

Two elements that are frequently measured using TIMS are strontium (Sr) and chromium (Cr). Strontium has four stable isotopes, namely  $^{84}\text{Sr}$ ,  $^{86}\text{Sr}$ ,  $^{87}\text{Sr}$ , and  $^{88}\text{Sr}$  with natural abundances of 0.56%, 9.86%, 7.00%, and 82.58%, respectively. Of these,  $^{87}\text{Sr}$  is produced by radioactive decay of  $^{87}\text{Rb}$ , making the  $^{87}\text{Rb}$ - $^{87}\text{Sr}$  system useful for dating geological processes and as a geochemical tracer (Faure and Powell, 1972). In addition, the four Sr isotopes are produced by different stellar nucleosynthetic processes (Papanastassiou and Wasserburg, 1978), and so measurements of  $^{84}\text{Sr}/^{86}\text{Sr}$  are of interest to search for nucleosynthetic isotope anomalies in meteorites and meteorite components (Moynier et al., 2012; Hans et al., 2013; Charlier et al., 2021; Schneider et al., 2023). Like Sr, Cr also has four stable isotopes, namely  $^{50}\text{Cr}$ ,  $^{52}\text{Cr}$ ,  $^{53}\text{Cr}$ , and  $^{54}\text{Cr}$  with natural abundances of 4.35%, 83.79%, 9.50% and 2.36%. Of these,  $^{53}\text{Cr}$  is produced by the decay of the short-lived, now-extinct radionuclide  $^{53}\text{Mn}$  (half-life  $\sim 3.7$  Ma), making the  $^{53}\text{Mn}$ - $^{53}\text{Cr}$  system an important chronometer for processes occurring in the first  $\sim 20$  Ma of the solar system (Birck and Allegre, 1988; Trinquier et al., 2008; Qin and Wang, 2017; Anand et al., 2021). In addition, meteorites display widespread variations in  $^{54}\text{Cr}/^{52}\text{Cr}$ , which are interpreted to predominantly be nucleosynthetic in origin (Rotaru et al., 1992; Trinquier et al., 2007; Qin et

al., 2010). Together, this makes both Sr and Cr isotope measurements versatile tools to study a wide range of processes in geochemistry and cosmochemistry.

We routinely conduct Sr and Cr isotope measurements in our laboratory since 2018, using two different TIMS instruments and three sets of Faraday cups with different usage histories. Here we report an extensive set of Sr and Cr standard measurements acquired over this long period of time, including measurements with extensively used and new Faraday cups. By systematically investigating the effect of different cup settings using different sets of cups, this provides a unique opportunity to assess the significance and overall effect of cup deterioration on high-precision isotope measurements by TIMS.

## **2.2. Materials and Methods**

### **2.2.1 Materials and standards**

The standards used throughout this study are the certified National Institute of Standards and Technology (NIST) standard reference materials (SRM) 3112a for Cr and 987 for Sr. Both standards were prepared as  $\sim 500 \text{ ng } \mu\text{l}^{-1}$  solutions using 6 M HCl; these solutions were used for loading Sr and Cr onto the filaments. All measurements were performed using zone-refined Re filaments (99.999% Re, width 0.76 cm, purchased from H Cross Company, NJ 07074 USA), welded onto single filaments and cleaned by outgassing under vacuum ( $< 1 \times 10^{-5}$  mbar) at 4.5 A for 288 minutes using the ThermoScientific filament degassing device.

### **2.2.2 Instrumental setup and measurement series**

The isotope measurements of this study were conducted on two different instruments and using three sets of Faraday cups having different lifetimes. The first instrument is the ThermoScientific Triton *Plus* at the University of Münster, for which two different sets of Faraday cups were used. The first set was used for  $\sim 6$  years for a variety of isotope measurements since installation of the instrument in 08/2015, including measurements of Ba, Nd, Sm, Cr, Sr, Dy, Er (Schneider et al., 2023; Hellmann et al., 2023; Schneider et al., 2020; Shollenberger et al., 2018; Shollenberger et al., 2021; Archer et al., 2019; Render and Brennecka, 2021; Brennecka and Kleine, 2017). As such, the

measurements conducted with this instrument setup (hereafter ‘setup #1’) provide a good example of measurements utilizing cups with an intensive pre-history. In 12/2019, a new set of Faraday cups was installed on the Triton Plus in Münster (corresponding to ‘setup #2’), and new Sr and Cr isotope measurements were conducted starting immediately after the cup installation. The second instrument used in this study is a ThermoScientific Triton XT installed at the Max Planck Institute for Solar System Research (MPS) in 09/2022. This instrument has been used for some additional  $^{87}\text{Sr}/^{86}\text{Sr}$  measurements, which were performed immediately after installation of the instrument (‘setup #3’). Thus, comparing measurements using setup #1 with those using setups #2 and #3 allows for the direct assessment of potential effects of using Faraday cups of different ages and usage history on high-precision isotope measurements.

We report data from three measurement campaigns, which used the three setups described above. To this end, long-term  $^{87}\text{Sr}/^{86}\text{Sr}$  measurements of SRM 987 are reported for all three setups, while  $^{84}\text{Sr}/^{86}\text{Sr}$  as well as  $^{53}\text{Cr}/^{52}\text{Cr}$  and  $^{54}\text{Cr}/^{52}\text{Cr}$  measurements are reported for setups #1 and #2. In addition to these long-term measurements, we also performed two single sets of experiments where the  $^{84}\text{Sr}/^{86}\text{Sr}$  and  $^{87}\text{Sr}/^{86}\text{Sr}$  ratios were measured consecutively in static mode using five different magnetic settings with masses 84 through 88 collected in the center cup (see Table 1). For each magnet setting, 4–5 static measurements were conducted. The purpose of this experiment is to systematically assess how the use of specific Faraday cups affects the final measured isotope ratios and thereby test as to whether differences in deterioration among different Faraday cups can be identified. This experiment was performed using setups #1 and #2.

### 2.2.3 Strontium isotope measurements

The measurements of  $^{84}\text{Sr}/^{86}\text{Sr}$  and  $^{87}\text{Sr}/^{86}\text{Sr}$  ratios were performed independently of each other and using different cup configurations (see Table 1). A gain calibration was performed before each individual measurement session (corresponding to samples loaded onto a single sample wheel). For both measurements, 1  $\mu\text{l}$  of the NIST SRM 987 solution containing  $\sim 500$  ng Sr was loaded onto each filament. The sample was dried at 1 A and topped with 1  $\mu\text{l}$  of  $\text{Ta}_2\text{O}_5$  activator solution consisting of 50 mg of 99.999% pure  $\text{Ta}_2\text{O}_5$  powder suspended in 3 ml 0.5 M  $\text{H}_3\text{PO}_4$ . After the mixture dried, the filament was heated to

glow for  $\sim 1$  s and is ready for measurement. For the  $^{87}\text{Sr}/^{86}\text{Sr}$  measurements, the filaments were stepwise heated at 370 mA/min using the automatic heat function of the Triton *Plus* until a signal of 0.2 V is reached on  $^{88}\text{Sr}$ . At this point the heating rate is reduced to 250 mA/min until a signal of 10 V on  $^{88}\text{Sr}$  is reached, and the measurement is started with a signal of 10.5 V of  $^{88}\text{Sr}$ . During the heating process, the lenses were focused and a peak center was performed at signals of 0.2 V and 10 V. For the measurement of  $^{84}\text{Sr}/^{86}\text{Sr}$ , this procedure remained the same, but the final signal was increased to 25–30 V on  $^{88}\text{Sr}$  and an additional lens focus was performed at a signal of 15 V. For both the  $^{84}\text{Sr}/^{86}\text{Sr}$  and  $^{87}\text{Sr}/^{86}\text{Sr}$  measurements, only Faraday cups connected to feedback resistors with  $10^{11} \Omega$  amplifiers were used, and no amplifier rotation was employed. Mass fractionation was corrected using the exponential law and  $^{86}\text{Sr}/^{88}\text{Sr} = 0.1194$  (Meija et al., 2016; Russell et al., 1978).

The  $^{84}\text{Sr}/^{86}\text{Sr}$  measurements consisted of two lines of data acquisition, which provide two separate static  $^{84}\text{Sr}/^{86}\text{Sr}$  ratios for each line and a dynamic  $^{84}\text{Sr}/^{86}\text{Sr}$  ratio (Table 1). The latter is obtained by correcting the  $^{84}\text{Sr}/^{86}\text{Sr}$  measured in the first line for instrumental mass fractionation using  $^{86}\text{Sr}/^{88}\text{Sr}$  measured in the second line as follows (Hans et al., 2013; Yobregat et al., 2017):

*Equation 5*

$$\left(\frac{^{84}\text{Sr}}{^{86}\text{Sr}}\right)_{dyn.} = \left(\frac{^{84}\text{Sr}}{^{86}\text{Sr}}\right)_{line\ 1} \times \left(\frac{\left(\frac{^{86}\text{Sr}}{^{88}\text{Sr}}\right)_{true}}{\left(\frac{^{86}\text{Sr}}{^{88}\text{Sr}}\right)_{line\ 2}}\right)^{\left(\frac{\ln\left(\frac{M(^{84}\text{Sr})}{M(^{86}\text{Sr})}\right)}{\ln\left(\frac{M(^{86}\text{Sr})}{M(^{88}\text{Sr})}\right)}\right)}.$$

The  $^{84}\text{Sr}/^{86}\text{Sr}$  and  $^{86}\text{Sr}/^{88}\text{Sr}$  ratios measured in this manner use the same Faraday cups, and so any bias induced by different cup efficiencies cancel out (Hans et al., 2013; Yobregat et al., 2017). The  $^{84}\text{Sr}/^{86}\text{Sr}$  measurements were performed using 4 s idle time on line 1 and 10 s idle time on line 2, which ensures complete decay of the high  $^{88}\text{Sr}$  beam measured in the H2 cup, which in line 2 is used to measure the ion beam on the much lower abundance isotope  $^{86}\text{Sr}$ . Both lines used 4 s integration time and a peak center and lens focus was performed every five blocks. One measurement consists of 25 blocks of 20 cycles each.

The  $^{87}\text{Sr}/^{86}\text{Sr}$  measurements used a three-line data acquisition theme following the method described in Hans et al. (2013). In this procedure,  $^{86}\text{Sr}$  is collected in cups H1, C, and L1, respectively, with all other Sr isotopes collected accordingly in each line (Table 1). This procedure allows determining three static  $^{87}\text{Sr}/^{86}\text{Sr}$  ratios for each line, as well as a multi-dynamic  $^{87}\text{Sr}/^{86}\text{Sr}$  calculated as follows:

Equation 6

$$\left(\frac{^{87}\text{Sr}}{^{86}\text{Sr}}\right)_{dyn.} = \frac{1}{2} \times \left( \sqrt{\left(\frac{^{87}\text{Sr}}{^{86}\text{Sr}}\right)_{line\ 1} \times \left(\frac{^{87}\text{Sr}}{^{88}\text{Sr}}\right)_{line\ 2} \times \left(\frac{^{88}\text{Sr}}{^{86}\text{Sr}}\right)_{true}} + \sqrt{\left(\frac{^{87}\text{Sr}}{^{86}\text{Sr}}\right)_{line\ 2} \times \left(\frac{^{87}\text{Sr}}{^{88}\text{Sr}}\right)_{line\ 3} \times \left(\frac{^{88}\text{Sr}}{^{86}\text{Sr}}\right)_{true}} \right) \times \sqrt{1 - \frac{\ln\left(\left(\frac{^{87}\text{Sr}}{^{88}\text{Sr}}\right)_{line\ 2} \times \left(\frac{^{88}\text{Sr}}{^{86}\text{Sr}}\right)_{true} / \left(\frac{^{87}\text{Sr}}{^{88}\text{Sr}}\right)_{line\ 2}\right)}{\ln\left(\frac{M(^{86}\text{Sr})}{M(^{88}\text{Sr})}\right)}}{M(^{86}\text{Sr})^2}},$$

where the subscript refers to magnet settings of lines 1, 2 or 3, respectively (Table 1).

**Table 1:** Cup settings for Sr-isotopic measurements.

Line	L4	L3	L2	L1	Center	H1	H2	H3	H4
<i><math>^{87}\text{Sr}/^{86}\text{Sr}</math> measurements</i>									
1				$^{84}\text{Sr}$	$^{85}\text{Rb}$	$^{86}\text{Sr}$	$^{87}\text{Sr}$	$^{88}\text{Sr}$	
2			$^{84}\text{Sr}$	$^{85}\text{Rb}$	$^{86}\text{Sr}$	$^{87}\text{Sr}$	$^{88}\text{Sr}$		
3		$^{84}\text{Sr}$	$^{85}\text{Rb}$	$^{86}\text{Sr}$	$^{87}\text{Sr}$	$^{88}\text{Sr}$			
<i><math>^{84}\text{Sr}/^{86}\text{Sr}</math> measurements</i>									
1					$^{84}\text{Sr}$	$^{85}\text{Rb}$	$^{86}\text{Sr}$	$^{87}\text{Sr}$	$^{88}\text{Sr}$
2			$^{84}\text{Sr}$	$^{85}\text{Rb}$	$^{86}\text{Sr}$	$^{87}\text{Sr}$	$^{88}\text{Sr}$		
<i>Cup-efficiency experiment</i>									
84-Center					$^{84}\text{Sr}$	$^{85}\text{Rb}$	$^{86}\text{Sr}$	$^{87}\text{Sr}$	$^{88}\text{Sr}$
85-Center				$^{84}\text{Sr}$	$^{85}\text{Rb}$	$^{86}\text{Sr}$	$^{87}\text{Sr}$	$^{88}\text{Sr}$	
86-Center			$^{84}\text{Sr}$	$^{85}\text{Rb}$	$^{86}\text{Sr}$	$^{87}\text{Sr}$	$^{88}\text{Sr}$		
87-Center		$^{84}\text{Sr}$	$^{85}\text{Rb}$	$^{86}\text{Sr}$	$^{87}\text{Sr}$	$^{88}\text{Sr}$			
88-Center	$^{84}\text{Sr}$	$^{85}\text{Rb}$	$^{86}\text{Sr}$	$^{87}\text{Sr}$	$^{88}\text{Sr}$				

One measurement consists of 25 blocks of 20 cycles with 8 s integration time and 4 s idle time each. Baseline (30 s) measurement, peak center, and lens focus was done every five blocks. For all Sr isotope measurements, possible isobaric interferences from  $^{87}\text{Rb}$  on  $^{87}\text{Sr}$  were monitored using the ion beam intensity on interference-free  $^{85}\text{Rb}$ . Natural samples might require an Rb-interference correction, however, no  $^{85}\text{Rb}$  signal was observed in any of the Sr isotope measurements of this study, reflecting the lower ionization potential of Rb, the high purity of the SRM 987 Sr standard and the low Rb blank of our procedure.

#### 2.2.4 Chromium isotope measurements

The Cr isotope measurements were made in static mode following the method described in Schneider et al. (2020). Approximately 1  $\mu\text{g}$  Cr of NIST SRM3112a was loaded onto outgassed Re filaments and dried at 0.7 A. The sample was covered with about 3  $\mu\text{l}$  of an Al-Si-gel emitter and dried at 1.2 A for 30 s. Finally, the filament was heated to 2 A for  $\sim 5$  s, while preventing the filament from glowing to ensure complete homogenization of sample and emitter, maintaining stickiness of this mixture on the filament (Schneider et al., 2020). For the measurements, filaments were stepwise heated until reaching a signal of 10 V on  $^{52}\text{Cr}$  using the automatic heat function of the Triton *Plus* using a slow heating procedure ( $\sim 30$  min). Ion beams on  $^{50}\text{Cr}$ ,  $^{52}\text{Cr}$ ,  $^{53}\text{Cr}$ , and  $^{54}\text{Cr}$  were collected in the L3, C, H1, and H2 cups, respectively, and all cups are connected to  $10^{11}$   $\Omega$  feedback resistors. Measurement were typically conducted with  $\sim 10$  V on  $^{52}\text{Cr}$  and correspond signal of 200–250 mV on  $^{54}\text{Cr}$ . Isobaric interferences from  $^{50}\text{Ti}$ ,  $^{50}\text{V}$ , and  $^{54}\text{Fe}$  were monitored using  $^{49}\text{Ti}$ ,  $^{51}\text{V}$ , and  $^{56}\text{Fe}$  in cups L4, L1, and H4, respectively. Each measurement consisted of 50 blocks of 30 cycles each with 4 s integration time per cycle for setup #1 and was later reduced to 25 blocks of 30 cycles for setup #2. Baseline measurements (30 s) and a lens focus were performed every three blocks.

For multi-static Cr isotope measurements, we used a 4-line routine outlined in Table 2 (Trinquier et al., 2008), where peak shapes and alignments were adjusted using the focus and dispersion lens system of the Triton *Plus* before each measurement session (i.e., one sample wheel), similar to multi-dynamic Sr isotope measurements. Each line is measured using 8 s of integration time and separated by 4 s of idle time. One measurement consists of 10 blocks with 20 cycles/block and a peak-center and baseline (30 s) measurement every

two blocks and a filament and lens focus after five blocks. The final  $^{53}\text{Cr}/^{52}\text{Cr}$  and  $^{54}\text{Cr}/^{52}\text{Cr}$  ratios are calculated as averages of lines 1–4 for  $^{53}\text{Cr}/^{52}\text{Cr}$  and lines 1–3 for  $^{54}\text{Cr}/^{52}\text{Cr}$  (Table 2). This difference reflects that measurement of  $^{54}\text{Cr}$  in a fourth line was not possible due to the instrument's cup setup.

Final mass fractionation-corrected ratios of  $^{53}\text{Cr}/^{52}\text{Cr}$  and  $^{54}\text{Cr}/^{52}\text{Cr}$  for all Cr measurements were obtained by internally normalizing to a fixed  $^{50}\text{Cr}/^{52}\text{Cr}$  ratio of 0.051859 using the exponential law (Russell et al., 1978; Shields et al., 1966). During measurements using setup #1, a total of 108 standard measurements were made over a period of 12 months, while with setup #2 65 standard measurements were made during the first three months after installation of the new Faraday cups.

**Table 2:** Cup settings for Cr-isotopic measurements.

Line	L3	L2	L1	Center	H1	H2	H3	H4
<i>Static Cr measurements</i>								
	$^{49}\text{Ti}$	$^{50}\text{Cr}$	$^{51}\text{V}$	$^{52}\text{Cr}$	$^{53}\text{Cr}$	$^{54}\text{Cr}$		$^{56}\text{Fe}$
<i>Multi-static Cr measurements</i>								
1	$^{50}\text{Cr}$	$^{51}\text{V}$	$^{52}\text{Cr}$	$^{53}\text{Cr}$	$^{54}\text{Cr}$		$^{56}\text{Fe}$	
2		$^{50}\text{Cr}$	$^{51}\text{V}$	$^{52}\text{Cr}$	$^{53}\text{Cr}$	$^{54}\text{Cr}$		
3			$^{50}\text{Cr}$	$^{51}\text{V}$	$^{52}\text{Cr}$	$^{53}\text{Cr}$	$^{54}\text{Cr}$	
4				$^{50}\text{Cr}$	$^{51}\text{V}$	$^{52}\text{Cr}$	$^{53}\text{Cr}$	

## 2.3. Results and Discussion

### 2.3.1 Effects of cup deterioration on Sr isotope measurements

The results of static and dynamic  $^{84}\text{Sr}/^{86}\text{Sr}$  and  $^{87}\text{Sr}/^{86}\text{Sr}$  measurements using two or three instrument setups, respectively, are shown in Figure 7. While there is significant scatter for the static  $^{84}\text{Sr}/^{86}\text{Sr}$  and  $^{87}\text{Sr}/^{86}\text{Sr}$  measurements for each setup, the dynamic  $^{84}\text{Sr}/^{86}\text{Sr}$  and  $^{87}\text{Sr}/^{86}\text{Sr}$  measurements show excellent long-term reproducibility during the 56 months course of this study (for Sr measurements) with mean values of  $^{84}\text{Sr}/^{86}\text{Sr} = 0.056491 \pm 0.000002$  (2 s.d.;  $n = 203$ ) and  $^{87}\text{Sr}/^{86}\text{Sr} = 0.710245 \pm 0.000004$  (2 s.d.;  $n = 50$ ). By contrast, static measurements for one particular cup configuration deviate from the dynamic  $^{84}\text{Sr}/^{86}\text{Sr}$  and  $^{87}\text{Sr}/^{86}\text{Sr}$  ratios by  $\sim 150$  and  $\sim 100$  ppm, respectively, and also show more scatter, which is predominantly caused by drift of the measured isotope ratios with time. This is particularly evident for the static  $^{87}\text{Sr}/^{86}\text{Sr}$  measurements using setups #2

and #3 (Fig. 7). Notably, comparison of the static  $^{84}\text{Sr}/^{86}\text{Sr}$  and  $^{87}\text{Sr}/^{86}\text{Sr}$  measurements using the three different setups show no obvious difference, i.e., using new Faraday cups in setups #2 and #3 do not appear to have resulted in significant improvement over the measurements performed using setup #1, which used aged Faraday cups. Thus, it is clear that dynamic  $^{84}\text{Sr}/^{86}\text{Sr}$  and  $^{87}\text{Sr}/^{86}\text{Sr}$  measurements provide much more reproducible and long-term stable results than static measurements (e.g., Wang et al., 2016). However, from these measurements alone it remains unclear to what extent the offset and poorer reproducibility of the static measurements is related to deterioration of the Faraday cups. To assess this effect more rigorously, we performed static  $^{84}\text{Sr}/^{86}\text{Sr}$  and  $^{87}\text{Sr}/^{86}\text{Sr}$  measurements using setups #1 and #2, and using five different magnetic settings with masses 84 through 88 collected in the center cup (see Table 1).

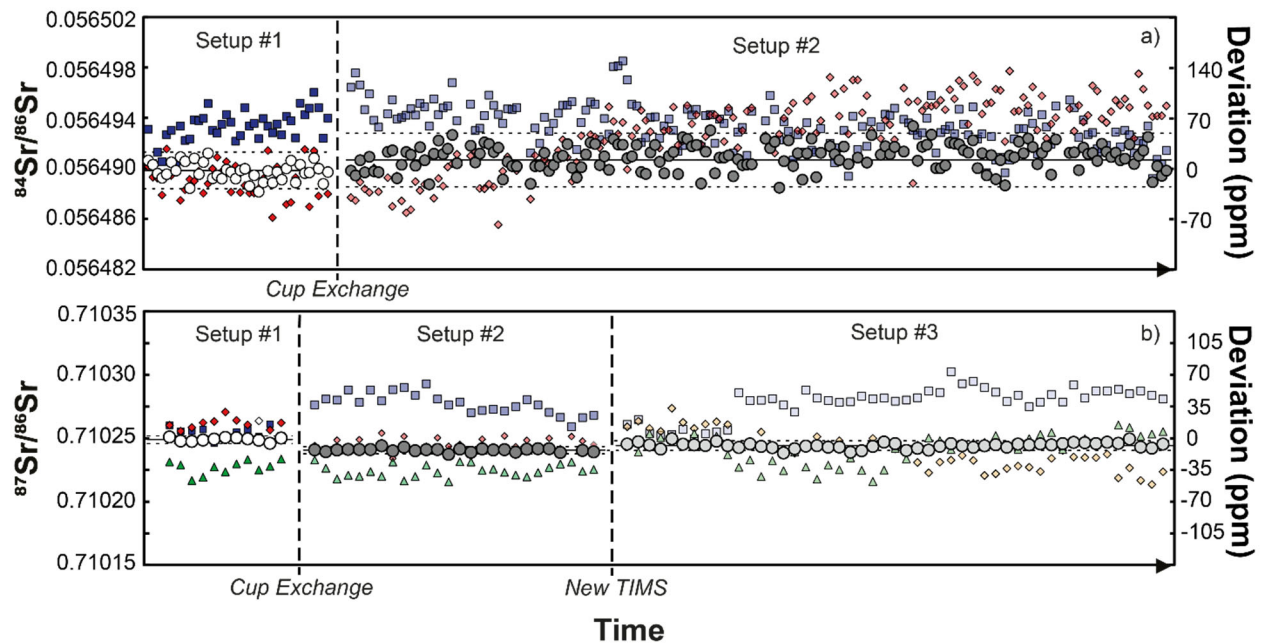


**Figure 7:** Mass fractionation-corrected  $^{84}\text{Sr}/^{86}\text{Sr}$  (a) and  $^{87}\text{Sr}/^{86}\text{Sr}$  ratios (b) for the SRM 897 Sr standard for setups #1, #2, and #3. For each setup, results for static measurements from individual lines and the results of the corresponding dynamic measurements are shown. Squares denote static results for line 1, diamonds for line 2, and triangles for line 3. Dashed lines show the external reproducibility ( $\pm 2$  s.d.) of the dynamic measurements. Right vertical axes provide parts-per-million deviations of measured isotope ratios from the mean of the dynamic results.

As shown in Figure 8, for both  $^{84}\text{Sr}/^{86}\text{Sr}$  and  $^{87}\text{Sr}/^{86}\text{Sr}$  the deviations from the dynamic values are smaller using setup #2 (new cups) compared to setup #1 (old cups), although some deviations remain. To assess whether these deviations can be linked to a specific Faraday cup, we modeled the effect of different Faraday cup efficiency factors on the measured isotope ratios. The cup efficiency can be understood as the ratio of the ion current in the high-ohmage feedback resistor connected to each cup to the ion current that is injected into the cup (Di et al., 2021). The cup efficiency is not to be confused with the amplifier gain factor, which is a conversion factor between the true input voltage from the cup to the output voltage and is determined before each analytical session (see above). Our calculations show that the different  $^{84}\text{Sr}/^{86}\text{Sr}$  and  $^{87}\text{Sr}/^{86}\text{Sr}$  ratios measured for the different magnetic settings using setup #1 are well reproduced by modifying the efficiency factor of only the central Faraday cup (Fig. 8).

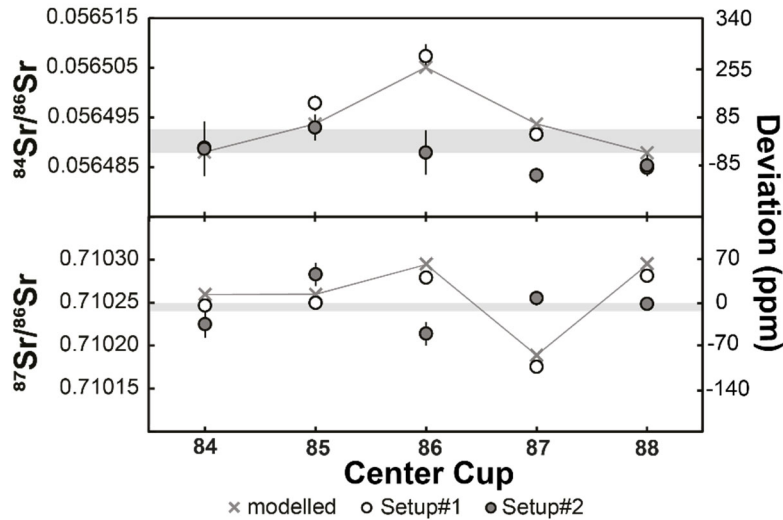


**Figure 8:** Mass fractionation-corrected  $^{84}\text{Sr}/^{86}\text{Sr}$  and  $^{87}\text{Sr}/^{86}\text{Sr}$  ratios for NIST SRM 987 measured with different magnet settings (Table 1) and using Faraday cups with extensive pre-usage (setup #1) and new cups (setup #2). Also shown are expected variations if the cup efficiency factor of the center cup is set to 0.9999, while the factor for all other cups is 1. These expected variations are in good agreement with the measured isotope ratios using setup #1. Horizontal grey bands show dynamic results for  $^{84}\text{Sr}/^{86}\text{Sr}$  and  $^{87}\text{Sr}/^{86}\text{Sr}$  with their respective external reproducibility ( $\pm 2\text{s.d.}$ ).

This is consistent with results of a prior study (Wang et al., 2016) and the observation that for measurements with either  $^{84}\text{Sr}$  or  $^{85}\text{Rb}$  collected in the center cup, the variations among the static and dynamic  $^{87}\text{Sr}/^{86}\text{Sr}$  measurements are the smallest (Fig. 8). This is because for these magnetic settings, the center cup is not used for either  $^{86}\text{Sr}$ ,  $^{87}\text{Sr}$ , or  $^{88}\text{Sr}$ , which are the three isotopes used for the calculation of mass-fractionation-corrected  $^{87}\text{Sr}/^{86}\text{Sr}$  ratios. In detail, the variable  $^{84}\text{Sr}/^{86}\text{Sr}$  and  $^{87}\text{Sr}/^{86}\text{Sr}$  ratios measured using the different magnetic settings are reproduced by arbitrarily setting the cup efficiency of the center cup to 0.9999, while keeping the cup efficiencies of all other cups at 1. This does not mean that *only* the center cup is deteriorated, but it shows this cup appears to be affected the most in this specific case. As discussed by Di et al. (2021), the main cause of changes in cup efficiency is the number of ions already collected in a specific cup. This is consistent with the quite extensive usage history of about six years for this set of Faraday cups and with the fact that for most measurements conducted on this instrument, the center cup usually received the highest ion beams. For instance, the instrument has been used for extensive static Cr isotope measurements (see section 2.3.2), where the most abundant isotope  $^{52}\text{Cr}$  is collected in the center cup.

We conducted the same measurements with setup #2, i.e., using a new set of Faraday cups. The absolute  $^{84}\text{Sr}/^{86}\text{Sr}$  and  $^{87}\text{Sr}/^{86}\text{Sr}$  ratios measured deviate from those obtained using setup #1, but as noted above, also deviate from the dynamic results obtained using both setups. However, the deviations observed for setup #2 cannot be attributed to the relative difference in the efficiency of an individual cup. This is not surprising because, given that a new set of Faraday cups has been used, there is no single cup that should be systematically different from all other cups. As such, the differences among the static  $^{84}\text{Sr}/^{86}\text{Sr}$  and  $^{87}\text{Sr}/^{86}\text{Sr}$  ratios measured for different magnetic settings, and the deviations of these values from the dynamic measurements, most likely reflect small inherent variations in Faraday cup efficiencies related to differences in material and surface properties among the individual cups.

Figure 9 compares the  $^{84}\text{Sr}/^{86}\text{Sr}$  ratios with different magnet settings of this study to available data from previous studies. Two observations stand out. First, the variable  $^{84}\text{Sr}/^{86}\text{Sr}$  ratios reported in prior studies show a similar pattern as our results for different

magnetic settings, where the largest offsets are observed when  $^{86}\text{Sr}$  is measured in the center cup. Of note, when  $^{85}\text{Rb}$  or  $^{87}\text{Sr}$  are collected in the center cup, the offsets are much smaller, most likely because the center cup is not used for measurement of  $^{84}\text{Sr}$ ,  $^{86}\text{Sr}$ , or  $^{88}\text{Sr}$ , i.e., the three isotopes used for calculation of mass-fractionated  $^{84}\text{Sr}/^{86}\text{Sr}$  ratios. Thus, systematic differences for different magnet settings and larger cup deterioration for the center cup are not a feature specific to a single TIMS instrument, but also appear to be present for other TIMS instruments. Second, the dynamic  $^{84}\text{Sr}/^{86}\text{Sr}$  measurements of all studies are in very good agreement, suggesting that differences in reported  $^{84}\text{Sr}/^{86}\text{Sr}$  ratios predominantly are due to unaccounted variations in Faraday cup efficiencies.

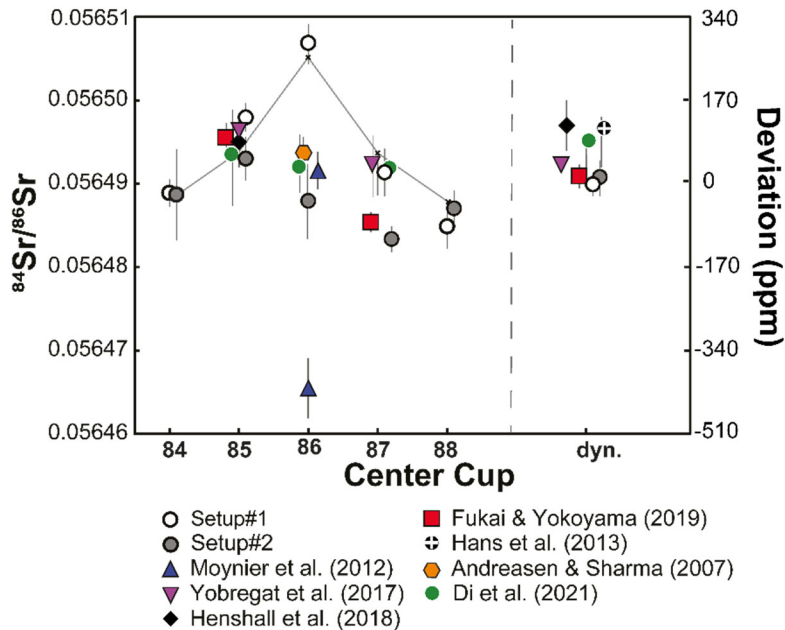


**Figure 9:** Comparison of  $^{84}\text{Sr}/^{86}\text{Sr}$  ratios for NIST SRM987 measured in this and in prior studies. Note the good agreement of the results except if  $^{86}\text{Sr}$  is collected in the center cup. Small crosses and bold line denote the modelled results from Figure 8. For details see text.

### 2.3.2 Effects of cup deterioration on Cr isotope measurements

During the course of the Sr isotope measurements described above, the TIMS instrument in Münster (setups #1 and #2) was also extensively used for Cr isotope measurements. Given the evidence for deterioration of the central cup based on the

Sr isotope measurements, the question arises how this deterioration affected the Cr isotope measurements.

As shown in Figure 10, both the  $^{53}\text{Cr}/^{52}\text{Cr}$  and  $^{54}\text{Cr}/^{52}\text{Cr}$  measured for the SRM 3112a standard using setup #1 drift over time to higher values, resulting in a strong positive correlation between these two ratios (Fig. 10, Fig. 11a). This correlation has also been observed in several prior studies (Qin et al., 2010; Trinquier et al., 2008; Lugmair and Shukolyukov, 1998). Immediately after the cup exchange (setup #2), the measured  $^{53}\text{Cr}/^{52}\text{Cr}$  and  $^{54}\text{Cr}/^{52}\text{Cr}$  ratios drop substantially by  $\sim 90$  ppm and  $\sim 130$  ppm, respectively, to values that are even lower than the value at the beginning of the measurement series using setup #1. However, even for setup #2 a slight drift in measured  $^{54}\text{Cr}/^{52}\text{Cr}$  ratios can be observed, and after about 8 months of use, a weak correlation between the measured  $^{53}\text{Cr}/^{52}\text{Cr}$  and  $^{54}\text{Cr}/^{52}\text{Cr}$  ratios emerges again (Fig. 11 a–c). As shown in Figure 10 and 11, this drift and the resulting correlation is a temporal effect, as later measurements systematically yielded higher  $^{53}\text{Cr}/^{52}\text{Cr}$  and  $^{54}\text{Cr}/^{52}\text{Cr}$  ratios compared to the earlier measurements.

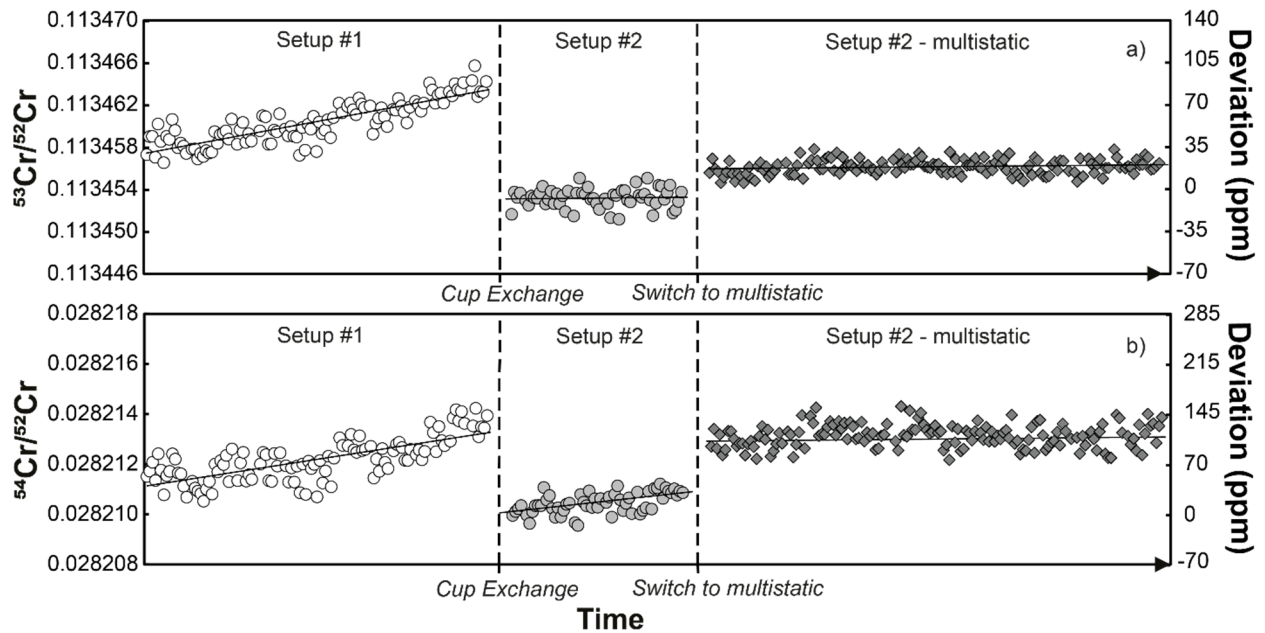


**Figure 10:** Mass fractionation-corrected  $^{53}\text{Cr}/^{52}\text{Cr}$  (a) and  $^{54}\text{Cr}/^{52}\text{Cr}$  ratios (b) for the SRM 3112a Cr standard for static measurements using setup #1 and setup #2, and multi-static measurements using setup #3. Right vertical axes provide parts-per-million deviations of measured isotope ratios from the start of measurements using setup #2.

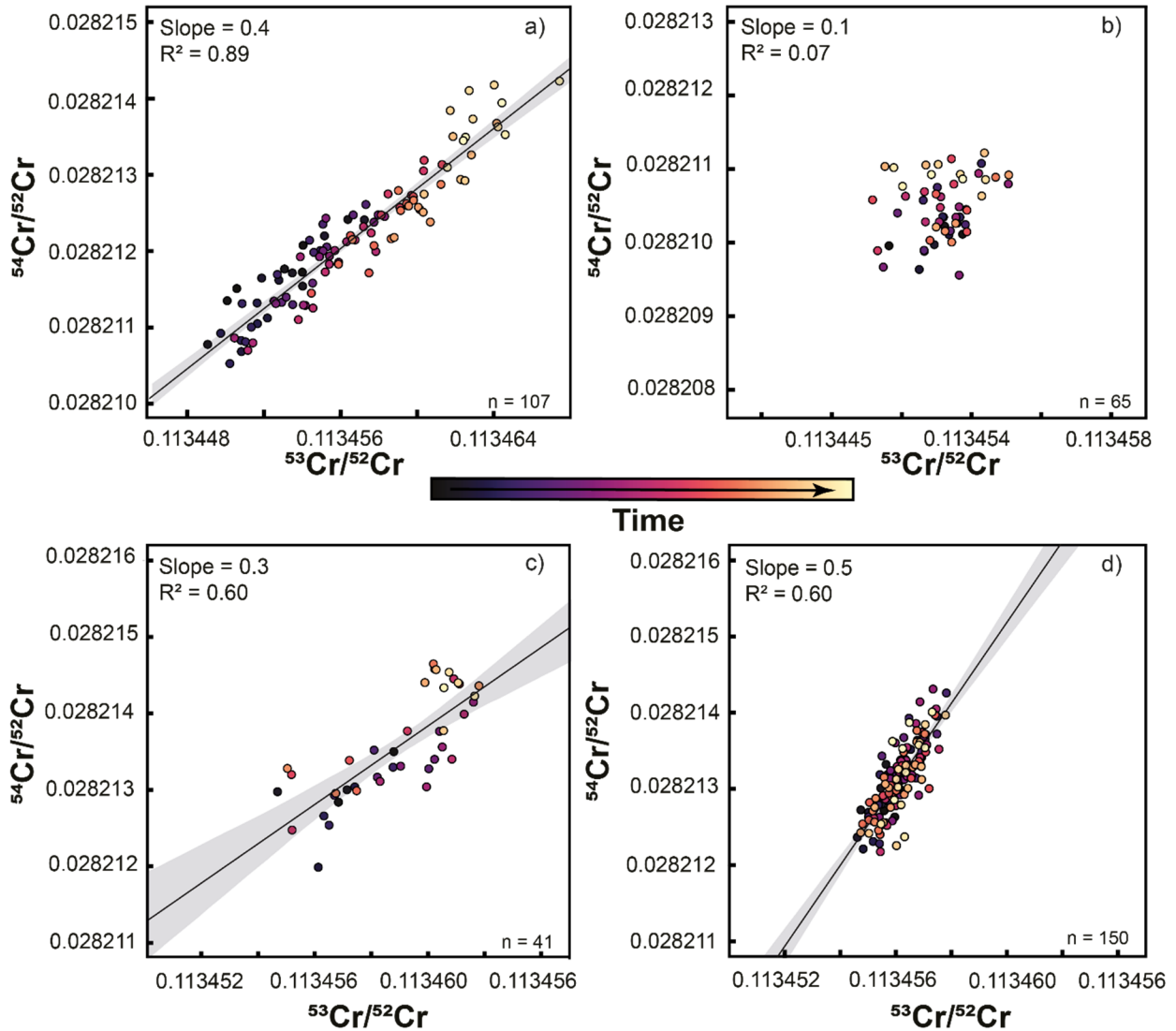


**Figure 11:** Mass fractionation-corrected  $^{53}\text{Cr}/^{52}\text{Cr}$  and  $^{54}\text{Cr}/^{52}\text{Cr}$  ratios of NIST SRM 3112a from static measurements using setup #1 (a) and setup #2 (b, c). Note the strong correlation of  $^{53}\text{Cr}/^{52}\text{Cr}$  and  $^{54}\text{Cr}/^{52}\text{Cr}$  obtained using setup #1 (a), which disappears entirely for the initial measurements using setup #2 (2 months) (b), but reappears relatively quickly after (8 months) (c). (d) Multi-static mass fractionation-corrected  $^{53}\text{Cr}/^{52}\text{Cr}$  and  $^{54}\text{Cr}/^{52}\text{Cr}$  ratios for NIST SRM3112a measured using setup #2. As for the static measurements, there is residual correlation between  $^{53}\text{Cr}/^{52}\text{Cr}$  and  $^{54}\text{Cr}/^{52}\text{Cr}$ , but this correlation is of smaller magnitude and does not reflect a temporal change in the measured ratios. As such, this correlation is probably due to residual mass fractionation effects. The color-coding of the data points indicates the time of individual measurements for each setup, demonstrating that the correlation of  $^{53}\text{Cr}/^{52}\text{Cr}$  and  $^{54}\text{Cr}/^{52}\text{Cr}$  ratios reflects a temporal drift of both ratios to higher values over time. The axis lengths were adjusted to display equal ranges.

To assess whether the correlation of  $^{53}\text{Cr}/^{52}\text{Cr}$  versus  $^{54}\text{Cr}/^{52}\text{Cr}$  ratios is due to Faraday cup deterioration, we calculated the change of both ratios resulting from a different cup efficiency of the central cup. As shown above, for the Sr isotope measurements using setup #1 we found that a cup efficiency of 0.9999 for the center cup, and 1 for all other cups, can account for the observed variations in measured  $^{84}\text{Sr}/^{86}\text{Sr}$  and  $^{87}\text{Sr}/^{86}\text{Sr}$  ratios. We find that these cup efficiencies result in higher measured  $^{53}\text{Cr}/^{52}\text{Cr}$  and  $^{54}\text{Cr}/^{52}\text{Cr}$  ratios compared to the ratios obtained with an efficiency of 1 for all Faraday cups, and a positive correlation between the two ratios with a slope that is in good agreement to the slopes observed for measurements with setup #1 and the later measurements with setup #2 (Fig. 12). Thus, as for Sr isotopes, the observed offsets in measured Cr isotope ratios can be attributed to Faraday cup deterioration of mainly the center cup.

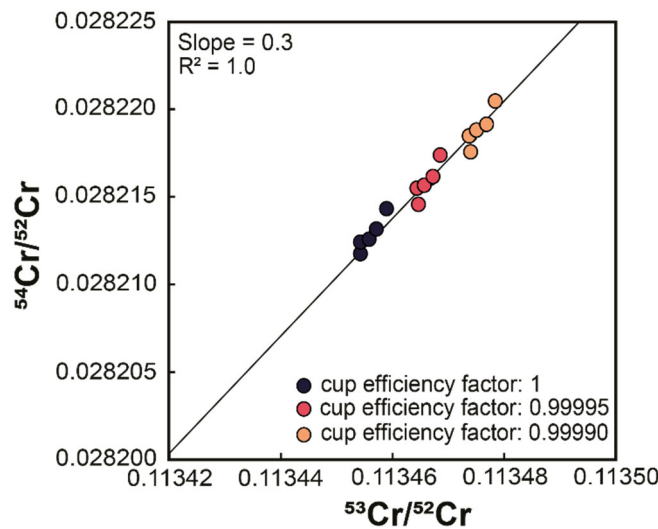


**Figure 12:** Effect of changing Faraday cup efficiency on mass fractionation-corrected  $^{53}\text{Cr}/^{52}\text{Cr}$  and  $^{54}\text{Cr}/^{52}\text{Cr}$  ratios. Calculations assume that the cup efficiency of only the center cup changes and show that a factor of 0.9999, and 0.99995 instead of 1 results in a positive correlation between  $^{53}\text{Cr}/^{52}\text{Cr}$  and  $^{54}\text{Cr}/^{52}\text{Cr}$  ratios similar to the correlation observed.

The correlation of  $^{53}\text{Cr}/^{52}\text{Cr}$  and  $^{54}\text{Cr}/^{52}\text{Cr}$  ratios has most commonly been attributed to residual mass fractionation that has not been accounted for by the correction for instrumental mass fractionation (Qin et al., 2010; Trinquier et al., 2008; Lugmair and Shukolyukov, 1998). However, our results show that at least for static measurements this correlation more likely results from changes in the Faraday cup efficiency of especially the

center cup, which is used to collect the ion beam of the most abundant Cr isotope,  $^{52}\text{Cr}$ , and is, as such, most susceptible to cup deterioration.

To overcome these problems inherent to static Cr isotope measurements, several studies used a multi-static setup, where Cr isotopes are measured in four or five different lines (Trinquier et al., 2008; Cornet et al., 2022). The same amount of sample (1  $\mu\text{g}$ ) was loaded onto one filament for multi-static measurements as for single static measurements, but the measurement time is four times as long as one static measurement. The idea of this approach is that the effects of different cup efficiencies should average out, as through the multi-line data acquisition all Cr isotopes are on average measured using the same set of Faraday cups. To assess if this is the case, we performed multi-static Cr isotope measurements using setup #2, which were all conducted after the static measurements conducted with this setup. We find that over a period of 9 months, both the  $^{53}\text{Cr}/^{52}\text{Cr}$  and  $^{54}\text{Cr}/^{52}\text{Cr}$  ratios no longer exhibit drift, thus allowing precise measurements of both ratios. However, when the multi-static  $^{53}\text{Cr}/^{52}\text{Cr}$  and  $^{54}\text{Cr}/^{52}\text{Cr}$  ratios are plotted against each other, a correlation with a similar slope as before is still apparent (Fig. 11d). A similar observation has been made by (Trinquier et al., 2008), using a similar setup as in this study. Importantly though, unlike for the static measurements, for the multi-static measurements the  $^{53}\text{Cr}/^{52}\text{Cr}$  and  $^{54}\text{Cr}/^{52}\text{Cr}$  ratios do not evolve over time and, as such, are unlikely to be related to the increasing aging of the Faraday cups. This is consistent with the idea that the effects of Faraday cup efficiencies should nearly cancel out in a multi-static measurement setup and suggests that the observed residual  $^{53}\text{Cr}/^{52}\text{Cr}$  versus  $^{54}\text{Cr}/^{52}\text{Cr}$  correlation in part reflects unaccounted mass fractionation effects (Trinquier et al., 2008). Nevertheless, in the dataset of this study the overall range of  $^{53}\text{Cr}/^{52}\text{Cr}$  and  $^{54}\text{Cr}/^{52}\text{Cr}$  ratios is larger for the static than for the multi-static measurements, indicating that at least for single-line static measurements, aging of the Faraday cups is the dominant factor causing the observed  $^{53}\text{Cr}/^{52}\text{Cr}$  versus  $^{54}\text{Cr}/^{52}\text{Cr}$  correlation.

## 2.4. Conclusions

This study compares the results of long-term high-precision Sr (i.e.,  $^{84}\text{Sr}/^{86}\text{Sr}$ ,  $^{87}\text{Sr}/^{86}\text{Sr}$ ) and Cr (i.e.,  $^{53}\text{Cr}/^{52}\text{Cr}$ ,  $^{54}\text{Cr}/^{52}\text{Cr}$ ) isotope measurements for the NIST SRM987 and NIST SR3112a standards, respectively, acquired on two thermal ionization mass spectrometers equipped with three different sets of Faraday cups having varying usage histories of between six years and one month. This extensive data set allows assessing the influence of Faraday cup deterioration on the precision and accuracy of the isotope measurements. Our results show that for static measurements drift and scatter of mass fractionation-corrected  $^{84}\text{Sr}/^{86}\text{Sr}$  and  $^{87}\text{Sr}/^{86}\text{Sr}$  as well as  $^{53}\text{Cr}/^{52}\text{Cr}$  and  $^{54}\text{Cr}/^{52}\text{Cr}$  ratios can be attributed to increasing deterioration of predominantly the center cup. For Sr isotopes, this problem can be overcome by dynamic measurements, which in this study provided stable and reproducible results over a period of 56 months for all three sets of Faraday cups used. For Cr isotopes, we find that the correlation between mass fractionated-corrected  $^{53}\text{Cr}/^{52}\text{Cr}$  and  $^{54}\text{Cr}/^{52}\text{Cr}$  ratios observed for static measurements in several prior studies can also largely be attributed to deterioration of the center cup. This residual correlation disappears when new Faraday cups are used, but appears again after only a few months of use and increases over time. Multi-static measurements minimize the long-term drift in mass fractionation-corrected  $^{53}\text{Cr}/^{52}\text{Cr}$  and  $^{54}\text{Cr}/^{52}\text{Cr}$  ratios, but a small residual correlation between  $^{53}\text{Cr}/^{52}\text{Cr}$  and  $^{54}\text{Cr}/^{52}\text{Cr}$  remains, which most likely reflects residual mass fractionation. Finally, the comparison to literature data for both Sr and Cr isotopes reveal that the effects of Faraday cup deterioration described here are not specific to the TIMS instruments of this study, but appear to be relatively common among TIMS instruments used for high-precision isotope measurements in other laboratories.



### 3. Distribution of *s*-, *r*-, and *p*-process nuclides in the early solar system inferred from Sr isotope anomalies in meteorites

#### Abstract

Nucleosynthetic isotope anomalies in meteorites allow distinguishing between the non-carbonaceous (NC) and carbonaceous (CC) meteorite reservoirs and show that correlated isotope anomalies exist in both reservoirs. It is debated, however, whether these anomalies reflect thermal processing of presolar dust in the disk or are primordial heterogeneities inherited from the solar system's parental molecular cloud. Here, using new high-precision  $^{84}\text{Sr}$  isotope data, we show that NC meteorites, Mars, and the Earth and Moon are characterized by the same  $^{84}\text{Sr}$  isotopic composition. This  $^{84}\text{Sr}$  homogeneity of the inner solar system contrasts with the well-resolved and correlated isotope anomalies among NC meteorites observed for other elements, and most likely reflects correlated *s*- and (*r*-, *p*-)-process heterogeneities leading to  $^{84}\text{Sr}$  excesses and deficits of similar magnitude which cancel each other. For the same reason there is no clearly resolved  $^{84}\text{Sr}$  difference between NC and CC meteorites, because in some carbonaceous chondrites the characteristic  $^{84}\text{Sr}$  excess of the CC reservoir is counterbalanced by an  $^{84}\text{Sr}$  deficit resulting from *s*-process variations. Nevertheless, most carbonaceous chondrites exhibit  $^{84}\text{Sr}$  excesses, which reflect admixture of refractory inclusions and more pronounced *s*-process heterogeneities in these samples. Together, the correlated variation of *s*- and (*r*-, *p*-)-process nuclides revealed by the  $^{84}\text{Sr}$  data of this study refute an origin of these isotope anomalies solely by processing of presolar dust grains, but points to primordial mixing of isotopically distinct dust reservoirs as the dominant process producing the isotopic heterogeneity of the solar system.

### 3.1. Introduction

Nucleosynthetic isotope anomalies reflect the heterogeneous distribution of isotopically anomalous presolar material and show that the solar accretion disk can be subdivided into the non-carbonaceous (NC) and carbonaceous (CC) meteorite reservoirs, which represent two spatially separated, but coexisting regions of the disk (Budde et al., 2016; Kruijer et al., 2017; Warren, 2011). Within this framework, the NC reservoir is typically associated with the inner disk, whereas the CC reservoir is thought to represent more distal disk regions and is possibly located beyond the orbit of Jupiter (Budde et al., 2016; Kruijer et al., 2017; Warren, 2011; Morbidelli et al., 2022). The origin of the NC-CC dichotomy, and more generally the processes that led to isotopic heterogeneity among meteorites and planets, are debated and processes associated with material infall from an isotopically heterogeneous molecular cloud core (Dauphas et al., 2002; Nanne et al., 2019; Burkhardt et al., 2019) or processing of presolar dust grains in the disk (e.g., Trinquier et al., 2009; Regelous et al., 2008, Paton et al., 2013) have been proposed. Furthermore, within each reservoir, isotope anomalies are often correlated, which has been interpreted to reflect mixing of isotopically distinct reservoirs in the disk (Alexander, 2019; Spitzer et al., 2020; Burkhardt et al., 2021; Hellmann et al., 2023).

The NC-CC isotopic dichotomy is evident for many of the Fe-peak elements (e.g., Ti, Cr, Ni), and also for several of the heavier elements such as Zr, Mo, and Ru (for recent reviews see Kleine et al., 2020; Kruijer et al., 2020; Bermingham et al., 2020). The isotope heterogeneities for these heavier elements are governed by variations in the relative abundances of nuclides produced in the proton-capture ( $p$ -process) as well as slow ( $s$ -process) and rapid ( $r$ -process) neutron-capture processes of stellar nucleosynthesis. Of these elements, Mo is uniquely useful because it can distinguish between  $s$ -process and  $r$ -process isotope variations. It shows that whereas  $s$ -process Mo isotope variations exist within both reservoirs, the CC reservoir is characterized by an  $r$ -process excess over the NC reservoir (e.g., Budde et al., 2016; Poole et al., 2017). This  $r$ -process excess has been interpreted to reflect a larger fraction of material in the CC reservoir with an isotopic composition as measured in Ca, Al-rich inclusions (CAIs), most of which display a more

pronounced *r*-process Mo excess than the CC reservoir (Burkhardt et al., 2019; Nanne et al., 2019; Brennecke et al., 2020). For other elements such as Zr and Ru, the distinction between *s*-process and *r*-process variations cannot easily be made, and so for these elements the characteristic *r*-process excess of the CC reservoir is partially masked by an on average larger *s*-process deficit in the CC over the NC reservoir (e.g., Akram et al., 2015; Fischer-Gödde and Kleine, 2017; Render et al., 2022).

A key element for further study of the nucleosynthetic isotope heterogeneity and the distribution of *p*-, *s*-, and *r*-process nuclides in the early solar system is strontium (Sr). Strontium has four stable isotopes ( $^{84}\text{Sr}$ ,  $^{86}\text{Sr}$ ,  $^{87}\text{Sr}$ ,  $^{88}\text{Sr}$ ), of which  $^{84}\text{Sr}$  is produced solely in the *p*-process,  $^{86}\text{Sr}$  and  $^{87}\text{Sr}$  are produced in the *s*-process, and  $^{88}\text{Sr}$  is produced by both, the *s*-process and the *r*-process. Furthermore,  $^{87}\text{Sr}$  is the decay-product of  $^{87}\text{Rb}$ , which over the life-time of the solar system produced radiogenic  $^{87}\text{Sr}$  variations that are orders of magnitude larger than any potential nucleosynthetic  $^{87}\text{Sr}$  heterogeneity (e.g., Papanastassiou and Wasserburg, 1978). Variations in  $^{87}\text{Sr}/^{86}\text{Sr}$  can, therefore, not be used to assess potential nucleosynthetic Sr isotope heterogeneities. As such, nucleosynthetic Sr isotope anomalies are commonly expressed as variations in the  $^{84}\text{Sr}/^{86}\text{Sr}$  ratio after mass-bias correction by internal normalization to  $^{88}\text{Sr}/^{86}\text{Sr}$ , and so variations in  $^{84}\text{Sr}$  can reflect heterogeneity in *p*-, *s*- and *r*-process Sr (Papanastassiou and Wasserburg, 1978). This makes nucleosynthetic Sr isotope variations a promising tool to investigate the distribution of *p*-, *r*-, and *s*-process nuclides in the early solar system.

Nucleosynthetic Sr isotope heterogeneity has been shown for acid leachates of primitive chondrites (Qin et al. 2011; Paton et al. 2013, Burkhardt et al., 2019), CAIs (Moynier et al., 2012; Hans et al., 2013), and several bulk meteorites, where Sr anomalies have predominantly been found for CC meteorites but also some NC meteorites (Fukai and Yokoyama, 2019; Hans et al., 2013; Henshall et al., 2018; Moynier et al., 2012; Paton et al., 2013; Yokoyama et al., 2015). However, overall Sr isotopes seem to show less systematic behavior than observed for the nucleosynthetic isotope anomalies of many other elements. For instance, it is unclear as to whether there is a systematic Sr isotope offset between NC and CC meteorites and whether there is Sr isotope heterogeneity in the NC reservoir. We present new high-precision  $^{84}\text{Sr}$  data for a comprehensive suite of meteorites, including

several samples for most of the major NC and CC meteorite groups. The new data are used to unravel the nature and extent of Sr isotope variations among meteorites, to assess the distribution of *p*-, *s*-, and *r*-process nuclides among meteorites and the terrestrial planets, and to constrain the processes responsible for generating the nucleosynthetic isotope heterogeneity in the early solar system.

### 3.2. Samples and analytical methods

Thirty-nine samples were selected for this study, including five terrestrial rocks, five lunar samples, and 29 meteorites from various chondrite and achondrite groups (Table 3). To avoid alteration induced by terrestrial weathering (Fukai and Yokoyama, 2019), we preferentially selected meteorite falls (n=19) and finds from Antarctica (n=9) and avoided finds from hot deserts (except NWA 4590).

Carbonaceous chondrites and the terrestrial sample JB2#2 were digested in Parr Bombs for 96 h at 190 °C using HF-HNO<sub>3</sub> (1:1) to facilitate complete digestion of refractory phases. All other samples were digested in Teflon beakers on a hotplate using a HF-HNO<sub>3</sub> (3:1) at > 140 °C for 72 h. After digestion, all samples were repeatedly re-dissolved and dried in *aqua regia* to dissolve residual fluorides. Strontium was purified by ion exchange chromatography following established procedures (e.g., Brennecka et al. 2013), with an additional purification step using Eichrom Sr-spec resin.

The Sr isotope measurements were performed using a ThermoScientific Triton *Plus* thermal ionization mass spectrometer (TIMS) at the University of Münster. The <sup>84</sup>Sr/<sup>86</sup>Sr ratios were measured using a two-line dynamic acquisition, where <sup>84</sup>Sr/<sup>86</sup>Sr measured in the first line is corrected for instrumental mass fractionation using <sup>86</sup>Sr/<sup>88</sup>Sr measured in the second line. The <sup>84</sup>Sr/<sup>86</sup>Sr and <sup>86</sup>Sr/<sup>88</sup>Sr ratios measured in this manner use the same Faraday cups, and so any bias induced by different cup efficiencies or amplifier gains cancel out (e.g., Hans et al., 2013; Yobregat et al., 2017). The dynamic <sup>84</sup>Sr/<sup>86</sup>Sr ratios show excellent agreement for all four sessions with a mean <sup>84</sup>Sr/<sup>86</sup>Sr = 0.0564907 ± 21 (2 s.d.) for the NIST SRM 987 standard, whereas the static <sup>84</sup>Sr/<sup>86</sup>Sr measurements exhibit significant drift, consistent with observations of prior studies (Hans et al., 2013; Henshall et al., 2018).

### 3.3. Nucleosynthetic Sr isotope variations among meteorites

The Sr isotopic data are reported as  $\mu^{84}\text{Sr}$  values, which represents the parts per  $10^6$  deviation of the mass-bias corrected  $^{84}\text{Sr}/^{86}\text{Sr}$  in a sample relative to the same ratio in the NIST SRM 987 standard ( $\mu^{84}\text{Sr} = [(^{84}\text{Sr}/^{86}\text{Sr})_{\text{sample}} / (^{84}\text{Sr}/^{86}\text{Sr})_{\text{SRM987}} - 1] \times 10^6$ ). The  $\mu^{84}\text{Sr}$  values of the terrestrial samples are indistinguishable from one another (average  $\mu^{84}\text{Sr} = 2 \pm 12$ , 2 s.d.) and from the NIST SRM 987 standard (Table 3, Fig. 13). This demonstrates the accuracy of our analytical methods and implies that the SRM 987 standard provides a good proxy for the  $\mu^{84}\text{Sr}$  of bulk Earth. This is consistent with prior studies that also employed a dynamic measurement routine (Hans et al. 2013; Yobregat et al. 2017; Henshall et al. 2018), but differs from results of some other studies, which based on static measurements found negative  $\mu^{84}\text{Sr}$  of approximately  $-20$  ppm for terrestrial samples (e.g., Moynier et al. 2012; Paton et al., 2013). This difference can likely be attributed to the larger uncertainty inherent in the static Sr isotope measurements and highlights the importance of using dynamic measurements to reliably resolve the anticipated small  $\mu^{84}\text{Sr}$  variations among meteorites.

The new Sr isotope data show that different samples from a given meteorite group have indistinguishable  $\mu^{84}\text{Sr}$  values, which makes it possible to calculate precise group means (Table 3; Fig. 13). The five lunar samples display a mean  $\mu^{84}\text{Sr}$  of  $-1 \pm 10$ , indicating that the Earth and Moon share the same  $\mu^{84}\text{Sr}$ . The four martian meteorites define a mean  $\mu^{84}\text{Sr}$  of  $12 \pm 12$ , which again is indistinguishable from the terrestrial and lunar values. Finally, for the four major NC meteorite groups investigated in this study (enstatite and ordinary chondrites, angrites, eucrites), all samples are indistinguishable from one another and provide precise mean  $\mu^{84}\text{Sr}$  values for each group as well a mean  $\mu^{84}\text{Sr} = 6 \pm 5$  (95% conf.) for the NC reservoir. This mean value overlaps with the composition of Earth, Moon, and Mars, and including these compositions results in a precise mean inner solar system  $\mu^{84}\text{Sr}$  value of  $5 \pm 4$  (95% conf.). Thus, the inner solar system appears to be homogeneous with respect to  $\mu^{84}\text{Sr}$ . This contrasts with results of some prior studies, which reported  $\mu^{84}\text{Sr}$  variations among NC meteorites of up to  $\sim 30$  ppm (Moynier et al., 2012; Paton et al., 2013).

**Table 3:** Sr isotope data for terrestrial and lunar samples and meteorites.

Group	Sample	Type	n	$\mu^{84}\text{Sr}$	$\pm$	$2\sigma$
Earth	AGV-2	Andesite	14	0	$\pm$ 7	
	BCR-2	Intraplate basalt	7	-1	$\pm$ 12	
	BCR-2#2	Intraplate basalt	6	1	$\pm$ 20	
	BCR-2#3	Intraplate basalt	10	13	$\pm$ 14	
	BCR-2#4	Intraplate basalt	5	3	$\pm$ 28	
	BHVO-2	Ocean island basalt	8	2	$\pm$ 9	
	BHVO-2#4	Ocean island basalt	5	-11	$\pm$ 22	
	JB-2	Ocean island basalt	8	4	$\pm$ 21	
	JB2#2	Ocean island basalt	4	-3	$\pm$ 11	
	BIR1a	Mid-ocean ridge basalt	7	2	$\pm$ 14	
	<i>Average</i>			2	$\pm$ 4	
Moon	60025.842 (241)	Ferroan anorthosite	8	-12	$\pm$ 14	
	10057	High-Ti mare basalt	8	5	$\pm$ 14	
	15495	Porphyritic basalt	5	5	$\pm$ 16	
	70017.825	High-Ti mare basalt	9	3	$\pm$ 18	
	12002.58	Porphyritic basalt	9	-7	$\pm$ 16	
	<i>Average</i>			-1	$\pm$ 10	
Mars	Zagami	Enriched shergottite	6	10	$\pm$ 23	
	MIL03346.76	Nakhlite	10	17	$\pm$ 14	
	RBT04262.75	Enriched Iherzolitic sher.	7	2	$\pm$ 11	
	Tissint	Enriched shergottite	10	18	$\pm$ 6	
	<i>Average</i>			12	$\pm$ 12	
Eucrites	Bouvante	Monomict eucrite	6	2	$\pm$ 15	
	Juvinas	Monomict eucrite	5	3	$\pm$ 15	
	Millbillilie	Polymict eucrite	7	4	$\pm$ 22	
	Moore County	Cumulate eucrite	4	9	$\pm$ 34	
	Pasamonte	Polymict eucrite	6	5	$\pm$ 20	
	Stannern	Monomict eucrite	7	11	$\pm$ 11	
	Stannern#2	Monomict eucrite	7	2	$\pm$ 11	
	<i>Average</i>			5	$\pm$ 3	
Angrites	D'Orbigny	Volcanic	6	14	$\pm$ 18	
	D'Orbigny#2	Volcanic	4	13	$\pm$ 27	
	D'Orbigny#3	Volcanic	8	12	$\pm$ 14	
	NWA 4590	Sub-volcanic	4	4	$\pm$ 30	
	<i>Average</i>			11	$\pm$ 7	
Ordinary Chondrites	Barwell	L5	6	-4	$\pm$ 23	
	Aumale	L6	6	8	$\pm$ 16	
	Leedey	L6	7	7	$\pm$ 12	
	<i>Average</i>			4	$\pm$ 16	
Enstatite Chondrites	ALHA 81021	EL6	9	5	$\pm$ 13	
	LAP10014.22	EL6	4	-7	$\pm$ 3	
	Khairpur	EL6	8	10	$\pm$ 10	
	Pillistfer	EL6	7	4	$\pm$ 20	
	<i>Average</i>			3	$\pm$ 11	

**Table 3 - continued:** Sr isotope data for terrestrial and lunar samples and meteorites.

Group	Sample	Type	n	$\mu^{84}\text{Sr}$	$\pm$	$2\sigma$
Carbonaceous Chondrites	Murchison	CM2	7	66	$\pm$	11
	Murchison#2	CM2	6	67	$\pm$	10
	Murchison#3	CM2	7	63	$\pm$	11
	MET 01070	CM1	6	60	$\pm$	17
	<i>Average</i>			64	$\pm$	3
	Allende	CV3	7	91	$\pm$	19
	Allende#2	CV3	9	65	$\pm$	15
	<i>Average</i>			78	$\pm$	37
	MIL09001	CR2	5	72	$\pm$	29
	DOM08006	CR2	6	70	$\pm$	15
	GRO95577	CR1	6	99	$\pm$	14
	GRA06100.58	CR2	5	70	$\pm$	46
	GRA06100.58#2	CR2	7	53	$\pm$	18
	<i>Average</i>			73	$\pm$	14
	Tarda	C2 ungr.	7	40	$\pm$	16
	Tagish Lake	C2 ungr.	7	9	$\pm$	12
	Orgueil	C11	5	20	$\pm$	22

**Notes.**  $\mu^{84}\text{Sr} = ({}^{84}\text{Sr}/{}^{86}\text{Sr}_{\text{sample}} / {}^{84}\text{Sr}/{}^{86}\text{Sr}_{\text{SRM987}} - 1) \times 10^6$ . Instrumental mass fractionation was corrected using by internal normalization to  ${}^{88}\text{Sr}/{}^{86}\text{Sr} = 8.3753$  and using the exponential law. *n* denotes number of individual measurements. Uncertainties are 95% conf. for  $n \geq 4$  and 2 s.d. for  $n < 4$ .

For example, Moynier et al. (2012) reported a  $\mu^{84}\text{Sr}$  of  $-36 \pm 6$  for enstatite chondrites based on static measurements of a single sample, and found a range of  $\mu^{84}\text{Sr}$  for ordinary chondrites from  $-43 \pm 10$  to  $-4 \pm 5$ . As for the terrestrial samples, the disparity between some of the previous data and the data of this study for NC materials most likely reflects the higher precision of the dynamic measurement routine combined with the more comprehensive sample set used in the present study. Most carbonaceous chondrites of this study exhibit more anomalous  $\mu^{84}\text{Sr}$  values but partly overlap with the NC composition (Fig. 13).

Whereas CV, CM, and CR have  ${}^{84}\text{Sr}$  excesses of between  $\sim 64$  and  $\sim 78$  ppm, the CI chondrite Orgueil and the two ungrouped chondrites Tagish Lake (TL) and Tarda exhibit lower  $\mu^{84}\text{Sr}$  that partly overlap with those of NC meteorites (Table 3, Fig. 13). This agrees with results of prior studies, which also showed that carbonaceous chondrites display variable  ${}^{84}\text{Sr}$  excesses (e.g., Yokoyama et al., 2015; Fukai and Yokoyama, 2019). However, the  $\mu^{84}\text{Sr}$  value for CR chondrites of this study is more elevated (mean  $\mu^{84}\text{Sr} = 73 \pm 33$ ) than  $\mu^{84}\text{Sr}$  values of  $\sim 0$  reported for two CR chondrite desert finds in earlier studies (Moynier et al., 2012; Fukai and Yokoyama, 2019). This difference almost certainly reflects terrestrial

alteration in these desert finds (Fukai and Yokoyama, 2019), which is absent in the CR chondrites of this study, all of which are finds from Antarctica. Finally, for the CI chondrite Orgueil,  $\mu^{84}\text{Sr} = 20 \pm 22$  determined here agrees with  $\mu^{84}\text{Sr} = -1 \pm 25$  for Orgueil and  $18 \pm 25$  for the CI chondrite Yamato 980115 (Fukai and Yokoyama, 2019), but is slightly lower than, albeit not resolved from  $\mu^{84}\text{Sr} = 42 \pm 17$  reported for Orgueil (Moynier et al., 2012) and  $\mu^{84}\text{Sr} = 37 \pm 10$  reported for the CI chondrite Ivuna (Paton et al., 2013). These slightly higher  $\mu^{84}\text{Sr}$  values probably reflect incomplete digestion of acid-resistant presolar grains such as SiC (Fukai and Yokoyama 2019).

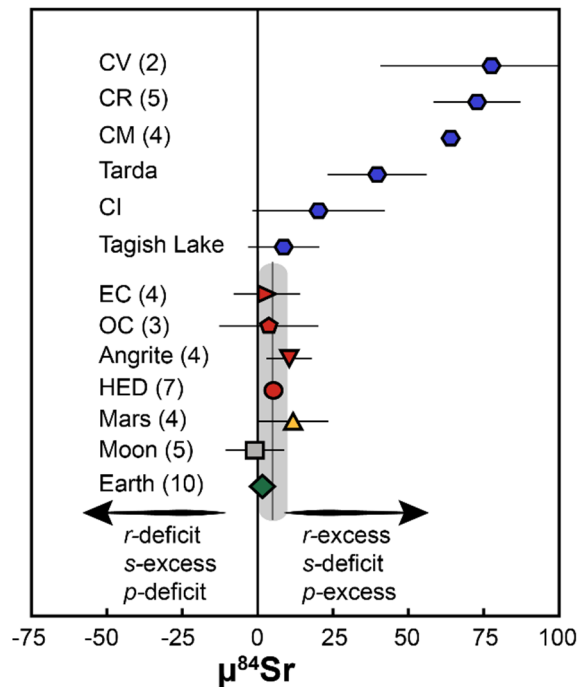


**Figure 13:** Average  $\mu^{84}\text{Sr}$  values of terrestrial, lunar, and meteoritic samples measured in this study. Uncertainties are 95% conf. for  $n \geq 4$  and 2 s.d. for  $n < 4$ . Grey box represents inner solar system average of  $\mu^{84}\text{Sr} = 5 \pm 4$  (95% conf.). Arrows indicate effect of excesses and deficits in  $s$ -,  $r$ -, and  $p$ -process Sr on  $\mu^{84}\text{Sr}$ .

### 3.4. Origin of $^{84}\text{Sr}$ variations in the solar system

The new data of this study reveal that the  $^{84}\text{Sr}$  systematics of meteorites differ in two important ways from other elements. First, there are no resolved  $^{84}\text{Sr}$  variations within the NC reservoir. This differs from the isotope anomalies for many other elements, which exhibit well-resolved and correlated isotope variations among NC meteorites, Mars, and the Earth and Moon. Given this ubiquitous isotope heterogeneity among NC meteorites, which is present for all elements showing nucleosynthetic isotope anomalies in carbonaceous chondrites or their components, it appears highly unlikely that  $^{84}\text{Sr}$  is indeed homogeneous in the NC reservoir. Second, the  $\mu^{84}\text{Sr}$  values of NC and CC meteorites are not separated by a gap, but partly overlap. This contrast with several other elements, where NC and CC meteorites define two distinct compositional clusters. As we will show below, this contrasting behavior of Sr likely results from the superimposed effects of (*p*-, *r*-) and *s*-process heterogeneities, which reduce the overall  $^{84}\text{Sr}$  variations within and between the NC and CC reservoirs.

#### 3.4.1 $^{84}\text{Sr}$ homogeneity of the inner solar system

The nucleosynthetic isotope heterogeneity among meteorites is governed by isotope anomalies in the Fe-peak elements (Ca, Ti, Cr, Ni, Zn), which are mainly produced by nuclear statistical equilibrium (NSE) and explosive nucleosynthesis in (pre-)supernovae massive stars, and anomalies in heavier elements such as Zr, Mo, and Ru associated with variations in the abundance of *p*-, *r*-, and *s*-process nuclides (e.g. Woosley and Heger, 2002; Pignatari et al., 2016). Whereas the CC reservoir is characterized by excesses in nuclides produced in neutron-rich stellar environments (e.g.,  $^{50}\text{Ti}$ ,  $^{54}\text{Cr}$ , *r*-process Mo), the NC reservoir exhibits deficits in these nuclides, relative to the terrestrial standard (e.g., Kleine et al., 2020). There are additional *s*-process variations in both reservoirs, which in the NC reservoir are correlated with the isotope anomalies in the Fe-peak elements and the variation in the relative abundance of *r*-process Mo (e.g., Spitzer et al., 2020). Thus,  $\mu^{84}\text{Sr}$  variations among and between NC and CC meteorites might be expected due to (*i*) *s*-process variations in both reservoirs, (*ii*) the *r*-process NC-CC difference, and (*iii*) *r*-process variations in the NC reservoir. Understanding the extent of  $^{84}\text{Sr}$  variations among meteorites, therefore, requires

disentangling the individual contributions of the specific  $s$ -,  $r$ -, and  $p$ -process variations to the  $\mu^{84}\text{Sr}$  value of any given sample.

To quantitatively assess the expected  $\mu^{84}\text{Sr}$  variations, we will start with the variations expected from the heterogeneous distribution of nuclides produced in neutron-rich stellar environments. For Sr this includes  $r$ - and  $p$ -process variations, which result in the same  $^{84}\text{Sr}$  signatures; for instance, the  $^{84}\text{Sr}$  excesses in CAIs have been interpreted to reflect either an  $r$ -process (Hans et al., 2013) or  $p$ -process excess (Charlier et al., 2021). For the model of this study, the distinction between  $r$ - and  $p$ -process variations is not important, which we will therefore treat together. We begin with the observation that the isotopic composition of the CC reservoir is always intermediate between those of the NC reservoir and CAIs (Nanne et al., 2019; Burkhardt et al., 2019). This observation has led to a model which attributes the ultimate origin of the NC-CC isotopic difference to time-varied infall from an isotopically heterogeneous molecular cloud, followed by mixing within the disk (Nanne et al., 2019; Burkhardt et al., 2019; Jacquet et al., 2019). In this model, CAIs represent the isotopic composition of the early infall, while NC meteorites record the isotopic composition of the late infall. The isotopic composition of the CC reservoir is then attributed to mixing of NC material with material having a CAI-like isotopic but broadly chondritic bulk chemical composition (termed ‘IC reservoir’ for Inclusion-like Chondritic reservoir; Burkhardt et al., 2019).

The nucleosynthetic variations within the NC reservoir are on the same trajectory as the NC-CC-IC offset, and so both the NC-CC isotopic difference as well as the isotopic variations within the NC reservoir can be understood as the result of mixing between the same two reservoirs, namely the IC reservoir and a reservoir having the starting composition of the NC reservoir (Fig. 14a). The fraction of IC material in the NC reservoir is then given by mass balance where  $\mu_{IC}$  is given by CAIs, and  $\mu_{NC,high}$  and  $\mu_{NC,low}$  represent the isotopic compositions of the two extremes of the NC isotope trend:

*Equation 7*

$$f_{IC,NC} = \frac{\mu_{NC,high} - \mu_{NC,low}}{\mu_{IC} - \mu_{NC,low}}.$$

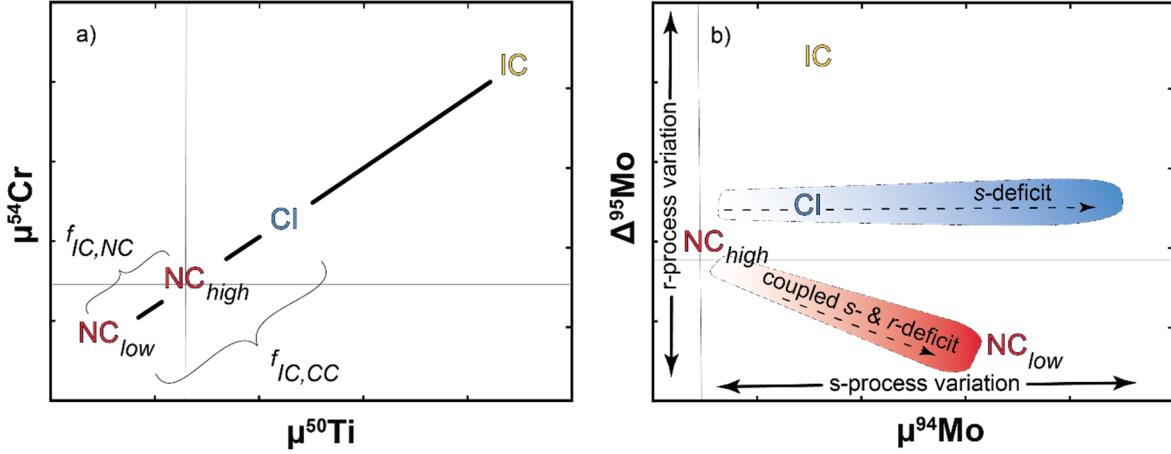


**Figure 14:** Schematic plots illustrating the mixing model of this study. a) Plot of  $\mu^{50}\text{Ti}$  vs.  $\mu^{54}\text{Cr}$  showing the location of the three components used in the mixing model: *IC*, *NC<sub>low</sub>*, *NC<sub>high</sub>*. Fractions  $f_{IC,NC}$  and  $f_{IC,CC}$  can be calculated by assuming that *NC<sub>high</sub>* and *CI* are mixtures of *NC<sub>low</sub>* and *IC* (see text for details). b) Plot of  $\mu^{94}\text{Mo}$  vs.  $\Delta^{95}\text{Mo}$ . For definition of  $\Delta^{95}\text{Mo}$  see text. Variations in  $\Delta^{95}\text{Mo}$  reflect *r*-process variations, whereas variations in  $\mu^{94}\text{Mo}$  mostly reflect *s*-process variation. The position of the mixing endmembers *IC* and *NC<sub>low</sub>* are indicated, as well as the resulting compositions of *NC<sub>high</sub>* and *CI*. For details about the model see text.

The value of  $f_{IC,NC}$  can be calculated for those elements whose isotopic composition in CAIs is well known and which exhibit sufficient isotope variation among NC meteorites. This includes  $^{48}\text{Ca}$ ,  $^{50}\text{Ti}$ ,  $^{54}\text{Cr}$ , and Mo. For Mo, this requires isolating the *s*- and *r*-process variations from each other. For this purpose, Budde et al. (2019) introduced the  $\Delta^{95}\text{Mo}$  notation, which provides the deviation of a sample's Mo isotopic composition from a theoretical *s*-process mixing line and, as such, is a measure of *r*-process Mo variations. All four elements provide consistent  $f_{IC,NC}$  values with a weighted mean of  $0.16 \pm 0.02$  (Fig. 15, Table A3.1 and A3.2).

Earth typically plots at one end of the NC isotope trend, defining the value of  $\mu_{NC,high}$  in equation 7. As  $\mu$ -values are calculated relative to the composition of the terrestrial standard and because the isotopic composition of Earth is typically close to that of the standard, we will for simplicity assume  $\mu_{NC,high} \approx 0$ . Rearranging equation 7 we have:

Equation 8

$$\mu_{NC,low} = \frac{-f_{IC,NC} \times \mu_{IC}}{1 - f_{IC,NC}} .$$

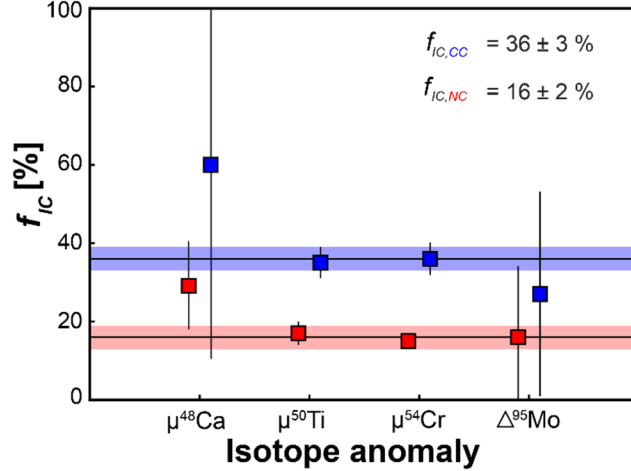


**Figure 15:** Fraction of IC material in the NC and CC reservoirs calculated using equations 7 and 9. Data used in these calculations are summarized in Table A3.1.

Using the mean  $\mu^{84}\text{Sr} = 131 \pm 11$  (95% conf.) of CAIs (Brennecka et al. 2013; Hans et al. 2013; Paton et al., 2013; Myoyo et al., 2018; Brennecka et al., 2020; Charlier et al. 2021) for  $\mu_{IC}$  and  $f_{IC,NC} = 0.16 \pm 0.02$  yields an expected  $\mu^{84}\text{Sr}_{NC,low}$  value of  $-24 \pm 6$ . In other words, *without s-process variations* the NC reservoir would be expected to have a range of  $\mu^{84}\text{Sr}$  values from  $-24 \pm 6$  for the most (*r*-, *p*-) process depleted bodies (e.g., ureilites) to  $\sim 0$  for enstatite chondrites and the Earth (Fig. 16, Table A3.2).

However, in addition to (*r*-, *p*-) process variations, NC meteorites also display correlated *s*-process variations, which range from only small *s*-process deficits in enstatite chondrites to larger deficits in, for instance, IIAB iron meteorites (e.g., Budde et al., 2019; Spitzer et al., 2020). To quantify the effect of these *s*-process variations on  $\mu^{84}\text{Sr}$ , we will take Mo as a proxy. The  $\mu^{94}\text{Mo}$  variations among NC meteorites are dominated by *s*-process variations with  $\mu^{94}\text{Mo}$  values ranging from  $\sim 0$  for IAB iron meteorites and winonaites to  $\sim 120$  for IIAB iron meteorites (Budde et al., 2019; Spitzer et al., 2020). On the basis of Mo and Sr isotopic data for presolar SiC grains (Nicolussi et al., 1998), acid leachates of primitive chondrites (Burkhardt et al., 2019), and *s*-process theory (Arlandini et al., 1999; Bisterzo et al., 2014; Dauphas et al., 2014b), we estimate that *s*-process heterogeneity results in  $0.31 \pm 0.07$  times smaller  $\mu^{84}\text{Sr}$  than  $\mu^{94}\text{Mo}$  variations (Burkhardt et al., 2019). Consequently, an *s*-process deficit of  $\mu^{94}\text{Mo} = 120$  corresponds to an expected *s*-process  $\mu^{84}\text{Sr}$  anomaly

of  $36 \pm 10$ . This expected *s*-process  $\mu^{84}\text{Sr}$  anomaly is of similar magnitude but opposite sign than the corresponding expected (*r*-, *p*-)-process  $\mu^{84}\text{Sr}$  anomaly of  $-24 \pm 6$  from above. Due to the correlated nature of the *s*- and *r*-process variations among NC meteorites (Fig. 14b), samples with the largest (*r*-, *p*-)-process effects on  $\mu^{84}\text{Sr}$  also have the largest *s*-process anomaly, while samples with the smallest (*r*-, *p*-)-process anomaly also have the smallest *s*-process anomaly. Thus, for all NC samples the resulting positive (*s*-process) and negative (*r*-, *p*-process)  $\mu^{84}\text{Sr}$  anomalies cancel out, which leads to the observed  $\mu^{84}\text{Sr}$  values close to 0 throughout the NC reservoir (Fig. 16).

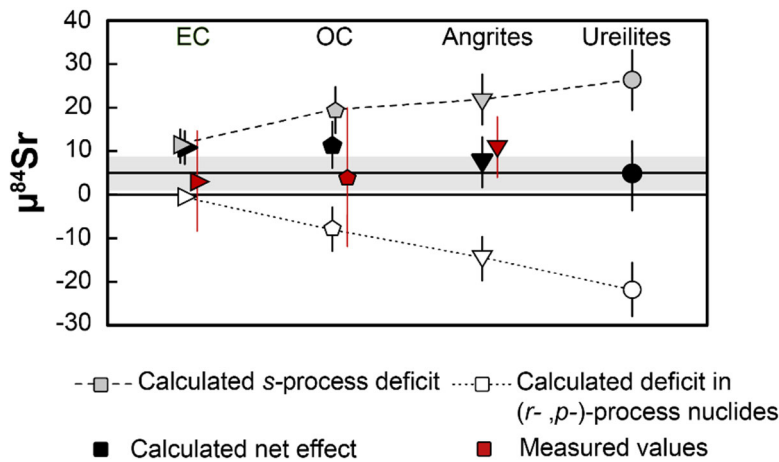


**Figure 16:** Expected  $\mu^{84}\text{Sr}$  anomalies for enstatite chondrites (EC), ordinary chondrites (OC), angrites, and ureilites resulting from only *s*- and only (*r*-, *p*-)-process variations. These variations lead to  $\mu^{84}\text{Sr}$  variations of opposite sign but similar magnitude, and so no resolvable  $\mu^{84}\text{Sr}$  variations remain among NC meteorites. Measured  $\mu^{84}\text{Sr}$  values for EC, OC, and angrites are shown for comparison and are well reproduced by the model. There are no  $\mu^{84}\text{Sr}$  data for ureilites, but they are also predicted to have  $\mu^{84}\text{Sr} \approx 0$ . Grey band represents the inner solar system average  $\mu^{84}\text{Sr} = 5 \pm 4$  (95% conf.). Data is summarized in Table A3.2.

### 3.4.2 $^{84}\text{Sr}$ offset between NC and CC meteorites

The model from above can also be used to assess the expected  $\mu^{84}\text{Sr}$  difference between NC and CC meteorites. For a refractory element like Sr, the Sr isotopic composition of carbonaceous chondrites can be strongly affected by the admixture of CAIs, and so for assessing the characteristic offset between the NC and CC reservoirs it is useful to use carbonaceous chondrites which contain only little CAIs, such as CI chondrites. For the CC reservoir, equation 7 takes the form:

Equation 9

$$f_{IC,CC} = \frac{\mu_{CI} - \mu_{NC,low}}{\mu_{IC} - \mu_{NC,low}}.$$

Similar to the calculation for the NC reservoir, values for  $f_{IC,CC}$  can be calculated using data for  $^{48}\text{Ca}$ ,  $^{50}\text{Ti}$ ,  $^{54}\text{Cr}$ , and  $\Delta^{95}\text{Mo}$ , and using the composition of CAIs to represent  $\mu_{IC}$  and the composition of ureilites to represent  $\mu_{NC,low}$  (Table A3.1). We find a mean  $f_{IC,CC} = 0.36 \pm 0.03$  (Fig. 15), which can be used to calculate the expected  $\mu^{84}\text{Sr}$  for CI chondrites:

Equation 10

$$\mu_{CI} = f_{IC,CC} \times \mu_{IC} + (1 - f_{IC,CC}) \times \mu_{NC,low}.$$

Using the mean  $\mu^{84}\text{Sr} = 131 \pm 11$  of CAIs for  $\mu_{IC}$ ,  $f_{IC,CC} = 0.36 \pm 0.06$ , and  $\mu^{84}\text{Sr} = -24 \pm 6$  for  $\mu_{NC,low}$  provides an expected  $\mu^{84}\text{Sr}$  value for CI chondrites of  $32 \pm 16$ . This value is calculated solely based on the expected ( $r$ -,  $p$ -)-process  $\mu^{84}\text{Sr}$  variations, but there are additional  $s$ -process variations affecting the  $^{84}\text{Sr}$  isotopic composition of carbonaceous chondrites. To assess the magnitude of these  $s$ -process variations, we again take  $^{94}\text{Mo}$  as a proxy. The  $\mu^{94}\text{Mo}$  values of IIAB irons (which have the largest  $s$ -process deficit and hence define  $\mu_{NC,low}$  for Mo) and CI chondrites differ by  $\sim 40$  ppm ( $\mu^{94}\text{Mo} \approx 120$  for IIAB irons and  $\approx 80$  for CI chondrites), which predominantly reflect  $s$ -process variations. Using the 0.31 ratio between  $\mu^{84}\text{Sr}$  and  $\mu^{94}\text{Mo}$   $s$ -process variations implies that the expected  $\mu^{84}\text{Sr}$  for CI chondrites needs to be lowered by  $\sim 12$  ppm, resulting in an overall expected  $\mu^{84}\text{Sr} = 20 \pm 17$ . This value overlaps with the measured  $\mu^{84}\text{Sr} = 20 \pm 22$  for Orgueil from this study, indicating that the lack of a clearly resolved  $\mu^{84}\text{Sr}$  difference between NC and CC meteorites reflects the counteracting effects of  $s$ - and  $r$ -process variations.

### 3.4.3 Origin of $^{84}\text{Sr}$ variations among carbonaceous chondrites

Prior studies have shown that the variable abundances of CAIs exert a strong control on the  $^{84}\text{Sr}$  isotopic composition of bulk carbonaceous chondrites (Fukai and Yokoyama, 2018; Burkhardt et al., 2019), which is consistent with the elevated  $\mu^{84}\text{Sr}$  values of the relatively CAI-rich CV chondrites reported in this and prior studies. However, this study reports the first precise  $^{84}\text{Sr}$  data for CR chondrites, which contain only few CAIs but display the same  $\mu^{84}\text{Sr}$  value as the CAI-rich CV chondrites. Consequently, variable abundances of

CAIs cannot be the sole cause of  $\mu^{84}\text{Sr}$  variations among the carbonaceous chondrites. CR chondrites are characterized by one of the largest *s*-process deficits with a  $\mu^{94}\text{Mo}$  value of  $\sim 280$  (Budde et al., 2018). For comparison, CI chondrites display  $\mu^{94}\text{Mo} \approx 80$ , and so there is a  $\sim 200$  ppm  $\mu^{94}\text{Mo}$  difference between the CR and CI chondrites. This corresponds to an *s*-process-induced  $\mu^{84}\text{Sr}$  difference between these two carbonaceous chondrites of  $\sim 60$  ppm (for *s*-process variations  $\mu^{84}\text{Sr} \approx 0.31 \times \mu^{94}\text{Mo}$ ; see above) and fully accounts for the more elevated  $\mu^{84}\text{Sr}$  of  $\sim 73$  for CR chondrites compared to CI chondrites ( $\mu^{84}\text{Sr} \approx 20$ ). Thus, not all the  $^{84}\text{Sr}$  variations among carbonaceous chondrites are attributable to the heterogeneous distribution of CAIs, but may also reflect *s*-process variations.

### 3.5. Implications for the origin of nucleosynthetic variability in the disk

It has been suggested that the nucleosynthetic isotopic heterogeneity of the solar protoplanetary disk reflects thermal processing of presolar dust grains (e.g., Trinquier et al. 2009; Paton et al. 2013). For instance, on the basis of apparent negative  $\mu^{84}\text{Sr}$  values for some NC meteorites and Earth (relative to the terrestrial standard), Paton et al. (2013) argued that inner solar system bodies are enriched in *s*-process Sr, which is carried by presolar SiC grains, and where the SiC enrichment results from the removal of thermally labile components by thermal processing of dust in the inner disk. However, the new  $^{84}\text{Sr}$  data of this study reveal that neither there are  $^{84}\text{Sr}$  variations among inner solar system bodies, nor are any of these bodies characterized by negative  $\mu^{84}\text{Sr}$  values (Fig. 13). This strongly argues against thermal processing as a mechanism to produce the nucleosynthetic isotope heterogeneity of the disk, because the resulting enrichment in thermally resistant carriers such as SiC would, as shown by Paton et al. (2013), result in variable  $\mu^{84}\text{Sr}$  among NC meteorites.

In addition, the lack of resolvable  $^{84}\text{Sr}$  variations among NC meteorites indicates correlated heterogeneity of *s*-process- and (*r*-, *p*-)-process-derived Sr. Producing such correlated isotope variations by thermal processing of presolar dust grains is highly unlikely, because any given *s*-process excess resulting from thermal processing would have to be balanced by the appropriate excess in (*r*-, *p*-)-process carriers. In other words, the thermal processing would have to fortuitously result in coupled enrichments of distinct presolar

carriers such that no resolvable  $^{84}\text{Sr}$  anomaly is produced. While this may happen for individual samples by chance, it seems highly unlikely that this consistently occurred for all NC meteorites and resulted in the observed variable and correlated *s*-process and (*r*-, *p*-)-process isotope variations. This is in line with the observation that among NC meteorites correlated isotope variations exist for elements of different stellar origins (supernovae, AGB stars) and having distinct geochemical (lithophile, siderophile) and cosmochemical (refractory, volatile) properties (Spitzer et al., 2020; Burkhardt et al., 2021). Such multi-elemental correlations of isotope anomalies cannot reflect thermal processing of distinct presolar carriers in the disk, because different elements and carrier phases are expected to have reacted differently to such processing. As such, the results of this study support models in which the nucleosynthetic isotope heterogeneity of the disk is inherited from the solar system's parental molecular cloud, with additional variations resulting from subsequent mixing within the disk.

### 3.6. Appendix Chapter 3

**Table A3.1:** Ca, Ti, Cr and Mo isotope anomaly data for various meteorite groups.

Meteorite Group	$\mu^{48}\text{Ca}$	$\mu^{50}\text{Ti}$	$\mu^{54}\text{Cr}$	$\Delta^{95}\text{Mo}$
NC <sub>high</sub> *	0 ± 5	0 ± 2	9 ± 13	3 ± 15
Enstatite Chondrites	-37 ± 46	2 ± 8	4 ± 5	-9 ± 4
Ordinary Chondrites	-28 ± 20	-66 ± 6	-40 ± 4	-15 ± 8
Angrites	-106 ± 33	-118 ± 8	-43 ± 6	-6 ± 9
Ureilites	-182 ± 44	-185 ± 26	-92 ± 4	-15 ± 7
CI Chondrites	205 ± 20	185 ± 12	159 ± 6	22 ± 34
CAI	468 ± 205	877 ± 53	597 ± 52	124 ± 14

**Note:** Data are from Spitzer et al. (2020) for  $\mu^{50}\text{Ti}$ ,  $\mu^{54}\text{Cr}$  and  $\Delta^{95}\text{Mo}$ ; Burkhardt et al. (2019) for  $\mu^{48}\text{Ca}$  values; Schneider et al. (2020) for  $\mu^{54}\text{Cr}$  of BSE and  $\mu^{48}\text{Ca}$  for CAIs are given in Render et al. (2022).

\* NC<sub>high</sub> is represented by Bulk Silicate Earth (BSE) for  $\mu^{48}\text{Ca}$ ,  $\mu^{50}\text{Ti}$ ,  $\mu^{54}\text{Cr}$  and by NWA 2526 for  $\Delta^{95}\text{Mo}$  [BSE cannot be used due to mixed composition (Budde et al., 2019)]

**Table A3.2:** Predicted and measured Sr isotopic compositions.

Meteorite Group	$f_{\text{IC,NC}}$	Predicted $\mu^{84}\text{Sr}$ from (r,p)-process variations	Predicted $\mu^{84}\text{Sr}$ from s-process variations <sup>a</sup>	Predicted bulk $\mu^{84}\text{Sr}$	Measured $\mu^{84}\text{Sr}$
Enstatite Chondrites	0.00 ± 0.01	-2 ± 4	13 ± 4	11 ± 6	3 ± 11
Ordinary Chondrites	0.07 ± 0.01	-8 ± 5	21 ± 6	13 ± 8	4 ± 16
Angrites	0.11 ± 0.01	-14 ± 5	23 ± 6	9 ± 8	11 ± 7
Ureilites	0.16 ± 0.02	-24 ± 6	28 ± 7	4 ± 9	
IIAB*			36 ± 9		
CI	0.36 ± 0.03	32 ± 16	-12 ± 6	20 ± 17	20 ± 22

\* maximum NC range

<sup>a</sup>Values are calculated by applying a slope of  $0.31 \pm 0.07$  for the s-process  $\mu^{84}\text{Sr}$ - $\mu^{94}\text{Mo}$  correlation (Burkhardt et al., 2019) on the range of observed  $\mu^{94}\text{Mo}$  anomalies. This slope is based on Mo and Sr isotopic data for presolar SiC grains (Nicolussi et al., 1998), acid leachates of primitive chondrites (Burkhardt et al., 2019), and main component s-process yields from Arlandini et al. (1999), using the formalism given by Dauphas et al. (2014b). The slope increases to 0.36 if the higher s-process yields from Bisterzo et al. (2014) are used, which would result in a positive shift in the predicted bulk  $\mu^{84}\text{Sr}$  values of 2, 3, 4, and 4 ppm for the OC, NC, angrites, and ureilites, respectively. This shift is within the uncertainty of our calculations and does not affect the qualitative evidence of our mixing model.



## 4. Strontium isotope evidence for formation of the Moon ~ 4.5 billion years ago

### Abstract

The formation of the Moon by a giant impact onto proto-Earth marks the end of terrestrial planet formation in the solar system. However, the timing of this event is controversial, with estimates ranging from ~ 50 and ~ 210 million years (Ma) after solar system formation. The  $^{87}\text{Rb}$ - $^{87}\text{Sr}$  system has the potential to resolve this debate, as formation of the Moon resulted in strong fractionation of rubidium from strontium. We report rubidium-strontium isotope data for lunar ferroan anorthosites which precisely constrain the initial  $^{87}\text{Sr}/^{86}\text{Sr}$  ratio of the Moon. In all models of the Moon-forming impact that account for the isotopic homogeneity of the Earth and Moon, this  $^{87}\text{Sr}/^{86}\text{Sr}$  requires formation of the Moon  $65 \pm 20$  Ma after solar system formation. This new estimate is consistent with the relation between the mass of the late veneer on Earth and the age of the Moon predicted in dynamical models of terrestrial planet formation.

## 4.1. Introduction

The Moon is thought to have formed as the result of a giant impact of an object called 'Theia' with proto-Earth near the end of Earth's accretion (Canup and Asphaug, 2001), marking the end of terrestrial planet formation in the solar system. However, despite its importance, until now the time of Moon formation has not been determined precisely, and current estimates range from  $\sim 4.5$  to  $\sim 4.36$  billion years (Ga) (Halliday, 2008; Nemchin et al., 2009; Borg et al., 2011, 2019; Barboni et al., 2017; Maurice et al., 2020; Greer et al., 2023).

The most common approach to date the Moon is by dating the different rock types assumed to have crystallized from the lunar magma ocean (LMO), which had formed as a result of the enormous thermal energy released by the giant impact (Smith et al., 1970; Warren, 1985). Solidification of the LMO led to chemical differentiation of the Moon through the separation of dense mafic cumulates from buoyant plagioclase-rich cumulates, which formed the ferroan anorthosites (FAN) that dominate the lunar crust (Wood et al., 1970; Warren, 1985; Elardo et al., 2011). The end of LMO crystallization is commonly associated with the formation of a residual liquid referred to as KREEP [for strong enrichments in potassium (K), rare earth elements (REE), and phosphorus(P); (Warren and Wasson, 1979)], and the crystallization ages of the Mg-suite, which represent melts intruded into the earlier-formed anorthositic crust (Borg et al., 2017; Zhang et al., 2021).

Formation ages for the different early- and late-formed products of the LMO consistently return ages of  $\sim 4.35$  Ga, including the crystallization age of FANs (Borg et al., 2011; Sio et al., 2020), which are thought to have formed soon after the Moon's formation (Elkins-Tanton et al., 2011), and model ages for the formation of KREEP (Sprung et al., 2013; Gaffney and Borg, 2014), which mark the end of LMO crystallization. This consistency of ages has been interpreted to indicate a rapid crystallization of the LMO at  $\sim 4.35$  Ga, which in turn would imply that the Moon formed at around this time, i.e.,  $\sim 210$  Ma after solar system formation (Borg et al., 2011, 2019; Sio et al., 2020; Borg and Carlson, 2023). This interpretation, however, is difficult to reconcile with several other observations. First, thermal evolution models of the Moon predict that LMO solidification should have lasted  $\sim 100$  Ma (Maurice et al., 2020), such that FANs are expected to have formed significantly

earlier than the KREEP source. However, until now only a single FAN sample has been precisely dated (Borg et al., 2011, 2015), and as such it is unclear as to whether this single age is representative for the formation period of all FANs. Second, formation of the Moon at ~ 4.35 Ga is inconsistent with the occurrence of rare lunar zircons with crystallization ages at around 4.45 Ga (Nemchin et al., 2009; Greer et al., 2023), and with the  $^{176}\text{Lu}$ - $^{176}\text{Hf}$  isotope systematics of lunar zircons, which has been interpreted to indicate formation of the KREEP source as early as ~ 4.5 Ga (Barboni et al., 2017). Together, these inconsistencies highlight the difficulty of reliably linking the ages of the various LMO products to a formation time of the Moon.

An alternative way of dating the formation of the Moon is to determine the time of a major chemical fractionation in the Moon that occurred during or immediately after the giant impact. The Moon is strongly depleted in moderately volatile elements (Wolf and Anders, 1980), which has been attributed to incomplete condensation of the proto-Moon (Lock et al., 2018) or volatile loss from the molten Moon (Charnoz et al., 2021), implying the volatile element loss occurred immediately after Moon's formation. Because Rb is moderately volatile, while Sr is refractory, the  $^{87}\text{Rb}$ - $^{87}\text{Sr}$  isotope system can potentially be used to determine the age of the Moon by dating volatile loss from the Moon. Based on the assumption that the Rb-Sr data of a single FAN sample record the initial Sr isotope composition of the Earth-Moon system, it has been argued that the Moon formed at around ~ 4.5 Ga (Halliday, 2008; Mezger et al., 2021). To more rigorously explore the utility of the Rb-Sr system to date the Moon, we obtained high-precision Rb-Sr data for a larger set of FANs to better define the initial Sr isotope composition of the Moon, and use the new data to model the Rb-Sr isotope evolution of the Earth-Moon system within the framework of current lunar formation models. Our results show that the Rb-Sr data provide a robust age for the formation of the Moon.

## 4.2. Results

For this study, eight FANs collected by the Apollo 15 and 16 missions were selected: 15415, 60025, 60015, 61015, 62255, 65315, 65325, and 67075. The sample selection was guided by (i) the presence of large anorthite crystals, which more readily allows for separating undisturbed mineral grains, (ii) low reported Rb concentrations, which is essential for precisely determining a sample's initial  $^{87}\text{Sr}/^{86}\text{Sr}$ , and (iii) low reported  $^{87}\text{Sr}/^{86}\text{Sr}$  values and/or other evidence for old formation ages (Table A4.1). In total, 14 different fractions from eight ferroan anorthosite samples were measured. Of these, 10 samples are plagioclase separates ('-p'), three bulk samples ('-b'), one residue after hand picking ('-r'), and one sieved fine fraction ('-f'; < 125  $\mu\text{m}$ ). The Rb and Sr concentrations, and  $^{87}\text{Sr}/^{86}\text{Sr}$  ratios were determined by thermal ionization mass spectrometry, after chemical separation of Rb and Sr (see section 4.4.1).

**Table 4:** Rb-Sr isotopic data for ferroan anorthosites.

Sample	Type <sup>a</sup>	Weight (mg)	Rb (ppm)	Sr (ppm)	$^{87}\text{Rb}/^{86}\text{Sr}^b$	n	$^{87}\text{Sr}/^{86}\text{Sr}^b$
15415	Plagioclase	30.0	0.045 ± 0.002	157 ± 2	0.00083 ± 4	2	0.699120 ± 6
60025	Plagioclase	16.9	0.022 ± 0.001	183 ± 2	0.00035 ± 2	5	0.699082 ± 2
60025	Plagioclase	15.9	0.030 ± 0.002	188 ± 2	0.00047 ± 2	3	0.699089 ± 2
60015	Plagioclase	18.0	0.034 ± 0.002	161 ± 2	0.00062 ± 3	1	0.699102 ± 7
61015	Plagioclase	6.0	0.051 ± 0.003	169 ± 2	0.00090 ± 5	1	0.699117 ± 2
61015	Bulk rock	27.4	0.233 ± 0.012	193 ± 2	0.00350 ± 18	4	0.699273 ± 2
61015	Fines	29.3	0.103 ± 0.005	185 ± 2	0.00160 ± 8	4	0.699163 ± 2
62255	Plagioclase	15.2	0.032 ± 0.002	157 ± 2	0.00059 ± 4	1	0.699098 ± 2
62255	Plag. residue	16.0	0.033 ± 0.002	157 ± 2	0.00059 ± 3	4	0.699098 ± 1
65315	Plagioclase	6.2	0.009 ± 0.001	140 ± 1	0.00019 ± 1	2	0.699081 ± 3
65315	Bulk rock	19.5	0.030 ± 0.002	123 ± 1	0.00071 ± 4	4	0.699141 ± 3
65325	Plagioclase	9.4	0.010 ± 0.001	184 ± 2	0.00019 ± 2	2	0.699071 ± 5
65325	Bulk rock	24.8	0.015 ± 0.001	166 ± 2	0.00034 ± 2	3	0.699089 ± 5
67075	Plagioclase	13.5	0.067 ± 0.003	125 ± 1	0.00155 ± 8	4	0.699161 ± 2

<sup>a</sup>Plagioclase: '-p', bulk: '-b', residue: '-r', and fines: '-f'.

<sup>b</sup>Uncertainties on  $^{87}\text{Rb}/^{86}\text{Sr}$  and  $^{87}\text{Sr}/^{86}\text{Sr}$  refer to last significant digits and for  $^{87}\text{Sr}/^{86}\text{Sr}$  are given as 2 s.e. for  $n \geq 4$  or as the 2 s.d. of the SRM 987 measurements within the same session for  $n < 4$ .  $^{87}\text{Sr}/^{86}\text{Sr}$  are normalized to  $^{87}\text{Sr}/^{86}\text{Sr} = 0.710245$  for SRM 987.

The reliable determination of the initial  $^{87}\text{Sr}/^{86}\text{Sr}$  ratios of FANs requires analyses of samples with sufficiently low  $^{87}\text{Rb}/^{86}\text{Sr}$  ratios such that the correction of measured  $^{87}\text{Sr}/^{86}\text{Sr}$  for radiogenic ingrowth becomes independent of the assumed age of a sample. Considering an age difference of between 3.8 Ga [i.e., the time of the late heavy bombardment of the Moon (Tera et al., 1974; Wetherill, 1975)] and 4.36 Ga [i.e., the crystallization age of FAN 60025 (Borg et al., 2011)] yields a ~ 10 ppm difference in calculated initial  $^{87}\text{Sr}/^{86}\text{Sr}$  ratios for an  $^{87}\text{Rb}/^{86}\text{Sr}$  ratio of 0.001. Thus, given an external reproducibility of  $\pm 5$  ppm of the  $^{87}\text{Sr}/^{86}\text{Sr}$  measurements (see section 4.4.2), the initial  $^{87}\text{Sr}/^{86}\text{Sr}$  of a sample can be determined reliably (i.e., independent of the assumed age of a sample) for samples having  $^{87}\text{Rb}/^{86}\text{Sr} \leq 0.001$ . This condition is met by all but one (sample 67075) of the plagioclase fractions analyzed in this study (Table 4, Fig. 17).

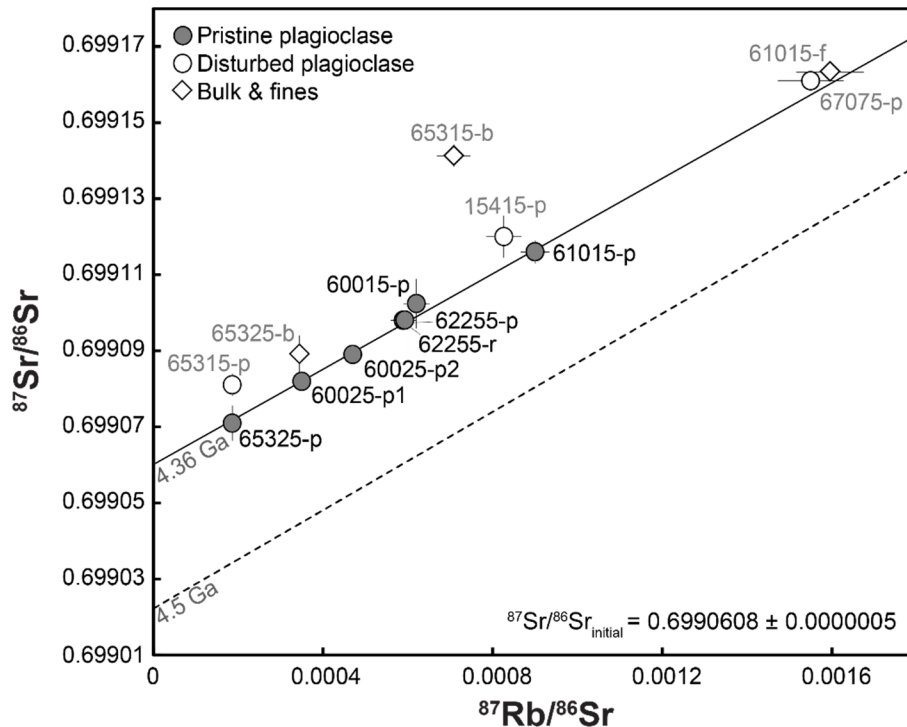


**Figure 17:** Rb-Sr isochron diagram for FANs. Reference isochrons were calculated using a bulk lunar  $^{87}\text{Rb}/^{86}\text{Sr} = 0.018$ , and relative to an age of 4.36 Ga for FAN 60025.

By contrast, the bulk and fines fractions of samples 65315, 65325, and 61015 display higher  $^{87}\text{Rb}/^{86}\text{Sr}$  and  $^{87}\text{Sr}/^{86}\text{Sr}$  ratios than their respective plagioclase fractions (Table 4, Fig. 17), suggesting that the Rb in these samples is predominantly located at grain boundaries between the plagioclase grains and in small melt patches. This highlights the importance of analyzing pure plagioclase fractions for reliably determining the initial  $^{87}\text{Sr}/^{86}\text{Sr}$  ratios of the samples. The plagioclase fractions of five FANs (65325, 60025, 62255, 60015, and 61015) plot along a single reference line in the Rb-Sr isochron diagram, indicating these samples formed about contemporaneously with a common initial  $^{87}\text{Sr}/^{86}\text{Sr}$  of  $0.6990608 \pm 0.0000005$  (2 s.e.,  $n = 7$ ; Fig. 17).

Owing to their low  $^{87}\text{Rb}/^{86}\text{Sr}$ , these samples do not provide a precise isochron age themselves ( $t = 4.497 \pm 0.469$  Ga, MSWD = 0.39), but among these FANs is sample 60025, for which precise absolute age of  $4.360 \pm 0.003$  Ga has been determined (Borg et al., 2011). Importantly, the  $^{87}\text{Rb}/^{86}\text{Sr}$  and  $^{87}\text{Sr}/^{86}\text{Sr}$  ratios obtained for plagioclase fractions from 60025 in this study are in good agreement with, albeit more precise than, previously reported values for this sample (Carlson and Lugmair, 1988; Borg et al., 2011) (Fig. A4.2). Thus, the new Sr isotope data for five FANs define the  $^{87}\text{Sr}/^{86}\text{Sr} = 0.6990608 \pm 0.000005$  of the Moon at  $4.360 \pm 0.003$  Ga (i.e., the age of FAN 60025). Three other FANs investigated in this study (65315, 15415, and 67075) plot slightly above the reference isochron defined by the other samples and are, therefore, characterized by higher initial  $^{87}\text{Sr}/^{86}\text{Sr}$  ratios (Fig. 17). As such, these samples either formed later than the other five FANs or their Rb-Sr systematics have been disturbed by post-crystallization processes such as for instance impact metamorphism.

### 4.3. Discussion

A Rb-Sr model age for the Moon can be calculated because the formation of the Earth-Moon system involved strong fractionation of Rb from Sr, as is manifested in the depletion of both bodies in the moderately volatile element Rb compared to refractory Sr (Wolf and Anders, 1980; Mezger et al., 2021). The  $^{87}\text{Rb}/^{86}\text{Sr}$  ratios of both the Earth and Moon are reasonably well constrained (see section 4.4.5), and so a Rb-Sr age can be determined by calculating the time at which the Earth-Moon system reached its initial Sr isotopic composition. This approach requires knowledge of both the precursor  $^{87}\text{Rb}/^{86}\text{Sr}$  and initial  $^{87}\text{Sr}/^{86}\text{Sr}$  of the Earth and Moon. However, while the  $^{87}\text{Rb}/^{86}\text{Sr}$  of the Earth is known, its initial  $^{87}\text{Sr}/^{86}\text{Sr}$  is not known a priori. Conversely, while the initial  $^{87}\text{Sr}/^{86}\text{Sr}$  of the Moon is precisely constrained by the data of this study, the  $^{87}\text{Rb}/^{86}\text{Sr}$  of the precursor material that formed the Moon is not known. This is because the Moon is strongly depleted in Rb, and this depletion partly or wholly results from Rb loss immediately following the giant impact that formed the Moon (Lock et al., 2018; Charnoz et al., 2021). Thus, prior studies have calculated a Rb-Sr age for the Moon by assuming that the Earth and Moon equilibrated isotopically, and as such the initial isotopic composition of the Moon equals that of the Earth (Halliday, 2008; Mezger et al., 2021). However, others have argued that the Rb-Sr system cannot be used in this manner because the initial Sr isotopic compositions of the Earth and the Moon may have been different (Borg et al., 2022).

To more rigorously assess under which conditions the Rb-Sr system can be used to date the Moon, we calculated the Rb-Sr isotopic evolution of the proto-Earth and the Moon-forming impactor Theia in current formation models for the Moon. We distinguish between four different impact scenarios: (i) models that invoke Earth-Moon isotopic equilibration; and models, that do not require isotopic equilibration, such as (ii) the canonical impact model, (iii) models in which the Earth and the Moon consist of similar mixtures of proto-Earth and Theia, or (iv) the Moon is formed mainly from proto-Earth's mantle (for a review of possible impact configurations see Canup et al., 2023).

The first of these cases is similar to the approach utilized in some prior studies, and an age of the Moon can be determined by calculating the time at which a reservoir

characterized by the BSE's  $^{87}\text{Rb}/^{86}\text{Sr}$  ratio has evolved to the lunar  $^{87}\text{Sr}/^{86}\text{Sr}$  (see section 4.4.3). Using this approach, we calculate an age of  $4.502 \pm 0.021$  Ga, or  $65 \pm 21$  million years (Ma) after solar system formation (Fig. 18; 4.4.3, and Table 5 for summary of parameters used in the age calculation). This age is broadly consistent with Rb-Sr ages of  $87 \pm 13$  Ma (Halliday, 2008) and  $60 \pm 15$  Ma reported in prior studies (Mezger et al., 2021), but this consistency is partly coincidence, for two main reasons. First, unlike these previous studies, our approach considers the Sr isotopic evolution within the Moon prior to crystallization of FANs, which results in Moon formation ages that are  $\sim 30$  Ma older than the ages calculated without correcting the FAN's initial  $^{87}\text{Sr}/^{86}\text{Sr}$  for radiogenic ingrowth within the Moon. This, together with the new and more precise  $^{87}\text{Sr}/^{86}\text{Sr}$  determined in this study, accounts for the difference of our Rb-Sr age compared to the  $87 \pm 13$  Ma estimate from an earlier study.

Second, the choice of the initial  $^{87}\text{Sr}/^{86}\text{Sr}$  ratio of the solar system has a similarly large effect on the calculated age (see Fig. A4.5–4.7). Using the initial  $^{87}\text{Sr}/^{86}\text{Sr}$  derived from angrite meteorites (Hans et al., 2013) results in Rb-Sr model ages that are  $\sim 30$ – $40$  Ma older compared to ages calculated relative to the initial  $^{87}\text{Sr}/^{86}\text{Sr}$  determined based on CAIs (see section 4.4.5.). As such, the good agreement of our Rb-Sr age compared to the  $60 \pm 15$  Ma age from Mezger et al. (2021) reflects that this former age should be  $\sim 30$  Ma younger because the Sr isotope evolution within the Moon was not considered, but should also be  $\sim 25$  Ma older because a different, higher solar system initial  $^{87}\text{Sr}/^{86}\text{Sr}$  was used. Finally, the uncertainty of the Rb-Sr age of this study is somewhat larger than uncertainties reported in the earlier studies, because we fully account for uncertainties associated with the initial  $^{87}\text{Sr}/^{86}\text{Sr}$  of the solar system and the Sr isotope evolution within the Moon (see section 4.4.5).

The validity of the Rb-Sr age calculated above relies on the assumption of efficient Sr isotope equilibration between the Earth and Moon during or immediately following the giant impact. It has been suggested that Earth-Moon equilibration is needed to account for the unexpected isotopic similarity of both bodies for elements that otherwise exhibit large isotopic variations among meteorites and planets (Pahlevan and Stevenson, 2007; Melosh, 2014; Lock et al., 2018). However, since proto-Earth and Theia may have evolved with very different  $^{87}\text{Rb}/^{86}\text{Sr}$  ratios, the difference in their  $^{87}\text{Sr}/^{86}\text{Sr}$  ratios is potentially much larger than any pre-existing isotope difference between these two bodies for other elements, and

so any pre-existing  $^{87}\text{Sr}/^{86}\text{Sr}$  difference may not have been erased completely. Of note, to account for the isotopic similarity of the Earth and Moon, other models have been developed in which the Moon predominantly consists of proto-Earth material, such as in the fast-spinning Earth model (Ćuk and Stewart, 2012) or Earth collided with a roughly similar sized planet and the Earth and the Moon are made from roughly similar mixtures, such as the half Earths collision model (Canup, 2012). As such, it is important to evaluate as to whether the Rb-Sr systematics can also be used to date the formation of the Moon without the assumption of Earth-Moon equilibration.

Without this assumption, a Rb-Sr age cannot be calculated as outlined above (see section 4.4.3), because we cannot assume *a priori* that the Earth and Moon had the same  $^{87}\text{Sr}/^{86}\text{Sr}$  immediately following the giant impact. To assess if a Rb-Sr age can nevertheless be calculated, we calculate the  $^{87}\text{Rb}/^{86}\text{Sr}$  of the Earth and the  $^{87}\text{Sr}/^{86}\text{Sr}$  of the Moon (i.e., the two parameters that are well constrained) resulting from the particular mixture of proto-Earth and impactor (i.e., Theia) materials predicted in different Moon formation scenarios (see section 4.4.4). In these models, the  $^{87}\text{Rb}/^{86}\text{Sr}$  ratios of proto-Earth and Theia are not known and are, therefore, assumed to be within the range of compositions observed among meteorite parent bodies (see section 4.4.4). Their corresponding  $^{87}\text{Sr}/^{86}\text{Sr}$  ratios at the time of Moon formation are determined by calculating the radiogenic ingrowth since the time of solar system formation until the time of the Moon-forming impact, and using the respective  $^{87}\text{Rb}/^{86}\text{Sr}$  of each body. In reality, neither proto-Earth nor Theia are expected to have evolved with a single  $^{87}\text{Rb}/^{86}\text{Sr}$  until the giant impact, but since we consider the full range of plausible  $^{87}\text{Rb}/^{86}\text{Sr}$  ratios for both objects, nearly every possible Rb-Sr isotopic evolution of these bodies is covered in these calculations ( $\geq 5 \times 10^5$  models for each scenario). The resulting  $^{87}\text{Rb}/^{86}\text{Sr}$  of the bulk silicate Earth (BSE) and  $^{87}\text{Sr}/^{86}\text{Sr}$  of the Moon can then be calculated by mass balance (see section 4.4.4). We ran Rb-Sr evolution calculations for different Moon formation scenarios, where the input parameters (Rb/Sr ratios of Theia and proto-Earth, size of the Theia, and mass fraction of Theia in the Moon) are varied randomly according to the respective impact scenario, and the time of the giant impact is a free parameter (see section 4.4.4; Table 6, 7). Models are considered successful when  $^{87}\text{Rb}/^{86}\text{Sr}_{\text{BSE}} = 0.08 \pm 0.01$  and  $^{87}\text{Sr}/^{86}\text{Sr}_{\text{Moon}}$  at time  $t = 4.360 \pm 0.003$  Ga matches the

observed  $^{87}\text{Sr}/^{86}\text{Sr}_{\text{FAN}} = 0.6990608 \pm 0.0000005$ . Thus, unlike for the case of Earth-Moon equilibration, the initial  $^{87}\text{Sr}/^{86}\text{Sr}$  of the Earth can be different from that of the Moon.

Our model age results are presented in Figure 18 for four different impact models and show that only for the canonical impact scenario no Rb-Sr age is obtained. This is consistent with results from an earlier study (Borg et al., 2022) and stems from the fact that in the canonical model the Moon predominantly consists of impactor material (Canup and Asphaug, 2001) and that, therefore, the initial Sr isotope compositions of Earth and Moon are in most cases different.

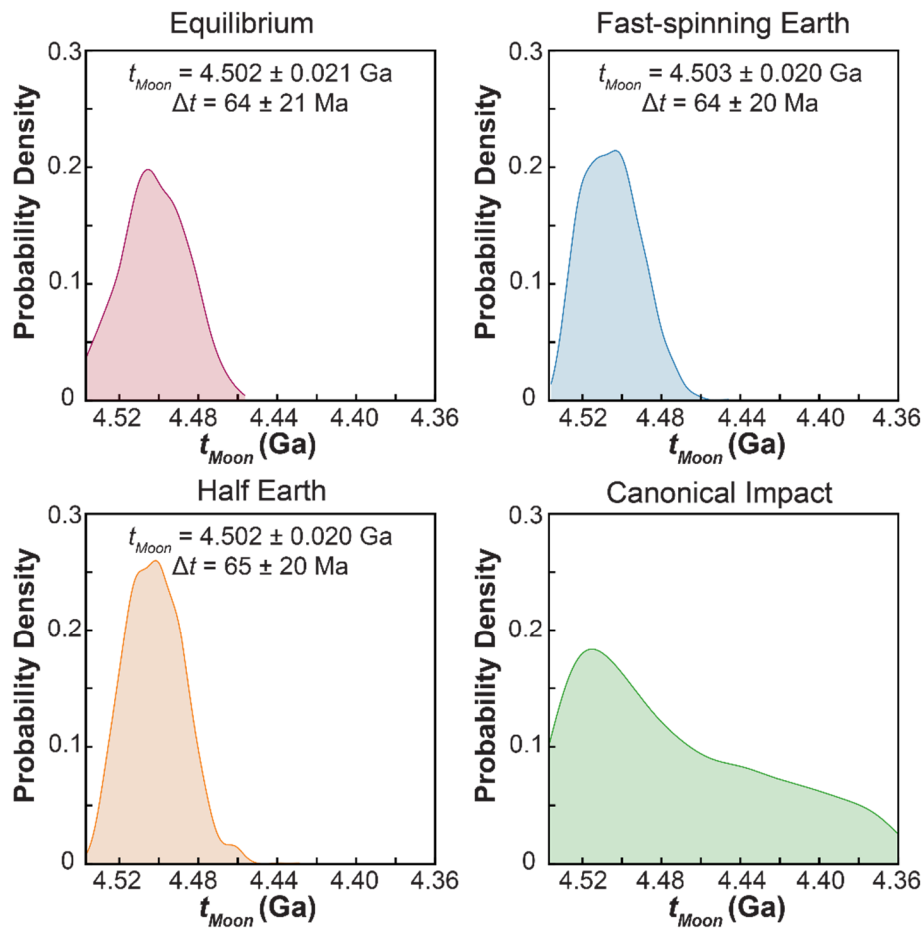


**Figure 18:** Rb-Sr model ages for the time of Moon formation calculated for four different impact scenarios. No discrete peak is obtained for the canonical impact scenario, but all other scenarios provide a consistent Moon formation age of  $4.502 \pm 0.020$  Ga, or  $65 \pm 20$  Ma after solar system formation.

By contrast, in both the fast-spinning Earth (Ćuk and Stewart, 2012) and the half Earth models (Canup, 2012), the  $^{87}\text{Rb}/^{86}\text{Sr}$  of the BSE and the initial  $^{87}\text{Sr}/^{86}\text{Sr}$  of the Moon are reproduced only for a relatively narrow range of impact ages of  $4.503 \pm 0.020$  Ga (or  $64 \pm 20$  Ma after solar system formation) and  $4.502 \pm 0.020$  Ga (or  $65 \pm 20$  Ma after solar system formation), respectively. This is because in the fast-spinning Earth scenario, the Moon predominantly consists of proto-Earth material (Ćuk and Stewart, 2012). Therefore, the initial Sr isotopic composition of the Moon provides a good proxy for that of the proto-Earth at the time of the impact, which, because Theia is quite small in this scenario, in turn is approximately the initial  $^{87}\text{Sr}/^{86}\text{Sr}$  of Earth. Conversely, in the half Earth impact model (Canup, 2012), the Moon and the Earth are produced from approximately the same mixtures of Theia and proto-Earth material, such that again the initial Sr isotopic composition of the Moon is essentially that of the Earth. Consequently, although these two giant impact models do not assume isotopic equilibration between the Earth and the Moon, they nevertheless predict very similar initial Sr isotopic compositions for the Earth and the Moon.

As such, like in the equilibration case, the Rb-Sr systematics can be used to calculate an age for the Moon, which, given the similar initial Sr isotopic compositions of the Earth and the Moon in all cases, are all similar and indicate that the Moon formed at  $4.502 \pm 0.020$  Ga, or  $65 \pm 20$  Ma after solar system formation.

Our calculations show that only the canonical impact model does *not* allow to determine a Rb-Sr age for the formation of the Moon. This impact scenario requires proto-Earth and Theia to have the same nucleosynthetic isotope compositions, implying that both formed from the same precursor materials. However, dynamical models of planet formation predict that Earth accreted material from different areas of the accretion disk, and so, given the range of isotopic compositions observed among meteorites and planets (Burkhardt et al., 2021), it appears unlikely that proto-Earth and Theia had the same isotopic compositions (Canup et al., 2023). Moreover, the canonical impact model has great difficulty explaining the similar  $^{182}\text{W}$  isotope compositions of the BSE and the Moon (Kruijer et al., 2015; Touboul et al., 2015; Kruijer and Kleine, 2017).

Different  $^{182}\text{W}$  signatures in the mantle of planetary objects reflect decay of short-lived  $^{182}\text{Hf}$  (half-life  $\sim 8.9$  Ma) following an early Hf-W fractionation during core formation (Kleine and Walker, 2017). Thus, unlike nucleosynthetic isotope signatures,  $^{182}\text{W}$  variations do not reflect the formation location of material in the disk, but record the accretion and core formation history of an object. As such, regardless of whether proto-Earth and Theia formed in the same region of the accretion disk, the  $^{182}\text{W}$  compositions of their mantles are not expected to be the same. Moreover, during the giant impact materials from proto-Earth's mantle, Theia's mantle, and Theia's core were mixed in various proportions to produce the final Earth and the Moon. All of these reservoirs presumably had different  $^{182}\text{W}$  compositions, and it is therefore highly unlikely to produce the similar  $^{182}\text{W}$  compositions of Earth's mantle and the Moon by this process (Kruijer and Kleine, 2017; Fischer et al., 2021). These difficulties also apply to the fast-spinning proto-Earth and half Earth impact models, but to a lesser extent, given the, respectively, small impactor size and more rigorous mixing in these models (Kruijer and Kleine, 2017). Thus, the canonical model does not provide a realistic scenario to account for the isotopic similarity of the Earth and Moon and, as such, also not for the Rb-Sr isotope evolution of the Earth-Moon system. Given that all other giant impact models define a precise Rb-Sr age for the Moon, we, therefore, conclude that the Rb-Sr systematics can be used to date the Moon, implying that the Moon formed at  $4.502 \pm 0.020$  Ga, or  $65 \pm 20$  Ma after solar system formation.

The age of the Moon determined in this study is  $\sim 150$  Ma older than the solidification age of the lunar magma ocean that has been inferred by dating the formation of FANs, the mare basalt sources, and KREEP (Borg et al., 2011, 2019; Gaffney and Borg, 2014). This age difference indicates either that the LMO was long-lived or that the whole-rock ages used to date solidification of the LMO have been partially or wholly reset by some later event(s). Current thermal models suggest that the LMO took  $\sim 100$  Ma to completely solidify (Maurice et al., 2020). Within this framework, and given that the crystallization of FANs is thought to have started soon after the formation of the Moon, we may expect to see variable formation ages of FANs, covering the entire solidification period of the LMO (Michaut and Neufeld, 2022). However, the new Sr isotopic data show that does not seem to be the case.

Although the Rb-Sr data of this study provide no precise absolute ages for the FANs, their indistinguishable initial  $^{87}\text{Sr}/^{86}\text{Sr}$  ratios can nevertheless be used to assess a maximum age difference among them. The initial  $^{87}\text{Sr}/^{86}\text{Sr}$  ratios of the five FANs with the least radiogenic Sr isotope composition vary by only  $\pm 4.8$  ppm [mean  $^{87}\text{Sr}/^{86}\text{Sr} = 0.699061 \pm 0.000003$  ( $\pm 2$  s.d.,  $n = 5$ ), Table A4.2], which in a reservoir characterized by the bulk lunar  $^{87}\text{Rb}/^{86}\text{Sr}$  of 0.018 corresponds to a time difference of  $\sim 14$  Ma. Consequently, provided the FANs crystallized from a melt with the bulk lunar  $^{87}\text{Rb}/^{86}\text{Sr}$ , their common initial  $^{87}\text{Sr}/^{86}\text{Sr}$  indicates they formed within at most  $\sim 28$  Ma of each other, which is much shorter than the expected lifetime of the LMO.

This discrepancy could reflect that the samples investigated in this study are not representative of the entire suite of FANs formed on the Moon. This possibility is difficult to exclude, given that all the samples having a common initial  $^{87}\text{Sr}/^{86}\text{Sr}$  are from the Apollo 16 landing site. Another possibility is that the common  $\sim 4.36$  Ga age of FANs reflects continuous recycling of earlier-formed crust by remelting from the underlying magma ocean, such that only the latest-formed crust was preserved. However, at least some recent models for lunar crust formation predict that in long-lived LMO, FANs should have formed over an extended period of time, and not a short interval as observed here (Michaut and Neufeld, 2022). Finally, a third possibility, already pointed out by Borg et al. (2011), is that FANs did not form in the original LMO, but record re-melting and crystallization during some later event. However, the nature of such a re-melting event is unclear at present, in particular because it would have to have affected a very large volume of the Moon (Borg et al., 2019). This is because the 4.36 Ga age is not only found for FANs but also for all other products of the LMO, indicating this time marks a major magmatic event affecting most of the Moon.

We conclude that while the age offset between the formation of the Moon and crystallization of FANs remains unclear, this uncertainty highlights the difficulty in linking the age of LMO products such as FANs to the age of the Moon. By contrast, the Rb-Sr model age presented here provides a more robust determination of the formation of the Moon, because it dates Rb-Sr fractionation associated with Rb loss from the Moon, which occurred immediately following the giant impact. We emphasize that this age is independent of whether or not FANs formed over an extended period of time, because the data of this study

precisely determine the  $^{87}\text{Sr}/^{86}\text{Sr}$  of the Moon at a well-defined point in time. Thus, if there are older FANs they will have lower  $^{87}\text{Sr}/^{86}\text{Sr}$ , which would be inconsequential for the age calculation because our approach accounts for the Rb-Sr isotopic evolution in the Moon (see above). As such the Rb-Sr model age provides a robust estimate for the formation time of the Moon which is independent of uncertainties associated with the lifetime of the LMO and the extent to which post-LMO resetting of individual ages occurred.

Our model age for Moon formation of  $65 \pm 20$  Ma after solar system formation is consistent with a number of other constraints. First, the  $^{182}\text{Hf}$ - $^{182}\text{W}$  systematics of the Moon have been interpreted to indicate formation of the Moon at  $\sim 50$  Ma after solar system formation (Thiemens et al., 2019). This age, however, only reflects a lower bound on the age of the Moon, because the  $^{182}\text{W}$  difference between the Moon and the Earth's mantle is at least in part due to late accretion to the Earth and Moon following the Moon-forming impact (Kruijjer et al., 2015; Touboul et al., 2015), such that the  $^{182}\text{Hf}$ - $^{182}\text{W}$  systematics are consistent with later Moon formation times (Kruijjer and Kleine, 2017; Kruijjer et al., 2021). Second, the occurrence of ancient zircons with crystallization ages of  $4.417 \pm 0.006$  Ga (Nemchin et al., 2009) and  $4.460 \pm 0.031$  Ga (Greer et al., 2023) indicate that the Moon formed and was nearly or completely solidified by  $\sim 150$  Ma after solar system formation. Given that LMO solidification may have taken up to  $\sim 100$  Ma, this is consistent with formation of the Moon at  $\sim 65$  Ma after solar system formation. Finally, constraints from the  $^{176}\text{Lu}$ - $^{176}\text{Hf}$  system in lunar zircons have been interpreted to indicate Moon formation within the first  $\sim 60$  Ma of the solar system (Barboni et al., 2017), which again is consistent with the Rb-Sr model age.

Furthermore, formation of the Moon at  $65 \pm 20$  Ma after solar system formation is consistent with predictions of recent dynamical models of terrestrial planet formation. While the timing of the last giant impact in these models varies [e.g., from 20 to 180 Ma (Woo et al., 2024)], there is an inverse correlation between the time of the last giant impact and the mass of late-accreted material added to the Earth afterwards [i.e., the late veneer (Walker, 2009)]. This correlation results naturally because the later the last impact occurs, the less material is left in the terrestrial planet region to be accreted as the late veneer. Since the mass of the late veneer on Earth is known from the abundances of highly siderophile elements in Earth's mantle (Walker, 2009), the correlation of giant impact time with the late-accreted mass can

be used to infer the predicted time of the Moon-forming impact for a given set of planet formation simulations. This approach was first used by Jacobson et al. (2014), who inferred an age of the Moon  $95 \pm 32$  Ma after solar system formation, based on a series of Grand Tack simulations. However, using the same approach, more recent planet formation models, in which terrestrial planet formation started from a ring of planetesimals formed at  $\sim 1$  AU, infer a Moon formation time of  $\sim 30$ – $80$  Ma after solar system formation (Woo et al., 2024). Both of these estimates are consistent with our Rb-Sr model age of the Moon and in agreement with the predictions of the ring model. We therefore conclude that a formation of the Moon  $65 \pm 20$  million years after solar system formation, as derived from Rb-Sr isotope systematics, is consistent with the oldest lunar zircon ages, newer LMO solidification models, implications from Hf-W systematics, and constraints from the late-accreted mass on Earth and the dynamics of terrestrial planet formation.

## 4.4. Materials and Methods

### 4.4.1 Sample preparation and chemical separation

Between 50 and 200 mg of each FAN sample was crushed carefully in an agate mortar and pure plagioclase grains were handpicked under a binocular. Where necessary, samples were sieved to  $> 125 \mu\text{m}$  to obtain intact grains. Relatively pure anorthites were identified as translucent grains with plain surfaces and no visible dark patches or inclusions (Fig. A4.1). In total, 14 different fractions from eight ferroan anorthosite samples were measured. Of these, nine samples are plagioclase separates ('-p'), three bulk samples ('-b'), one residue after hand picking ('-r'), and one sieved fines fraction ('-f';  $> 125 \mu\text{m}$ ). After weighing, the samples were cleaned with Milli-Q water in an ultrasonic bath to remove any potential surface contamination with Rb. The use of any acid for sample washing was avoided, to not risk fractionation of sample Rb and Sr through leaching. Analyses of the wash fractions show tens to hundreds of picograms Rb in some fractions, highlighting the importance of removing Rb contamination from the grain surfaces before further processing of the samples. Comparison of results of washed and unwashed fractions of sample 60025, together with comparison to literature data for this sample, demonstrates that this procedure efficiently removes any Rb contamination. After washing, the samples were digested in pre-cleaned

Teflon beakers using a 2:1 mixture of double distilled HF-HNO<sub>3</sub> at 140 °C for 2–3 days, followed by dissolution in *aqua regia* at 140 °C for 2 days. The samples were then dried in 0.5 ml 6 M HCl, and were re-dissolved in 2 ml 2.5 M HCl. At this stage, depending on the amount of sample available, some of the samples were split into two aliquots. One aliquot was spiked with a <sup>85</sup>Rb-<sup>84</sup>Sr tracer for the determination of Rb and Sr concentrations by isotope dilution (ID-aliquot). The other aliquot (IC-aliquot) was used solely for measuring Sr isotopic compositions. For samples for which less material was available, no aliquot was taken, and the entire sample was mixed with an appropriate amount of the <sup>85</sup>Rb-<sup>84</sup>Sr spike. For all samples, <sup>87</sup>Sr/<sup>86</sup>Sr ratios were measured on the ID aliquot and the final <sup>87</sup>Sr/<sup>86</sup>Sr was obtained by subtracting the contribution from the spike (Stracke et al., 2014). For samples for which both ID and IC aliquots were measured, the <sup>87</sup>Sr/<sup>86</sup>Sr ratios determined for both aliquots agree with each other, attesting to the accuracy of the spike subtraction (Fig. A4.3).

After aliquoting and spiking, samples were loaded onto quartz glass columns filled with 5 ml cation exchange resin (BioRad AG-50W-X2, 200–400 mesh), and Rb and Sr were eluted using 2.5 M HCl (e.g., Nebel et al., 2005). The Rb and Sr cuts were dried, re-dissolved in concentrated HNO<sub>3</sub>, and diluted to 0.25 ml 5 M HNO<sub>3</sub>. These solutions were loaded onto homemade microcolumns filled with 100 µl Eichrom Sr-spec-B resin, and Rb was eluted using 1.2 ml 5 M HNO<sub>3</sub>, followed by Sr, which was eluted with 1.7 ml Milli-Q water (e.g., Nebel et al., 2005). This procedure resulted in sufficiently clean Rb-ID, Sr-ID, and Sr-IC cuts for the isotope measurements (i.e., interference corrections were negligible).

Given the low Rb but high Sr contents of the samples, any blank contribution is expected to be insignificant for Sr, but can be very important for Rb. Thus, Rb blanks were carefully monitored throughout this study, and for each sample a Rb blank was processed through the entire digestion and chemical separation procedure. Total procedural Rb blanks were between 3 and 16 pg (n = 12, 9/12 < 10 pg), resulting in < 5% Rb blank contribution for all measured samples except 65315-Plag (29%) and 65325-Plag (7%). For all samples, the uncertainties introduced by the blank correction were propagated into the final uncertainty of the measured <sup>87</sup>Rb/<sup>86</sup>Sr ratios. Total procedural blanks for Sr were between 5 and 16 pg (n = 2) and were negligible.

#### 4.4.2 Rb-Sr isotope measurements

The Rb-ID measurements were performed using Thermo Fisher Triton XT thermal ionization mass spectrometer (TIMS) at the Max Planck Institute for Solar System Research (MPS). For the measurement, 0.5 ng Rb was loaded onto previously outgassed Re filaments together with a Ta<sub>2</sub>O<sub>5</sub> activator and measured at 600–700 °C for 40 cycles in static mode. Possible interference from <sup>87</sup>Sr on <sup>87</sup>Rb were monitored by also measuring the ion beam on <sup>88</sup>Sr, but owing to the much higher ionization temperature of Sr compared to Rb, no <sup>88</sup>Sr signal above baseline was observed. Instrumental mass fractionation was corrected using measurement of the NIST 984 Rb standard alongside the samples. Based on the standard measurements, the uncertainty on measured <sup>87</sup>Rb/<sup>85</sup>Rb ratios is 0.5% (2 s.d.). The largest contributor to the final uncertainty of <sup>87</sup>Rb/<sup>86</sup>Sr ratios is the Rb blank correction, resulting in final uncertainty on measured <sup>87</sup>Rb/<sup>86</sup>Sr ratios of 5% (2 s.d.). Given the low <sup>87</sup>Rb/<sup>86</sup>Sr of all samples of this study, this uncertainty is inconsequential for the interpretation of the Rb-Sr isotopic data.

The Sr isotopic composition of the IC-Sr and ID-Sr aliquots were also performed on the Triton XT at MPS, where Sr was measured in a three-line multi-dynamic data acquisition scheme using our previously established procedures (Hans et al., 2013; Chapter 2). Each measurement consisted of 400–600 cycles of data acquisition and the final <sup>87</sup>Sr/<sup>86</sup>Sr is obtained from the <sup>87</sup>Sr/<sup>86</sup>Sr measured in each line corrected for mass fractionation using the <sup>88</sup>Sr/<sup>86</sup>Sr measured in two lines. The mass fractionation uses the exponential law and <sup>86</sup>Sr/<sup>88</sup>Sr = 0.1194. The NIST SRM987 Sr standard yielded <sup>87</sup>Sr/<sup>86</sup>Sr = 0.710245 ± 0.000005 (2 s.d., n = 43) for the course of this study. Where possible, samples were measured multiple times and the uncertainty on <sup>87</sup>Sr/<sup>86</sup>Sr are reported as twice the standard error for n ≥ 4 or twice the standard deviation of the standard measurements of the same session (for n < 4).

#### 4.4.3 Rb-Sr age in case of Earth-Moon equilibration

The Sr isotopic composition of the BSE at time  $t$  is given by:

*Equation 11*

$$\left(\frac{{}^{87}\text{Sr}}{{}^{86}\text{Sr}}\right)_{BSE,t} = \left(\frac{{}^{87}\text{Sr}}{{}^{86}\text{Sr}}\right)_{SSI} + \left(\frac{{}^{87}\text{Rb}}{{}^{86}\text{Sr}}\right)_{BSE} \times (e^{\lambda(t_{CAI}-t_{Moon})} - 1),$$

where SSI stands for ‘solar system initial’ and  $t_{CAI}$  and  $t_{Moon}$  are the absolute ages of Ca-Al-rich inclusions (CAI) and the Moon, respectively (Table 5). The initial Sr isotopic composition of the Moon can be back-calculated from the measured Sr isotopic composition of FANs of known age ( $t_{FAN}$ ):

Equation 12

$$\left(\frac{^{87}\text{Sr}}{^{86}\text{Sr}}\right)_{Moon,i} = \left(\frac{^{87}\text{Sr}}{^{86}\text{Sr}}\right)_{FAN,t} - \left(\frac{^{87}\text{Rb}}{^{86}\text{Sr}}\right)_{Moon} \times (e^{\lambda(t_{Moon}-t_{FAN})} - 1).$$

With the assumption that at the time of Moon formation the initial Sr isotopic compositions of the BSE and the Moon were identical, we have:

Equation 13

$$\begin{aligned} \left(\frac{^{87}\text{Sr}}{^{86}\text{Sr}}\right)_{SSI} + \left(\frac{^{87}\text{Rb}}{^{86}\text{Sr}}\right)_{BSE} \times (e^{\lambda(t_{CAI}-t_{Moon})} - 1) \\ = \left(\frac{^{87}\text{Sr}}{^{86}\text{Sr}}\right)_{FAN,t} - \left(\frac{^{87}\text{Rb}}{^{86}\text{Sr}}\right)_{Moon} \times (e^{\lambda(t_{Moon}-t_{FAN})} - 1). \end{aligned}$$

The only unknown in this equation is the age of the Moon,  $t_{Moon}$ . Because the time differences  $t_{Moon} - t_{FAN}$  and  $t_{CAI} - t_{Moon}$  are much smaller than the half-life of  $^{87}\text{Rb}$  ( $\sim 49$  Ga), we can use the Taylor series approximation  $e^{\lambda t} = 1 + \lambda t + \dots$ . With this approximation we can solve for the age of the Moon:

Equation 14

$$t_{Moon} \approx \frac{b\lambda t_{CAI} - d\lambda t_{FAN} + a - c}{(b - d)\lambda},$$

where the parameters are defined as follows:

Equation 15

$$a = \left(\frac{^{87}\text{Sr}}{^{86}\text{Sr}}\right)_{SSI}, b = \left(\frac{^{87}\text{Rb}}{^{86}\text{Sr}}\right)_{BSE}, c = \left(\frac{^{87}\text{Sr}}{^{86}\text{Sr}}\right)_{FAN,t}, d = \left(\frac{^{87}\text{Rb}}{^{86}\text{Sr}}\right)_{Moon}.$$

#### 4.4.4 Rb-Sr age in non-equilibrium models

In the case where there was no isotopic equilibration between the Earth and Moon, the  $^{87}\text{Rb}/^{86}\text{Sr}$  and  $^{87}\text{Sr}/^{86}\text{Sr}$  of both bodies can be calculated by mass balance using assumed compositions of proto-Earth and Theia, the relative size of Theia ( $x_{Theia}$ ), and the mass

fraction of material from Theia in the Moon ( $f_{Theia}$ ). Specifically, the present-day  $^{87}\text{Rb}/^{86}\text{Sr}_{\text{BSE}}$  can be calculated as follows:

Equation 16

$$\left(\frac{^{87}\text{Rb}}{^{86}\text{Sr}}\right)_{\text{BSE}} = \left[ 2.89 \times \left( \frac{x_{\text{Theia}} \times \text{Rb}_{\text{Theia}} + (1 - x_{\text{Theia}}) \times \text{Rb}_{\text{proto-Earth}}}{x_{\text{Theia}} \times \text{Sr}_{\text{Theia}} + (1 - x_{\text{Theia}}) \times \text{Sr}_{\text{proto-Earth}}} \right) \right] \times (e^{-\lambda \times t_{\text{Moon}}}),$$

where  $x_{\text{Theia}}$  and  $\text{Rb}_{\text{Theia}}$ ,  $\text{Sr}_{\text{Theia}}$ ,  $\text{Rb}_{\text{proto-Earth}}$ ,  $\text{Sr}_{\text{proto-Earth}}$  refer to the Rb and Sr concentrations of proto-Earth and Theia (see section 4.4.5, Table 7).

Similarly, the Moon's initial  $^{87}\text{Sr}/^{86}\text{Sr}$  can be calculated as follows:

Equation 17

$$\left(\frac{^{87}\text{Sr}}{^{86}\text{Sr}}\right)_{\text{Moon}, t} = \frac{f_{\text{Theia}} \times \left(\frac{^{87}\text{Sr}}{^{86}\text{Sr}}\right)_{\text{Theia}, t} \times \text{Sr}_{\text{Theia}} + (1 - f_{\text{Theia}}) \times \left(\frac{^{87}\text{Sr}}{^{86}\text{Sr}}\right)_{\text{proto-Earth}, t} \times \text{Sr}_{\text{proto-Earth}}}{f_{\text{Theia}} \times \text{Sr}_{\text{Theia}} + (1 - f_{\text{Theia}}) \times \text{Sr}_{\text{proto-Earth}}},$$

using the  $^{87}\text{Sr}/^{86}\text{Sr}_{\text{Theia}}$  and  $^{87}\text{Sr}/^{86}\text{Sr}_{\text{proto-Earth}}$  at time  $t$ , which are in turn calculated according to:

Equation 18

$$\left(\frac{^{87}\text{Sr}}{^{86}\text{Sr}}\right)_{\text{Theia or proto-Earth}, t} = \left(\frac{^{87}\text{Sr}}{^{86}\text{Sr}}\right)_{\text{SSI}} + \left(\frac{^{87}\text{Rb}}{^{86}\text{Sr}}\right)_{\text{Theia or proto-Earth}, t} \times (e^{\lambda(t_{\text{CAI}} - t_{\text{Moon}})} - 1).$$

To match the measured lunar initial  $^{87}\text{Sr}/^{86}\text{Sr} = 0.6990608 \pm 0.000005$  at  $t_{\text{FAN}} = 4.360 \pm 0.003$  Ga (Borg et al., 2011), the Moon's  $^{87}\text{Sr}/^{86}\text{Sr}$  then follows subsequent isotopic evolution with  $^{87}\text{Rb}/^{86}\text{Sr}_{\text{bulk-Moon}} = 0.018 \pm 0.006$  (Borg et al., 2022) according to:

Equation 19

$$\left(\frac{^{87}\text{Sr}}{^{86}\text{Sr}}\right)_{\text{Moon}, t_{\text{FAN}}} = \left(\frac{^{87}\text{Sr}}{^{86}\text{Sr}}\right)_{\text{Moon}, t_{\text{Moon}}} + \left(\frac{^{87}\text{Rb}}{^{86}\text{Sr}}\right)_{\text{Moon}} \times (e^{\lambda(t_{\text{Moon}} - t_{\text{FAN}})} - 1).$$

We calculated the  $^{87}\text{Sr}/^{86}\text{Sr}$  of the Moon at time  $t_{\text{FAN}}$  and the BSE's  $^{87}\text{Rb}/^{86}\text{Sr}$  for random combinations of  $x_{\text{Theia}}$ ,  $f_{\text{Theia}}$ ,  $\text{Rb}/\text{Sr}_{\text{Theia}}$ , and  $\text{Rb}/\text{Sr}_{\text{proto-Earth}}$  within their respective bounds (see below and Tables 6–7). The age of the moon ( $t_{\text{Moon}}$ ) is a free parameter varied between 4.537 Ga, which is the earliest time possible for Moon formation as defined by

Hf-W chronometry (Touboul et al., 2007, Nimmo and Kleine 2015), and 4.360 Ga, the crystallization age of FAN 60025, marking the youngest possible age of the Moon (Borg et al., 2011). Models are considered successful when the  $^{87}\text{Sr}/^{86}\text{Sr}_{\text{Moon}}$  at time  $t_{\text{FAN}} = 4.360 \pm 0.003$  Ga matches the measured  $^{87}\text{Sr}/^{86}\text{Sr} = 0.6990608 \pm 0.0000005$  and the BSE's  $^{87}\text{Rb}/^{86}\text{Sr}$  matches the observed  $^{87}\text{Rb}/^{86}\text{Sr}_{\text{BSE}} = 0.08 \pm 0.01$  (Borg et al., 2022). For models which display discrete peaks of  $t_{\text{Moon}}$  (i.e., all models except the canonical model), the Rb-Sr model age was obtained from the probability density function of  $t_{\text{Moon}}$  ( $n = 1000$ , Fig. 5, Fig. A4.5–4.7).

#### 4.4.5 Choice of parameters for model age calculations

The parameters with their respective uncertainties used in the model age calculations are summarized in Tables 5–7. For the  $^{87}\text{Rb}/^{86}\text{Sr}$  ratios of the BSE and the Moon we take the estimates from Borg et al. (2022), which is based on a compilation of estimates from several prior studies. For the age of CAIs we take 4.567 Ga (Connelly et al., 2012), and for the age of FANs  $4.360 \pm 0.003$  Ga (Borg et al., 2011). For the Rb and Sr concentrations, and  $^{87}\text{Rb}/^{86}\text{Sr}$  ratios of proto-Earth and Theia we assume the full range of possible compositions, from extremely volatile element-depleted objects having Rb/Sr  $\sim 0$  to volatile element-rich bodies having a CI chondrite-like  $^{87}\text{Rb}/^{86}\text{Sr}$  of  $\sim 0.8$ . Given that CI chondrites are the most volatile element-rich meteorites known, their  $^{87}\text{Rb}/^{86}\text{Sr}$  provides a reasonable estimate for the highest possible ratio of either proto-Earth or Theia. The size of Theia and the fraction of material from Theia in the Moon for the different giant impact models are taken from the compilation in Canup et al. (2023).

The initial  $^{87}\text{Sr}/^{86}\text{Sr}$  of the solar system is best determined using Rb-Sr isotope data for CAIs, which are the oldest dated solids of the solar system and are characterized by sufficiently low Rb/Sr ratios. However, CAIs carry nucleosynthetic Sr isotope anomalies, as manifested in variations in the  $^{84}\text{Sr}/^{86}\text{Sr}$  ratio (internally normalized to a fixed  $^{88}\text{Sr}/^{86}\text{Sr}$ ) (Papanastassiou and Wasserburg, 1978; Moynier et al., 2012; Hans et al., 2013). Depending on whether the Sr isotope anomalies reflect the heterogeneous distribution of Sr from the *p*- (proton-capture), *s*- (slow neutron capture), or *r*-processes (rapid neutron capture), the effects on  $^{87}\text{Sr}/^{86}\text{Sr}$  vary and, as such, impact the estimate for the initial  $^{87}\text{Sr}/^{86}\text{Sr}$  of the solar system. Hans et al. (2013) assumed that the  $^{84}\text{Sr}$  anomalies in CAIs are due to variations in

*r*-process Sr because the same CAIs they analyzed display *r*-process Mo isotope variations (Burkhardt et al., 2011). In this case the initial  $^{87}\text{Sr}/^{86}\text{Sr}$  of CAIs requires an upward correction from the measured value of 0.698930 (re-normalized to 0.710245 for the NIST SRM 987 standard) to a value of 0.698970 (Hans et al., 2013). This higher value happens to be indistinguishable from the initial  $^{87}\text{Sr}/^{86}\text{Sr}$  measured for angrite and eucrite meteorites (Hans et al., 2013), both of which show no nucleosynthetic Sr isotope anomalies (Hans et al., 2013; Schneider et al., 2023). This has motivated some studies to use the initial  $^{87}\text{Sr}/^{86}\text{Sr}$  of these meteorites to represent the initial  $^{87}\text{Sr}/^{86}\text{Sr}$  of the solar system (Mezger et al., 2021). However, it has also been shown that some CAIs exhibit large internal  $^{84}\text{Sr}/^{86}\text{Sr}$  variations accompanied by more subdued variations in  $^{87}\text{Sr}/^{86}\text{Sr}$ , indicating that at least some of the nucleosynthetic Sr isotope anomalies in CAIs reflect heterogeneities solely in the *p*-process nuclide  $^{84}\text{Sr}$  (Charlier et al., 2021). These variations do not require any correction of the  $^{87}\text{Sr}/^{86}\text{Sr}$  ratio, and so the upward correction of the measured initial  $^{87}\text{Sr}/^{86}\text{Sr}$  of CAIs assuming that the Sr isotope anomalies solely reflect *r*-process heterogeneity likely is too large. To account for this uncertainty, we use a solar system initial  $^{87}\text{Sr}/^{86}\text{Sr} = 0.698950 \pm 0.000020$ , which covers the entire range of possible initial values from 0.698930 (i.e., the measured value which would represent the solar system initial provided the  $^{84}\text{Sr}$  anomalies in CAIs entirely reflect *p*-process variations) to 0.698970 (i.e., the corrected CAI initial assuming that the  $^{84}\text{Sr}$  anomalies in CAIs reflect only *r*-process variations).

**Table 5:** Parameters for calculating Rb-Sr model ages.

Parameter	Value	Reference
$\lambda^{87}\text{Rb}$	$1.397 \times 10^{-5} \text{ Ma}^{-1}$	Nebel et al. (2011)
$t_{\text{CAI}}$	$4.56730 \pm 0.00016 \text{ Ga}$	Connelly et al. (2012)
$^{87}\text{Rb}/^{86}\text{Sr}_{\text{FBSE}}$	$0.08 \pm 0.01$	Borg et al. (2022)
$^{87}\text{Rb}/^{86}\text{Sr}_{\text{FMoon}}$	$0.018 \pm 0.006$	Borg et al. (2022)
$^{87}\text{Sr}/^{86}\text{Sr}_{\text{FAN}}$	$0.6990608 \pm 0.0000005$	This study
$t_{\text{FAN}}$	$4.360 \pm 0.003 \text{ Ga}$	Borg et al. (2011)

**Table 6:** Parameters for  $x_{\text{Theia}}$  and  $f_{\text{Theia}}$  according to different impact models (Canup et al., 2023).

<b>Model</b>	<b><math>x_{\text{Theia}}</math></b>	<b><math>f_{\text{Theia}}</math></b>
Canonical giant impact	0.05 – 0.2	0.7 – 0.8
Fast-spinning Earth	0.026 – 0.1	0.04 – 0.15
Half Earth	0.4 – 0.6	0.45 – 0.55

**Table 7:** Parameters for Rb/Sr of proto-Earth and Theia.

	<b>Rb (ppm)</b>	<b>Sr (ppm)</b>	<b><math>^{87}\text{Rb}/^{86}\text{Sr}</math></b>
Proto-Earth	0 – 2.2	8 – 100	0 – 0.8
Theia	0 – 2.2	8 – 100	0 – 0.8

*Concentrations and corresponding  $^{87}\text{Rb}/^{86}\text{Sr}$  ratios reflect minimum and maximum values observed among meteorites [CI chondrites: (e.g., Wasson and Kalleyman 1988) and angrites (e.g., Wang et al., 2024)].*

## 4.5. Appendix Chapter 4

**Table A4.1:** Summary of properties of samples selected for this study.

Sample	Type	Details	References*
15415	Ferroan Anorthosite	<ul style="list-style-type: none"> <li>· Coarse grained plagioclase crystals</li> <li>· Low <math>^{87}\text{Rb}/^{86}\text{Sr} = 0.0024</math></li> <li>· Low but unprecise <math>^{87}\text{Sr}/^{86}\text{Sr} = 0.69914 \pm 5</math></li> <li>· Lower <math>^{142}\text{Nd}</math> suggesting an old formation age</li> </ul>	LSC, Nyquist et al. (1973)
60015	Cataclastic Anorthosite	<ul style="list-style-type: none"> <li>· Pristine interior, up to 3 mm plag crystals</li> <li>· Low bulk <math>^{87}\text{Rb}/^{86}\text{Sr} = 0.047</math></li> <li>· Low but unprecise <math>^{87}\text{Sr}/^{86}\text{Sr} = 0.69902 \pm 10</math></li> </ul>	LSC, Papanastassiou and Wasserburg, (1976)
60025	Ferroan Anorthosite	<ul style="list-style-type: none"> <li>· Intensively studied, coarse grained 'pristine' anorthosite with large plagioclase crystals.</li> <li>· Dated to <math>4.360 \pm 0.003</math> Ga by concordant Pb-Pb and Sm-Nd chronometers</li> <li>· Low <math>^{87}\text{Rb}/^{86}\text{Sr}</math> and low <math>^{87}\text{Sr}/^{86}\text{Sr}</math></li> </ul>	LSC, Borg et al. (2011), Carlson and Lugmair, (1988)
61015	Anorthositic Breccia	<ul style="list-style-type: none"> <li>· Very low Rb reported for plagioclase (&lt; 20 ppb)</li> </ul>	LSC
62255	Ferroan Anorthosite	<ul style="list-style-type: none"> <li>· Up to 6 mm Plag. Grains</li> <li>· Very low Rb (&lt; 20 ppb)</li> <li>· Very low <math>^{142}\text{Nd}</math> suggests old formation age</li> </ul>	LSC, Boyet et al. (2015)
65315	Cataclastic Anorthosite	<ul style="list-style-type: none"> <li>· Badly crushed FAN, relict plag grains up to 4 mm, only px at grain boundaries, not highly shocked</li> <li>· Low <math>^{87}\text{Rb}/^{86}\text{Sr} \approx 0.001</math></li> </ul>	LSC
65325	Cataclastic Anorthosite	<ul style="list-style-type: none"> <li>· Anorthosite with 99% An.</li> <li>· Large 0.1-1 mm plagioclase grains</li> <li>· Low Rb conc. (0.07 ppm)</li> </ul>	LSC
67075	Ferroan Anorthosite	<ul style="list-style-type: none"> <li>· Old Rb-Sr age of 4.47 Ga</li> <li>· Unprecise initial <math>^{87}\text{Sr}/^{86}\text{Sr}</math></li> </ul>	LSC, Nyquist (2010)

\*LSC: Lunar Sample Compendium

**Table A4.2:** Calculated  $^{87}\text{Sr}/^{86}\text{Sr}_{\text{initial}}$  values of the undisturbed plagioclase fractions.

<b>Sample</b>	<b>n</b>	<b><math>^{87}\text{Sr}/^{86}\text{Sr}_{\text{initial}}</math></b>	
60015-p	2	0.699064	± 0.000007
60025-p1	5	0.699060	± 0.000002
60025-p2	3	0.699060	± 0.000002
		0.699060	0.0000007
61015-p	1	0.699061	± 0.000002
62255-r	4	0.699061	± 0.000002
62255-p	5	0.699061	± 0.000001
		0.699061	0.0000003
65325-p	1	0.699059	± 0.000005
<i>Average (± 2s.d.)</i>		<i>0.699061</i>	<i>± 0.000003</i>



**Figure A4.1:** Examples of plagioclase grains separated from lunar ferroan anorthosites.

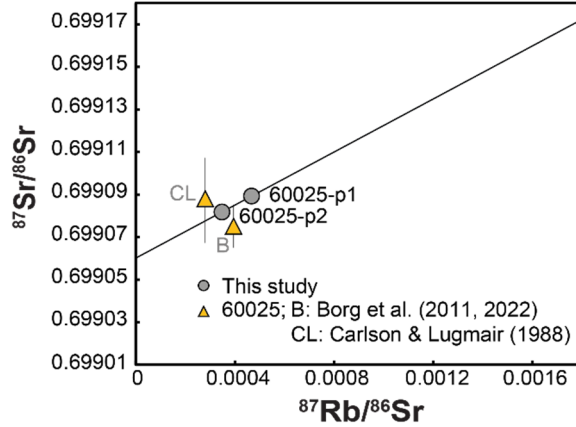


**Figure A4.2:** Comparison of Rb-Sr data for FAN 60025 obtained in this study to previously reported results.

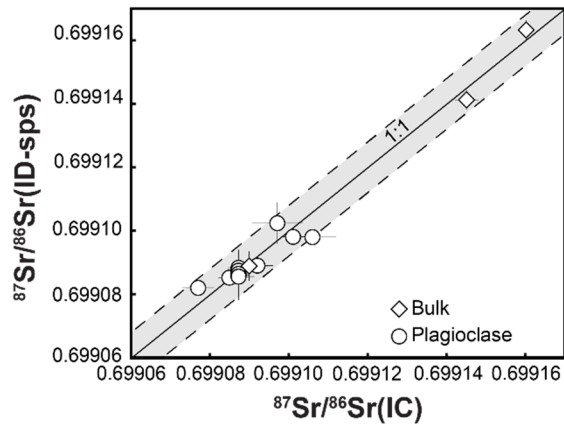


**Figure A4.3:** Comparison of  $^{87}\text{Sr}/^{86}\text{Sr}$  ratios determined on spiked (ID, 'spike subtracted' : sps) and unspiked (IC) aliquots for the FANs of this study. Results for both aliquots agree within the external reproducibility of the Sr isotope measurements (gray band).

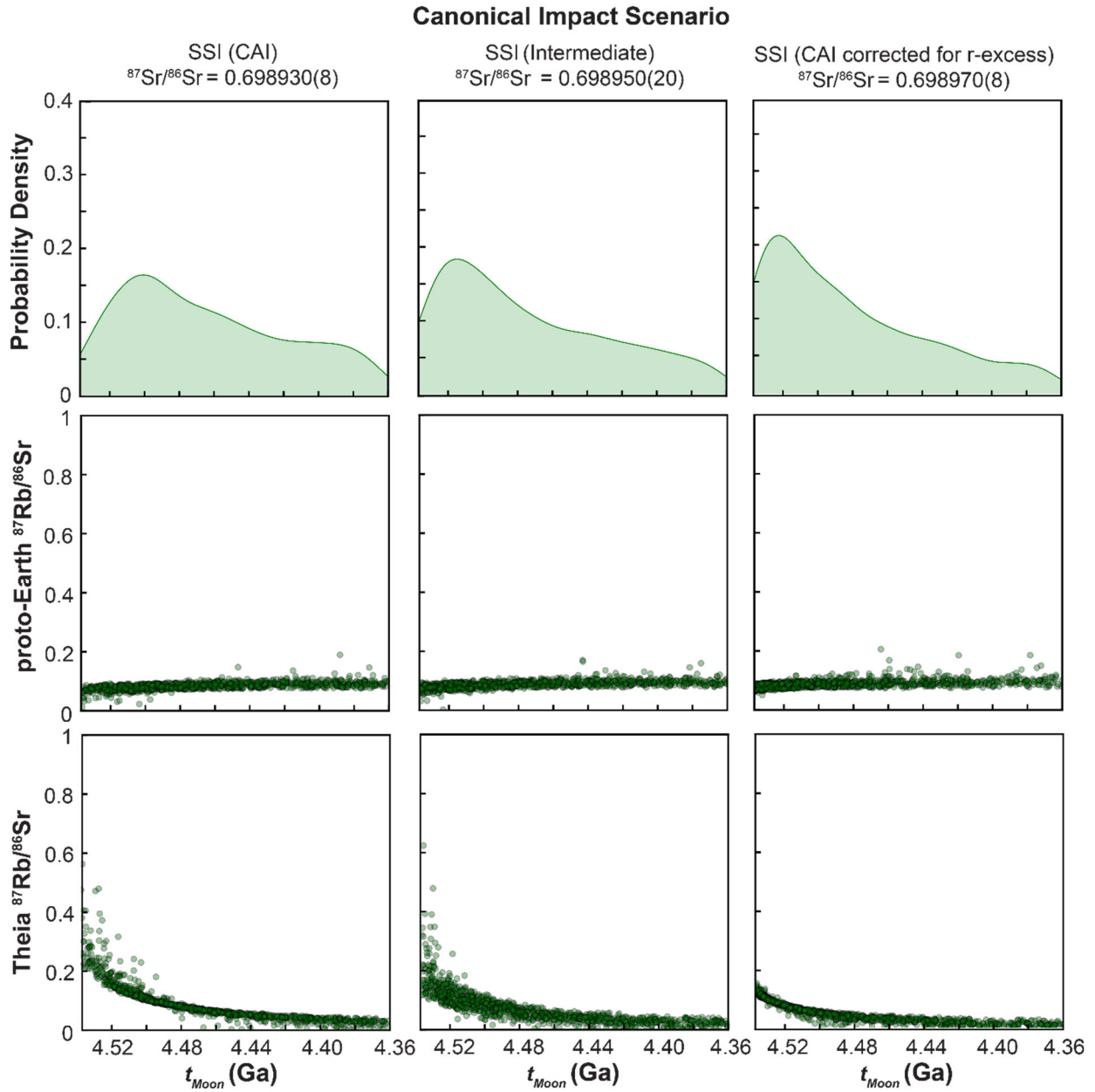


**Figure A4.5:** Successful model results for the canonical impact scenario for different estimates for the initial  $^{87}\text{Sr}/^{86}\text{Sr}$  of the solar system.

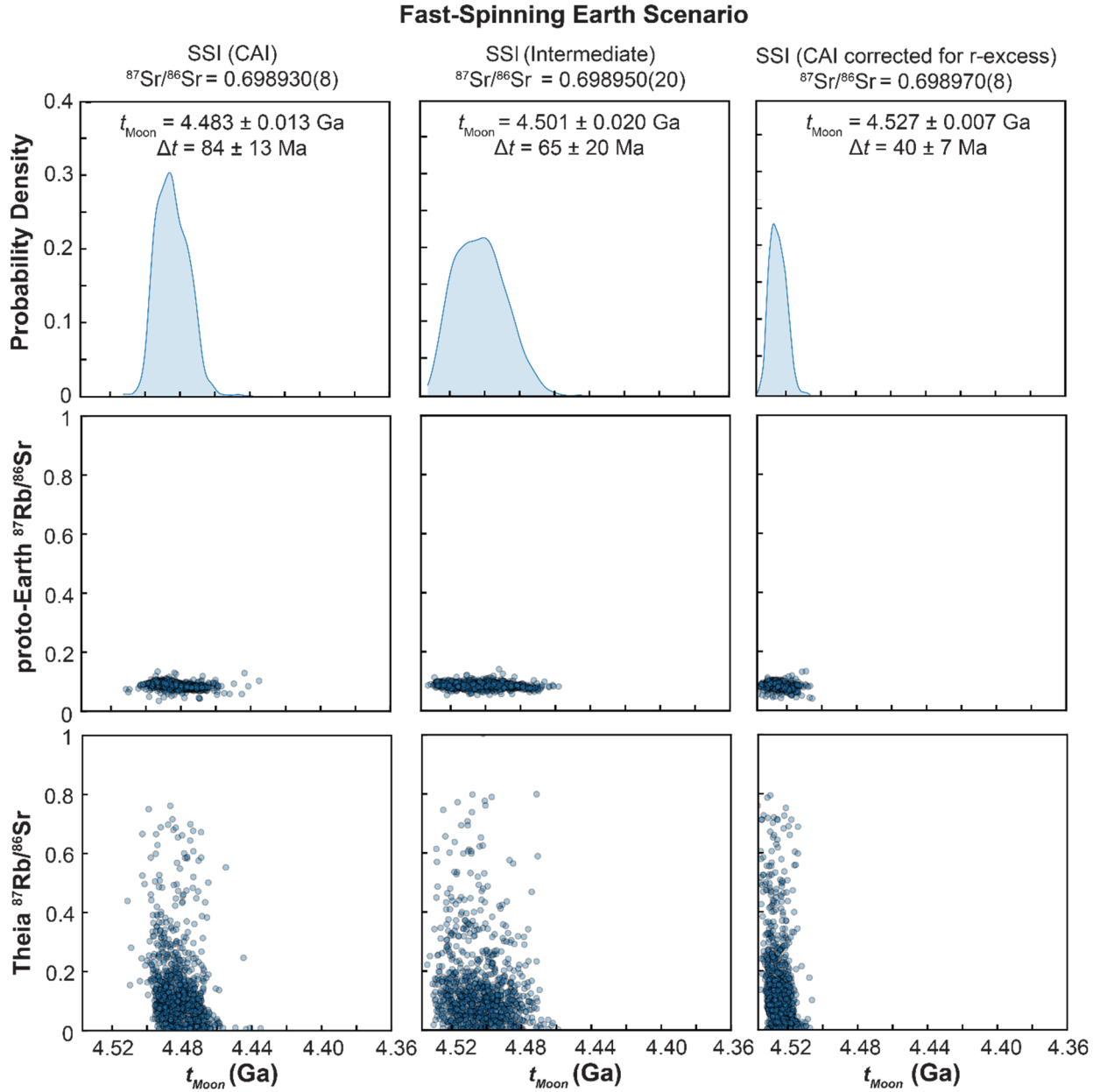


**Figure A4.6:** Successful model results for the fast-spinning Earth scenario for different estimates for the initial  $^{87}\text{Sr}/^{86}\text{Sr}$  of the solar system.

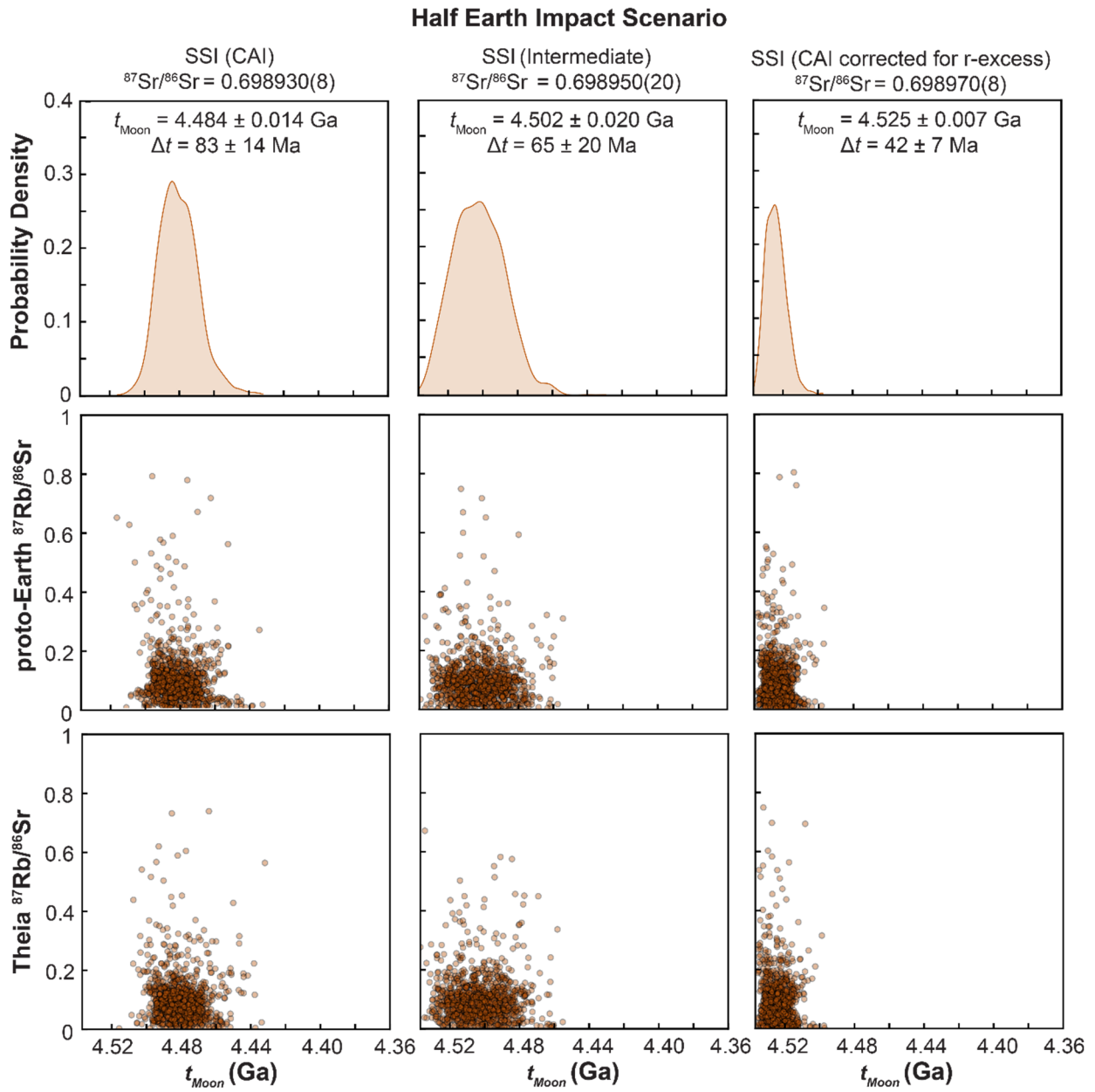


**Figure A4.7:** Successful model results for the half Earth scenario for different estimates for the initial  $^{87}\text{Sr}/^{86}\text{Sr}$  of the solar system.



## 5. Synthesis and Outlook

This thesis showed that Sr isotopes enable investigation of a multitude of questions in cosmochemistry and can provide critical insights into our understanding of the early solar system as well as the timing of moon formation. For this purpose, high-precision measurements of  $^{84}\text{Sr}/^{86}\text{Sr}$  and  $^{87}\text{Sr}/^{86}\text{Sr}$  were used to study nucleosynthetic strontium isotope anomalies among meteorites and the chronology of Moon formation using lunar ferroan anorthosites.

To measure variations in isotopic ratios at the highest level of precision, a thorough understanding of analytically induced uncertainties is critical. One example is the effect of cup degradation in TIMS instruments on the precision and accuracy of isotopic data. This issue was discussed in **Chapter 2**. Traditional static measurement techniques suffer significantly from the successive degradation of the Faraday cups used to collect the ion beams in TIMS instruments, which results in temporal drifts with decreasing cup efficiency. In the case of strontium, dynamic measurements are better suited to yield more precise, consistent, and interlaboratory comparable results. Hence, dynamic measurements should be used whenever possible for Sr isotope analysis.

**Chapter 3** revisited the distribution of nucleosynthetic strontium isotope anomalies in the early solar system by measuring  $\mu^{84}\text{Sr}$  variations among samples from meteorites, Mars, the Earth, and the Moon with a dynamic measurement method. This new precise and consistent dataset demonstrates that the inner solar system (NC meteorites, Mars, the Earth and the Moon) displays homogeneous  $\mu^{84}\text{Sr}$  compositions within  $5 \pm 4$  ppm compared to inconsistent and less precise literature data. While there is variation among outer solar system materials, there is no clear separation of the NC and CC reservoirs (i.e., inner and outer solar system materials) regarding  $\mu^{84}\text{Sr}$  anomalies. Both observations are different from isotopic anomalies in most other elements and thus require another explanation. It can be shown that counterbalancing contributions from *s*-, *r*-, and *p*-process isotopes through variable (*r*-, *p*-) excess and variable *s*-process deficits account for the homogeneity in the

inner solar system and the absence of a clear NC-CC separation in  $\mu^{84}\text{Sr}$ . These new observations argue against the origin of isotopic heterogeneity from thermal processing, as previously suggested based on  $\mu^{84}\text{Sr}$  anomalies, but support the hypothesis of an initial heterogeneity in the protoplanetary accretion disk.

Overall, this study highlights the importance of considering different nucleosynthetic processes as contributors to isotope anomalies in different elements. Most isotope anomalies would be affected by different contributions from *s*-, *r*-, and *p*-process isotopes, and the origin of each isotope anomaly is not always clear. Thus, it would be interesting to investigate more nucleosynthetic isotope anomalies in the framework of counterbalancing contributions from different nucleosynthetic processes. Heavier refractory elements like Sm, Ba, Hf, W, or Os do not show resolved isotope anomalies at the bulk meteorite scale, especially for the NC reservoir. The reason for the absence of isotopic heterogeneity in heavier refractory elements is still under discussion, but the model of counterbalancing contributions from different nucleosynthetic sources (as presented based on Sr isotopes) could be one explanation and should thus be taken into account.

In the last part of the thesis (**Chapter 4**) new high-precision measurements of  $^{87}\text{Sr}/^{86}\text{Sr}$  of several Apollo 16 ferroan anorthosites (FANs) are presented and the data is used to address the timing of lunar crust formation and the age of the Moon. Comparison of the  $^{87}\text{Sr}/^{86}\text{Sr}_{\text{initial}}$  ratios of eight different FANs reveals that five Apollo 16 FANs originated from one single fast-cooled magmatic event on the Moon at  $\sim 4.36$  Ga and formed within a maximum timespan of 28 Ma.

Importantly, the absolute age of anorthosites is not necessarily equivalent to Moon formation, as previously proposed. Instead, independently from the actual age of the samples, the new and precise  $^{87}\text{Sr}/^{86}\text{Sr}_{\text{initial}} = 0.6990608 \pm 0.0000005$  of the Moon allows for the calculation of an Rb-Sr model age of the Moon-forming impact. In contrast to previous attempts at determining the age of the Moon using Rb-Sr systematics, the newly obtained initial  $^{87}\text{Sr}/^{86}\text{Sr}$  value is based on seven samples from five different FANs instead of only one single FAN as in previous works. Furthermore, the approach presented here does not rely on the knowledge of the Rb/Sr ratios of proto-Earth and Theia as these are not known *a priori*.

As the impact parameters are also not well constrained, the age of the Moon was calculated for four different cases. These include a canonical impact, the half Earth scenario, a fast-spinning Earth with a small impactor, and the case of isotopic equilibrium between the Earth and the Moon. A canonical impact is difficult to reconcile with the isotopic homogeneity of the Earth and the Moon and requires an isotopically Earth-like impactor, which is thought to be unlikely. Also, no age can be determined for a canonical impact between  $\sim 4.54$  and  $\sim 4.36$  Ga.

Instead, for scenarios that can account for the isotopic similarity, such as equilibrium but also non-equilibrium scenarios (e.g., the half Earth or fast-spinning Earth scenario), a consistent age of  $4.502 \pm 0.020$  Ga can be determined. This result is reproducible for all three scenarios, which cover a wide range of non-canonical impact scenarios. The obtained age is also in remarkable agreement with the oldest lunar zircon ages and with newer dynamical constraints that predict the giant impact between 50 and 80 Ma after the start of the solar system following a giant planet instability. As such, this study provides new evidence for an early Moon formation  $65 \pm 20$  Ma after solar system formation.

The discrepancy between the formation of the Moon at  $\sim 4.5$  Ga and the formation age of FANs at  $\sim 4.36$  Ga requires an extended lifetime of the LMO of  $\sim 140$  Ma or a global remelting event. It would thus be interesting to perform similar measurements on pristine lunar FANs from other regions of the Moon and expand the data to anorthites in lunar meteorites to circumvent possible sample bias. These could be used to further test, if indeed the LMO was long-lived. Additionally, the possibility of a remelting event should not be left unconsidered. While an early, currently unrecognized giant impact on the Moon might be unlikely to induce global melting, this could be possible by strong tidal heating due to orbital resonances.

In addition, giant impact models need to be further developed to better constrain the giant impact parameters more precisely, which are crucial for determining model ages and the implications of isotopic data. Looking further ahead, samples from inner solar system bodies such as Venus or Mercury could help to assess the likelihood that Theia and proto-Earth were isotopic twins, and thus help to assess the likelihood of a canonical impact.



## References

- Akram W., Schönbacher M., Bisterzo S. and Gallino R. (2015) Zirconium isotope evidence for the heterogeneous distribution of s-process materials in the solar system. *Geochimica et Cosmochimica Acta* **165**, 484–500.
- Alexander C. M. O. (2019) Quantitative models for the elemental and isotopic fractionations in chondrites: The carbonaceous chondrites. *Geochimica et Cosmochimica Acta* **254**, 277–309.
- Anand A., Pape J., Wille M., Mezger K. and Hofmann B. (2021) Early differentiation of magmatic iron meteorite parent bodies from Mn–Cr chronometry. *Geochemical Perspective Letters* **20**, 6–10.
- Andreasen R. and Sharma M. (2007) Mixing and Homogenization in the Early Solar system: Clues from Sr, Ba, Nd, and Sm Isotopes in Meteorites. *The Astrophysical Journal* **665**, 874–883.
- Archer G. J., Brennecka G. A., Gleißner P., Stracke A., Becker H. and Kleine T. (2019) Lack of late-accreted material as the origin of 182W excesses in the Archean mantle: Evidence from the Pilbara Craton, Western Australia. *Earth and Planetary Science Letters* **528**, 115841.
- Arlandini C., Kappeler F., Wisshak K., Gallino R., Lugaro M., Busso M. and Straniero O. (1999) Neutron Capture in Low-Mass Asymptotic Giant Branch Stars: Cross Sections and Abundance Signatures. *The Astrophysical Journal* **525**, 886–900.
- Barboni M., Boehnke P., Keller B., Kohl I. E., Schoene B., Young E. D. and McKeegan K. D. (2017) Early formation of the Moon 4.51 billion years ago. *Science Advances* **3**, e1602365.
- Birmingham K. R., Füri E., Lodders K. and Marty B. (2020) The NC-CC Isotope Dichotomy: Implications for the Chemical and Isotopic Evolution of the Early Solar system. *Space Science Reviews* **216**, 133.
- Birck J.-L. and Allègre C. J. (1988) Manganese - chromium isotope systematics and the development of the early Solar system. *Nature* **331**, 579–584.
- Bischoff A. (2001) Meteorite classification and the definition of new chondrite classes as a result of successful meteorite search in hot and cold deserts. *Planetary and Space Science* **49**, 769–776.
- Bisterzo S., Gallino R., Straniero O., Cristallo S. and Käppeler F. (2011) The s-process in low-metallicity stars - II. Interpretation of high-resolution spectroscopic observations with asymptotic giant branch models: The s-process in low-metallicity stars - II. *Monthly Notices of the Royal Astronomical Society* **418**, 284–319.
- Bisterzo S., Travaglio C., Gallino R., Wiescher M. and Käppeler F. (2014) Galactic Chemical Evolution and Solar s-process Abundances: Dependence on the 13C-Pocket Structure. *The Astrophysical Journal* **787**, 10.
- Borg L. E. and Carlson R. W. (2023) The Evolving Chronology of Moon Formation. *Annual Reviews of Earth and Planetary Sciences* **51**, 031621-060538.
- Borg L. E., Brennecka G. A. and Kruijjer T. S. (2022) The origin of volatile elements in the Earth–Moon system. *Proceedings of the National Academy of Sciences* **119**, e2115726119.

- Borg L. E., Connelly J. N., Boyet M. and Carlson R. W. (2011) Chronological evidence that the Moon is either young or did not have a global magma ocean. *Nature* **477**, 70–72.
- Borg L. E., Connelly J. N., Cassata W. S., Gaffney A. M. and Bizzarro M. (2017) Chronologic implications for slow cooling of troctolite 76535 and temporal relationships between the Mg-suite and the ferroan anorthosite suite. *Geochimica et Cosmochimica Acta* **201**, 377–391.
- Borg L. E., Gaffney A. M. and Shearer C. K. (2015) A review of lunar chronology revealing a preponderance of 4.34–4.37 Ga ages. *Meteoritics & Planetary Science* **50**, 715–732.
- Borg L. E., Gaffney A. M., Kruijer T. S., Marks N. A., Sio C. K. and Wimpenny J. (2019) Isotopic evidence for a young lunar magma ocean. *Earth and Planetary Science Letters* **523**, 115706.
- Bouvier A. and Wadhwa M. (2010) The age of the Solar system redefined by the oldest Pb–Pb age of a meteoritic inclusion. *Nature Geoscience* **3**, 637–641.
- Boyet M., Carlson R. W., Borg L. E. and Horan M. (2015) Sm–Nd systematics of lunar ferroan anorthositic suite rocks: Constraints on lunar crust formation. *Geochimica et Cosmochimica Acta* **148**, 203–218.
- Brasser R. and Mojzsis S. J. (2020) The partitioning of the inner and outer Solar system by a structured protoplanetary disk. *Nature Astronomy* **4**, 492–499.
- Brennecka G. A. and Kleine T. (2017) A Low Abundance of  $^{135}\text{Cs}$  in the Early Solar system from Barium Isotopic Signatures of Volatile-depleted Meteorites. *The Astrophysical Journal Letters* **837**, L9.
- Brennecka G. A., Borg L. E. and Wadhwa M. (2013) Evidence for supernova injection into the solar nebula and the decoupling of r-process nucleosynthesis. *Proceedings of the National Academy of Sciences of the United States of America* **110**, 17241–17246.
- Brennecka G. A., Burkhardt C., Budde G., Kruijer T. S., Nimmo F. and Kleine T. (2020) Astronomical context of Solar system formation from molybdenum isotopes in meteorite inclusions. *Science* **370**, 837–840.
- Budde G., Burkhardt C., and Kleine T. (2019) Molybdenum isotopic evidence for the late accretion of outer Solar system material to Earth. *Nature Astronomy* **3**, 736–741.
- Budde G., Burkhardt C., Brennecka G. A., Fischer-Gödde M., Kruijer T. S. and Kleine T. (2016) Molybdenum isotopic evidence for the origin of chondrules and a distinct genetic heritage of carbonaceous and non-carbonaceous meteorites. *Earth and Planetary Science Letters* **454**, 293–303.
- Budde G., Kruijer T. S. and Kleine T. (2018) Hf–W chronology of CR chondrites: Implications for the timescales of chondrule formation and the distribution of  $^{26}\text{Al}$  in the solar nebula. *Geochimica et Cosmochimica Acta* **222**, 284–304.
- Burbidge E. M., Burbidge G. R., Fowler W. A. and Hoyle F. (1957) Synthesis of the Elements in Stars. *Reviews of Modern Physics* **29**, 547–650.
- Burkhardt C., Dauphas N., Hans U., Bourdon B. and Kleine T. (2019) Elemental and isotopic variability in solar system materials by mixing and processing of primordial disk reservoirs. *Geochimica et Cosmochimica Acta* **261**, 145–170.
- Burkhardt C., Kleine T., Oberli F., Pack A., Bourdon B. and Wieler R. (2011) Molybdenum isotope anomalies in meteorites: Constraints on solar nebula evolution and origin of the Earth. *Earth and Planetary Science Letters* **312**, 390–400.

- Burkhardt C., Spitzer F., Morbidelli A., Budde G., Render J. H., Kruijer T. S. and Kleine T. (2021) Terrestrial planet formation from lost inner solar system material. *Science Advances* **7**, 1–12.
- Cameron A. G. W. and Ward, W. R. (1976) *Lunar Planetary Science Conference Abstract* **7**, 120.
- Cano E. J., Sharp Z. D. and Shearer C. K. (2020) Distinct oxygen isotope compositions of the Earth and Moon. *Nature Geoscience* **13**, 270–274.
- Canup R. M. (2012) Forming a moon with an Earth-like composition via a giant impact. *Science* **338**, 1052–1055.
- Canup R. M. (2014) Lunar-forming impacts: Processes and alternatives. *Philosophical Transactions of the Royal Society A: Mathematical, Physical and Engineering Sciences* **372**, 20130175.
- Canup R. M. and Asphaug E. (2001) Origin of the Moon in a giant impact near the end of the Earth's formation. *Nature* **412**, 708–712.
- Canup R. M., Richter K., Dauphas N., Pahlevan K., Ćuk M., Lock S. J., Stewart S. T., Salmon J., Rufu R., Nakajima M. and Magna T. (2023) Origin of the Moon. *Reviews in Mineralogy and Geochemistry* **89**, 53–102.
- Carlson R. W. and Lugmair G. W. (1988) The age of ferroan anorthosite 60025: oldest crust on a young Moon? *Earth and Planetary Science Letters* **90**, 119–130.
- Chambers J. (2014) Planet Formation, in: Davis A. M. (Ed.), *Treatise on Geochemistry*, 2 ed. Elsevier, Oxford, pp. 55–72.
- Charlier B. L. A., Tissot F. L. H., Vollstaedt H., Dauphas N., Wilson C. J. N. and Marquez R. T. (2021) Survival of presolar *p*-nuclide carriers in the nebula revealed by stepwise leaching of Allende refractory inclusions. *Science Advances* **7**, eabf6222.
- Charnoz S., Sossi P. A., Lee Y.-N., Siebert J., Hyodo R., Allibert L., Pignatale F. C., Landeau M., Oza A. V. and Moynier F. (2021) Tidal pull of the Earth strips the proto-Moon of its volatiles. *Icarus* **364**, 114451.
- Clayton R. N. and Mayeda T. K. (1975) Genetic relations between the moon and meteorites. *Lunar and Planetary Science Conference Proceedings* **2**, 1761–1769.
- Connelly J. N., Bizzarro M., Krot A. N., Nordlund Å., Wielandt D. and Ivanova M. A. (2012) The absolute chronology and thermal processing of solids in the solar protoplanetary disk. *Science* **338**, 651–655.
- Cornet M., Fitoussi C., Bourdon B. and Pili E. (2022) Determination of chromium isotopic composition in various geological material by thermal ionization mass spectrometry. *International Journal of Mass Spectrometry* **480**, 116897.
- Ćuk M. and Stewart S. T. (2012) Making the Moon from a Fast-Spinning Earth: A Giant Impact Followed by Resonant Despinning. *Science* **338**, 1047–1052.
- Darwin G. H. (1879) I. On the bodily tides of viscous and semi-elastic spheroids, and on the ocean tides upon a yielding nucleus. *Transactions of the Philosophical Society* **170**.
- Dauphas N. and Schauble E. A. (2016) Mass Fractionation Laws, Mass-Independent Effects, and Isotopic Anomalies. *Annual Reviews of Earth and Planetary Sciences* **44**, 709–783.
- Dauphas N., Burkhardt C., Warren P. H. and Fang-Zhen T. (2014a) Geochemical arguments for an Earth-like Moon-forming impactor. *Philosophical Transactions A. Mathematics Physics and Engineering. Sciences* **372**, 20130244.
- Dauphas N., Chen J. H., Zhang J., Papanastassiou D. A., Davis A. M. and Travaglio C. (2014b) Calcium-48 isotopic anomalies in bulk chondrites and achondrites: Evidence for a

- uniform isotopic reservoir in the inner protoplanetary disk. *Earth and Planetary Science Letters* **407**, 96–108.
- Dauphas N., Marty B. and Reisberg L. (2002) Inference on terrestrial genesis from molybdenum isotope systematics. *Geophysical Research Letters* **29**, 8-1-8-3.
- Di Y., Krestianinov E., Zink S. and Amelin Y. (2021) High-precision multidynamic Sr isotope analysis using thermal ionization mass spectrometer (TIMS) with correction of fractionation drift. *Chemical Geology* **582**, 120411.
- Elardo S. M., Draper D. S. and Shearer C. K. (2011) Lunar Magma Ocean crystallization revisited: Bulk composition, early cumulate mineralogy, and the source regions of the highlands Mg-suite. *Geochimica et Cosmochimica Acta* **75**, 3024–3045.
- Elkins-Tanton L. T., Burgess S. and Yin Q. Z. (2011) The lunar magma ocean: Reconciling the solidification process with lunar petrology and geochronology. *Earth and Planetary Science Letters* **304**, 326–336.
- Faure G. and Powell J. L. (1972) Strontium Isotope Geology, *Springer-Verlag*, Berlin
- Fischer R. A., Zube N. G. and Nimmo F. (2021) The origin of the Moon's Earth-like tungsten isotopic composition from dynamical and geochemical modeling. *Nature Communications* **12**, 35.
- Fischer, M. (2021) Triple oxygen isotope study on the Earth-Moon system (*Doctoral dissertation, Georg-August-Universität Göttingen*), doi.org/10.53846/goediss-9028.
- Fischer-Gödde M. and Kleine T. (2017) Ruthenium isotopic evidence for an inner Solar system origin of the late veneer. *Nature* **541**, 525–527.
- Frebel A. (2014) Reconstructing the Cosmic Evolution of the Chemical Elements. *Daedalus* **143**, 71–80.
- Fukai R. and Yokoyama T. (2019) Nucleosynthetic Sr–Nd Isotope Correlations in Chondrites: Evidence for Nebular Thermal Processing and Dust Transportation in the Early Solar system. *The Astrophysical Journal* **879**, 79.
- Fukai R., Yokoyama T. and Kagami S. (2017) Evaluation of the long-term fluctuation in isotope ratios measured by TIMS with the static, dynamic, and multistatic methods: A case study for Nd isotope measurements. *International Journal of Mass Spectrometry* **414**, 1–7.
- Gaffney A. M. and Borg L. E. (2014) A young solidification age for the lunar magma ocean. *Geochimica et Cosmochimica Acta* **140**, 227–240.
- Gaffney, A.M., Gross, J., Borg, L.E., Hanna, K.L.D., Draper, D.S., Dygert, N., Elkins-Tanton, L.T., Prissel, K.B., Prissel, T.C., Steenstra, E.S., and van Westrenen, W. (2023) Magmatic Evolution I: Initial Differentiation of the Moon. *Reviews in Mineralogy and Geochemistry* **2023**; **89**, 103–145.
- Greaves J. S. (2005) Disks Around Stars and the Growth of Planetary Systems. *Science* **307**, 68–71.
- Greer J., Zhang B., Isheim D., Seidman D. N., Bouvier A. and Heck P. R. (2023) 4.46 Ga zircons anchor chronology of lunar magma ocean. *Geochemical Perspective Letters* **27**, 49–53.
- Grossman L. (1972) Condensation in the primitive solar nebula. *Geochimica et Cosmochimica Acta* **36**, 597–619.
- Halliday A. N. (2008) A young Moon-forming giant impact at 70–110 million years accompanied by late-stage mixing, core formation and degassing of the Earth. *Philosophical Transactions of the Royal Society Advances* **366**, 4163–4181.

- Hans U., Kleine T. and Bourdon B. (2013) Rb–Sr chronology of volatile depletion in differentiated protoplanets: BABI, ADOR and ALL revisited. *Earth and Planetary Science Letters* **374**, 204–214.
- Hartmann W. K. and Davis D. R. (1975) Satellite-sized planetesimals and lunar origin. *Icarus* **24**, 504–515.
- Hellmann J. L., Schneider J. M., Wölfer E., Drązkowska J., Jansen C. A., Hopp T., Burkhardt C. and Kleine T. (2023) Origin of Isotopic Diversity among Carbonaceous Chondrites. *The Astrophysical Journal Letters* **946**, L34.
- Henshall T., Cook D. L., Garçon M. and Schönbachler M. (2018) High-precision strontium isotope analysis of geological samples by thermal ionisation mass spectrometry. *Chemical Geology* **482**, 113–120.
- Herwartz D., Pack A., Friedrichs B. and Bischoff A. (2014) Identification of the giant impactor Theia in lunar rocks. *Science* **344**, 1146–1150.
- Hopp T., Budde G. and Kleine T. (2020) Heterogeneous accretion of Earth inferred from Mo–Ru isotope systematics. *Earth and Planetary Science Letters* **534**, 116065.
- Hoppe P. and Zinner E. (2000) Presolar dust grains from meteorites and their stellar sources. *Journal of Geophysical Research: Space Physics* **105**, 10371–10385.
- Hosono N., Karato S., Makino J. and Saitoh T. R. (2019) Terrestrial magma ocean origin of the Moon. *Nature Geoscience* **12**, 418–423.
- Huss G. R., Keil K. and Taylor G. J. (1981) The matrices of unequilibrated ordinary chondrites: Implications for the origin and history of chondrites. *Geochimica et Cosmochimica Acta* **45**, 33–51.
- Jacobson S. A., Morbidelli A., Raymond S. N., O’Brien D. P., Walsh K. J. and Rubie D. C. (2014) Highly siderophile elements in Earth’s mantle as a clock for the Moon-forming impact. *Nature* **508**, 84–87.
- Jacquet E., Pignatale F. C., Chaussidon M. and Charnoz S. (2019) Fingerprints of the Protosolar Cloud Collapse in the Solar system. II. Nucleosynthetic Anomalies in Meteorites. *The Astrophysical Journal* **884**, 32.
- Johansen A. and Youdin A. (2007) Protoplanetary Disk Turbulence Driven by the Streaming Instability: Non-Linear Saturation and Particle Concentration. *The Astrophysical Journal* **662**, 627–641.
- Käppeler F., Gallino R., Bisterzo S. and Aoki W. (2011) The s process: Nuclear physics, stellar models, and observations. *Reviews of Modern Physics* **83**, 157–193.
- Kleine T. and Walker R. J. (2017) Tungsten Isotopes in Planets. *Annual Review of Earth and Planetary Sciences* **45**, 389–417.
- Kleine T., Budde G., Burkhardt C., Kruijjer T. S., Worsham E. A., Morbidelli A. and Nimmo F. (2020) The Non-carbonaceous–Carbonaceous Meteorite Dichotomy. *Space Science Reviews* **216**.
- Kruijjer T. S., Archer G. J. and Kleine T. (2021) No 182W evidence for early Moon formation. *Nature Geoscience* **14**, 714–715.
- Kruijjer T. S., Burkhardt C., Budde G. and Kleine T. (2017) Age of Jupiter inferred from the distinct genetics and formation times of meteorites. *Proceedings of the National Academy of Sciences* **114**, 6712–6716.
- Kruijjer T. S., Kleine T. and Borg L. E. (2020) The great isotopic dichotomy of the early Solar system. *Nature Astronomy* **4**, 32–40.

- Kruijer T. S., Kleine T., Fischer-Gödde M. and Sprung P. (2015) Lunar tungsten isotopic evidence for the late veneer. *Nature* **520**, 534–537.
- Kruijer T. S., Kleine T., Fischer-Gödde M. and Sprung P. (2015) Lunar tungsten isotopic evidence for the late veneer. *Nature* **520**, 534–537.
- Lichtenberg T., Drażkowska J., Schönbächler M., Golabek G. J. and Hands T. O. (2021) Bifurcation of planetary building blocks during Solar system formation. *Science* **371**, 365–370.
- Liu N., Savina M. R., Gallino R., Davis A. M., Bisterzo S., Gyngard F., Käppeler F., Cristallo S., Dauphas N., Pellin M. J. and Dillmann I. (2015) Correlated strontium and barium isotopic compositions of acid-cleaned single mainstream silicon carbides from Murchison. *The Astrophysical Journal* **803**, 1–23.
- Lock S. J., Stewart S. T., Petaev M. I., Leinhardt Z., Mace M. T., Jacobsen S. B. and Čuk M. (2018) The Origin of the Moon Within a Terrestrial Synestia. *Journal of Geophysical Research: Planets* **123**, 910–951.
- Lodders K. and Amari S. (2005) Presolar grains from meteorites: Remnants from the early times of the solar system. *Geochemistry* **65**, 93–166.
- Lugaro M., Davis A. M., Gallino R., Pellin M. J., Straniero O. and Käppeler F. (2003) Isotopic Compositions of Strontium, Zirconium, Molybdenum, and Barium in Single Presolar SiC Grains and Asymptotic Giant Branch Stars. *The Astrophysical Journal* **593**, 486–508.
- Lugmair G. W. and Shukolyukov A. (1998) Early solar system timescales according to <sup>53</sup>Mn-<sup>53</sup>Cr systematics. *Geochimica et Cosmochimica Acta* **62**, 2863–2886.
- Maurice M., Tosi N., Schwinger S., Breuer D. and Kleine T. (2020) A long-lived magma ocean on a young Moon. *Science Advances* **6**.
- McSween H. Y. and Richardson S. M. (1977) The composition of carbonaceous chondrite matrix. *Geochimica et Cosmochimica Acta* **41**, 1145–1161.
- Meija J., Coplen T. B., Berglund M., Brand W. A., Bièvre P. D., Gröning M., Holden N. E., Irrgeher J., Loss R. D., Walczyk T. and Prohaska T. (2016) Isotopic compositions of the elements 2013 (IUPAC Technical Report). *Pure and Applied Chemistry* **88**, 293–306.
- Melosh H. J. (2014) New approaches to the Moon's isotopic crisis. *Philosophical Transactions of the Royal Society A: Mathematical, Physical and Engineering Sciences* **372**, 20130168.
- Mezger K., Maltese A. and Vollstaedt H. (2021) Accretion and differentiation of early planetary bodies as recorded in the composition of the silicate Earth. *Icarus* **365**, 114497.
- Michaut C. and Neufeld J. A. (2022) Formation of the Lunar Primary Crust From a Long-Lived Slushy Magma Ocean. *Geophysical Research Letters* **49**, e2021GL095408.
- Morbidelli A., Baillié K., Batygin K., Charnoz S., Guillot T., Rubie D. C. and Kleine T. (2022) Contemporary formation of early Solar system planetesimals at two distinct radial locations. *Nature Astronomy* **6**, 72–79.
- Morishima R. and Watanabe S. (2001) Two types of co-accretion scenarios for the origin of the Moon. *Earth Planets and Space* **53**, 213–231.
- Mougel B., Moynier F. and Göpel C. (2018) Chromium isotopic homogeneity between the Moon, the Earth, and enstatite chondrites. *Earth and Planetary Science Letters* **481**, 1–8.

- Moynier F., Day J. M. D., Okui W., Yokoyama T., Bouvier A., Walker R. J. and Podosek F. A. (2012) Planetary-scale strontium isotopic heterogeneity and the age of volatile depletion of early solar system materials. *The Astrophysical Journal* **758**.
- Myojo K., Yokoyama T., Okabayashi S., Wakaki S., Sugiura N. and Iwamori H. (2018) The Origin and Evolution of Nucleosynthetic Sr Isotope Variability in Calcium and Aluminum-rich Refractory Inclusions. *The Astrophysical Journal* **853**, 48.
- Nakajima M., Genda H., Asphaug E. and Ida S. (2022) Large planets may not form fractionally large moons. *Nature Communications* **13**, 568.
- Nanne J. A. M., Nimmo F., Cuzzi J. N. and Kleine T. (2019) Origin of the non-carbonaceous-carbonaceous meteorite dichotomy. *Earth and Planetary Science Letters* **511**, 44–54.
- Nebel O. and Stammer J. A. (2016) Strontium Isotopes. In *Encyclopedia of Geochemistry: A Comprehensive Reference Source on the Chemistry of the Earth* (ed. W. M. White). Springer International Publishing, Cham. pp. 1–6.
- Nebel O., Mezger K., Scherer E. E. and Münker C. (2005) High precision determinations of  $^{87}\text{Rb}/^{85}\text{Rb}$  in geologic materials by MC-ICP-MS. *International Journal of Mass Spectrometry* **246**, 10–18.
- Nebel O., Scherer E. E. and Mezger K. (2011) Evaluation of the  $^{87}\text{Rb}$  decay constant by age comparison against the U–Pb system. *Earth and Planetary Science Letters* **301**, 1–8.
- Nemchin A., Timms N., Pidgeon R., Geisler T., Reddy S. and Meyer C. (2009) Timing of crystallization of the lunar magma ocean constrained by the oldest zircon. *Nature Geoscience* **2**, 133–136.
- Nicolussi G. K., Pellin M. J., Lewis R. S., Davis A. M., Clayton R. N. and Amari S. (1998) Strontium Isotopic Composition in Individual Circumstellar Silicon Carbide Grains: A Record of s-Process Nucleosynthesis. *Physical Review Letters* **81**, 3583.
- Nimmo F. and Kleine T. (2015) Early Differentiation and Core Formation. In *The Early Earth* American Geophysical Union (AGU). pp. 83–102.
- Nyquist L. E., Hubbard N. J., Jahn B., Bansal B. M., Wiesmann H. and Gast P. W. (1973) Rb-Sr systematics for chemically defined Apollo 15 and 16 materials. *Proceedings of the Lunar Science Conference* **4**, 1832.
- Nyquist L. E., Shih C.-Y., Bogard D. D. and Yamaguchi A. (2010) Lunar Crustal History from Isotopic Studies of Lunar Anorthosites. In *Global Lunar Conference of the International Astronautical Federation. Beijing. GLUC-2010.1.1. A.4*
- Pahlevan K. and Stevenson D. J. (2007) Equilibration in the aftermath of the lunar-forming giant impact. *Earth and Planetary Science Letters* **262**, 438–449.
- Papanastassiou D. A. and Wasserburg G. J. (1968) Initial strontium isotopic abundances and the resolution of small time differences in the formation of planetary objects. *Earth and Planetary Science Letters* **5**, 361–376.
- Papanastassiou D. A. and Wasserburg G. J. (1978) Strontium isotopic anomalies in the Allende Meteorite. *Geophysical Research Letters* **5**, 595–598.
- Papanastassiou D. A., Wasserburg G. J., Burnett D. S. 1970. Rb-Sr ages of lunar rocks from the Sea of Tranquility. *Earth and Planetary Science Letters* **8**:1–19
- Papanastassiou, D. A. and Wasserburg, G. J. (1976) Early Lunar Differentiates and Lunar Initial  $^{87}\text{Sr}/^{86}\text{Sr}$ . *Abstracts of the Lunar and Planetary Science Conference* **7**, 665.
- Paton C., Schiller M. and Bizzarro M. (2013) Identification of an  $^{84}\text{Sr}$ -depleted carrier in primitive meteorites and implications for thermal processing in the solar protoplanetary disk. *Astrophysical Journal Letters* **763**, 2–7.

- Pignatari M., Herwig F., Hirschi R., Bennett M., Rockefeller G., Fryer C., Timmes F. X., Ritter C., Heger A., Jones S., Battino U., Dotter A., Trappitsch R., Diehl S., Frischknecht U., Hungerford A., Magkotsios G., Travaglio C. and Young P. (2016) NuGrid Stellar Data Set. I. Stellar Yields from H to Bi for Stars with Metallicities  $Z = 0.02$  and  $Z = 0.01$ . *The Astrophysical Journal Supplement Series* **225**, 24.
- Poole G. (2013) Nucleosynthetic isotope anomalies in meteorites-clues for solar system origin. *Geology Today* **29**, 190–194.
- Poole G. M., Rehkämper M., Coles B. J., Goldberg T. and Smith C. L. (2017) Nucleosynthetic molybdenum isotope anomalies in iron meteorites – new evidence for thermal processing of solar nebula material. *Earth and Planetary Science Letters* **473**, 215–226.
- Prissel T.C., Parman S.W., Head J.W. (2016) Formation of the Lunar Highlands Mg-suite as told by Spinel. *American Mineralogist* **101**, 1624–1635
- Qin L. and Wang X. (2017) Chromium Isotope Geochemistry. *Reviews in Mineralogy and Geochemistry* **82**, 379–414.
- Qin L., Alexander C. M. O., Carlson R. W., Horan M. F. and Yokoyama T. (2010) Contributors to chromium isotope variation of meteorites. *Geochimica et Cosmochimica Acta* **74**, 1122–1145.
- Qin L., Carlson R. W. and Alexander C. M. O. (2011) Correlated nucleosynthetic isotopic variability in Cr, Sr, Ba, Sm, Nd and Hf in Murchison and QUE 97008. *Geochimica et Cosmochimica Acta* **75**, 7806–7828.
- Raymond S. N. and Morbidelli A. (2014) The Grand Tack model: a critical review. *Proceedings of the International Astronomical Union* **9**, 194–203.
- Regelous M., Elliott T. and Coath C. D. (2008) Nickel isotope heterogeneity in the early Solar system. *Earth and Planetary Science Letters* **272**, 330–338.
- Render J. and Brennecka G. A. (2021) Isotopic signatures as tools to reconstruct the primordial architecture of the Solar system. *Earth and Planetary Science Letters* **555**, 116705.
- Render J., Brennecka G. A., Burkhardt C. and Kleine T. (2022) Solar system evolution and terrestrial planet accretion determined by Zr isotopic signatures of meteorites. *Earth and Planetary Science Letters* **595**, 117748.
- Reufer A., Meier M. M. M., Benz W. and Wieler R. (2012) A hit-and-run giant impact scenario. *Icarus* **221**, 296–299.
- Roberti L., Pignatari M., Psaltis A., Sieverding A., Mohr P., Fülöp Z. and Lugaro M. (2023) The  $\gamma$ -process nucleosynthesis in core-collapse supernovae - I. A novel analysis of  $\gamma$ -process yields in massive stars. *Astronomy and Astrophysics* **677**, A22.
- Rotaru M., Birck J. L. and Allègre C. J. (1992) Clues to early Solar system history from chromium isotopes in carbonaceous chondrites. *Nature* **358**, 465–470.
- Russell S. S., Connolly Jr. H. C. and Krot A. N. (2018) Chondrules., *Cambridge University Press*.
- Russell W. A., Papanastassiou D. A. and Tombrello T. A. (1978) Ca isotope fractionation on the Earth and other solar system materials. *Geochimica et Cosmochimica Acta* **42**, 1075–1090.
- Schiller M., Bizzarro M. and Fernandes V. A. (2018) Isotopic evolution of the protoplanetary disk and the building blocks of Earth and the Moon. *Nature* **555**, 507–510.

- Schneider J. M., Burkhardt C. and Kleine T. (2023) Distribution of s-, r-, and p-process Nuclides in the Early Solar system Inferred from Sr Isotope Anomalies in Meteorites. *The Astrophysical Journal Letters* **952**, L25.
- Schneider J. M., Burkhardt C., Marrocchi Y., Brennecka G. A. and Kleine T. (2020) Early evolution of the solar accretion disk inferred from Cr-Ti-O isotopes in individual chondrules. *Earth and Planetary Science Letters* **551**, 116585.
- Scott E. R. D. (2007) Chondrites and the Protoplanetary Disk. *Annual Review of Earth and Planetary Sciences* **35**, 577–620.
- See T. J. J. (1909) The Capture Theory of Satellites. *Publications of the Astronomical Society of the Pacific* **21**, 167–173.
- Shields W. R., Murphy T. J., Catanzaro E. J. and Garner E. L. (1966) Absolute isotopic abundance ratios and the atomic weight of a reference sample of chromium. *Journal of Research of the National Bureau of Standards Sect. A* **70A**, 193.
- Shollenberger Q. R., Borg L. E., Ramon E. C., Sharp M. A. and Brennecka G. A. (2021) Samarium isotope compositions of uranium ore concentrates: A novel nuclear forensic signature. *Talanta* **221**, 121431.
- Shollenberger Q. R., Render J. and Brennecka G. A. (2018) Er, Yb, and Hf isotopic compositions of refractory inclusions: An integrated isotopic fingerprint of the Solar system's earliest reservoir. *Earth and Planetary Science Letters* **495**, 12–23.
- Sio C. K., Borg L. E. and Cassata W. S. (2020) The timing of lunar solidification and mantle overturn recorded in ferroan anorthosite 62237. *Earth and Planetary Science Letters* **538**, 116219.
- Smith J.V., Anderson A.T., Newton R.C., Olsen E.J., Wyllie P.J. (1970) Petrologic history of the Moon inferred from petrography, mineralogy, and petrogenesis of Apollo 11 rocks. *Geochimica et Cosmochimica Acta (Supp.)* **11**, 897–925.
- Snyder G.A., Taylor L.A., Halliday A.N. (1995) Chronology and petrogenesis of the lunar highlands suite: Cumulates from KREEP basalt crystallization. *Geochimica et Cosmochimica Acta* **59**, 1185–1203.
- Spitzer F., Burkhardt C., Budde G., Kruijjer T. S., Morbidelli A. and Kleine T. (2020) Isotopic Evolution of the Inner Solar system Inferred from Molybdenum Isotopes in Meteorites. *The Astrophysical Journal Letters* **898**, L2.
- Spitzer F., Burkhardt C., Nimmo F. and Kleine T. (2021) Nucleosynthetic Pt isotope anomalies and the Hf-W chronology of core formation in inner and outer solar system planetesimals. *Earth and Planetary Science Letters* **576**, 117211.
- Sprung P., Kleine T. and Scherer E. E. (2013) Isotopic evidence for chondritic Lu/Hf and Sm/Nd of the Moon. *Earth and Planetary Science Letters* **380**, 77–87.
- Steller T., Burkhardt C., Yang C. and Kleine T. (2022) Nucleosynthetic zinc isotope anomalies reveal a dual origin of terrestrial volatiles. *Icarus* **386**, 115171.
- Stracke A., Scherer E. E. and Reynolds B. C. (2014) Application of Isotope Dilution in Geochemistry. In *Treatise on Geochemistry* Elsevier. pp. 71–86.
- Taylor D. J., McKeegan K. D. and Harrison T. M. (2009) Lu–Hf zircon evidence for rapid lunar differentiation. *Earth and Planetary Science Letters* **279**, 157–164.
- Tera F., Papanastassiou D. A. and Wasserburg G. J. (1974) Isotopic evidence for a terminal lunar cataclysm. *Earth and Planetary Science Letters* **22**, 1–21.

- Thiemens M. M., Sprung P., Fonseca R. O. C., Leitzke F. P. and Münker C. (2019) Early Moon formation inferred from hafnium–tungsten systematics. *Nature Geoscience* **12**, 696–700.
- Touboul M., Kleine T., Bourdon B., Palme H. and Wieler R. (2007) Late formation and prolonged differentiation of the Moon inferred from W isotopes in lunar metals. *Nature* **450**, 1206–1209.
- Touboul M., Puchtel I. S. and Walker R. J. (2015) Tungsten isotopic evidence for disproportional late accretion to the Earth and Moon. *Nature* **520**, 530–533.
- Travaglio C., Gallino R., Arnone E., Cowan J., Jordan F. and Sneden C. (2004) Galactic Evolution of Sr, Y, and Zr: A Multiplicity of Nucleosynthetic Processes. *The Astrophysical Journal* **601**, 864–884.
- Trinquier A., Birck J. and Allegre C. J. (2007) Widespread  $^{54}\text{Cr}$  Heterogeneity in the Inner Solar system. *The Astrophysical Journal* **655**, 1179–1185.
- Trinquier A., Birck J.-L. and Allègre C. J. (2008) High-precision analysis of chromium isotopes in terrestrial and meteorite samples by thermal ionization mass spectrometry. *Journal of Analytical Atomic Spectroscopy* **23**, 1565.
- Trinquier A., Elliott T., Ulfbeck D., Coath C., Krot A. N. and Bizzarro M. (2009) Origin of Nucleosynthetic Isotope Heterogeneity in the Solar Protoplanetary Disk. *Science* **324**, 374–376.
- Urey H. C. (1952) *The Planets, Their Origin and Development.*, Yale University Press.
- Van Kooten E. M. M. E., Wielandt D., Schiller M., Nagashima K., Thomen A., Larsen K. K., Olsen M. B., Nordlund Å., Krot A. N. and Bizzarro M. (2016) Isotopic evidence for primordial molecular cloud material in metal-rich carbonaceous chondrites. *Proceedings of the National Academy of Sciences* **113**, 2011–2016.
- Walker R. J. (2009) Highly siderophile elements in the Earth, Moon and Mars: Update and implications for planetary accretion and differentiation. *Geochemistry* **69**, 101–125.
- Walsh K. J., Morbidelli A., Raymond S. N., O'Brien D. P. and Mandell A. M. (2011) A low mass for Mars from Jupiter's early gas-driven migration. *Nature* **475**, 206–209.
- Wang B., Moynier F. and Hu Y. (2024) Rubidium isotopic compositions of angrites controlled by extensive evaporation and partial recondensation. *Proc. Natl. Acad. Sci. U.S.A.* **121**, e2311402121.
- Wang G., Wu Y. and Xu J. (2016) Optimization techniques for improving the precision of isotopic analysis by thermal ionization mass spectrometry, taking strontium, neodymium, lead, and osmium as examples. *Spectroscopy Letters* **49**, 85–90.
- Warren P. H. (1985) The magma ocean concept and lunar evolution. *Annual Review of Earth and Planetary Sciences* **13**, 201–240.
- Warren P. H. (2011) Stable-isotopic anomalies and the accretionary assemblage of the Earth and Mars: A subordinate role for carbonaceous chondrites. *Earth and Planetary Science Letters* **311**, 93–100.
- Warren, P. H., and J. T. Wasson. (1979) Effects of pressure on the crystallization of a chondritic magma ocean and implications for the bulk composition of the moon. *Lunar and Planetary Science Conference, 10th, Houston, Proceedings.2* **10**, 2051–2083.
- Wasson J. T. and Kallemeyn G. W. (1988) The solar system: Chemistry as a key to its origin. *Geochimical Philosophical Transactions of the Royal Society of London. Series A, Mathematical and Physical Sciences et Cosmochimica Acta* **253**, 535–544.

- Weisberg M. K., McCoy T. J., Krot A. N. (2006) Systematics and evaluation of meteorite classification, in: Lauretta D. S., McSween Jr H. Y. (Eds.), Meteorites and the early solar system II. *University of Arizona Press, Tucson*, pp. 19–52.
- Wetherill, G.W. (1975) Late heavy bombardment of the moon and terrestrial planets. *Proceedings of the 6th Lunar Planetary Science Conference* **2**, 1539–1561.
- Wiechert U., Halliday A. N., Lee D.-C., Snyder G. A., Taylor L. A. and Rumble D. (2001) Oxygen Isotopes and the Moon-Forming Giant Impact. *Science* **294**, 345–348.
- Wise D. U. (1964) Origin of the Moon by Fission. In *The Earth-Moon System; Proceedings of an international conference held January 20-21 Plenum Press, New York, Goddard Space Flight Center, NASA*. p. 213.
- Wolf R. and Anders E. (1980) Moon and Earth: compositional differences inferred from siderophiles, volatiles, and alkalis in basalts. *Geochimica et Cosmochimica Acta* **44**, 2111–2124.
- Woo J. M. Y., Nesvorný D., Scora J. and Morbidelli A. (2024) Terrestrial planet formation from a ring: Long-term simulations accounting for the giant planet instability. *Icarus* **417**, 116109.
- Wood JA, Dickey JS Jr., Marvin UB, Powell BN. (1970). Lunar anorthosites and a geophysical model of the Moon. *Geochim. Cosmochim. Acta (Supp.)* **11** 965–88.
- Woosley S. E. and Heger A. (2007) Nucleosynthesis and remnants in massive stars of solar metallicity. *Physics Reports* **442**, 269–283.
- Woosley S. E. and Howard W. M. (1978) The p-processes in supernovae. *The Astrophysical Journal Supplement Series* **36**, 285–304.
- Yobregat E., Fitoussi C. and Bourdon B. (2017) A new method for TIMS high precision analysis of Ba and Sr isotopes for cosmochemical studies. *Journal of Analytical Atomic Spectroscopy* **32**, 1388–1399.
- Yokoyama T., Fukami Y., Okui W., Ito N. and Yamazaki H. (2015) Nucleosynthetic strontium isotope anomalies in carbonaceous chondrites. *Earth and Planetary Science Letters* **416**, 46–55.
- Youdin A. N. and Goodman J. (2005) Streaming Instabilities in Protoplanetary Disks. *The Astrophysical Journal* **620**, 459.
- Young E. D., Kohl I. E., Warren P. H., Rubie D. C., Jacobson S. A. and Morbidelli A. (2016) Oxygen isotopic evidence for vigorous mixing during the Moon-forming giant impact. *Science* **351**, 493–496.
- Zhang B., Lin Y., Moser D. E., Warren P. H., Hao J., Barker I. R., Shieh S. R. and Bouvier A. (2021) Timing of lunar Mg-suite magmatism constrained by SIMS U-Pb dating of Apollo norite 78238. *Earth and Planetary Science Letters* **569**, 117046.
- Zhang J., Dauphas N., Davis A. M., Leya I. and Fedkin A. (2012) The proto-Earth as a significant source of lunar material. *Nature Geoscience* **5**, 251–255.
- Zolensky M., Barrett R. and Browning L. (1993) Mineralogy and composition of matrix and chondrule rims in carbonaceous chondrites. *Geochimica et Cosmochimica Acta* **57**, 3123–3148.

## List of Figures

- Figure 1:** Meteorite classification scheme after Bischoff (2001). **17**
- Figure 2:** Plot of  $\epsilon^{54}\text{Cr}$  versus  $\epsilon^{50}\text{Ti}$  displaying the NC-CC dichotomy (Warren, 2011). Figure modified from Kleine et al. (2020). **19**
- Figure 3:** Qualitative model of the dynamical evolution of the early solar nebula that explains the relative observations from nucleosynthetic isotope variations in meteorites. Figure modified from Nanne et al. (2019). **21**
- Figure 4:** Schematic view of the structure of the solidified lunar magma ocean. The plagioclase floatation crust insulated the residual LMO and restrains cooling. Figure modified from Borg and Carlson (2023). **25**
- Figure 5:** The different Sr isotopes are created by different pathways. The s-process path is shown in bold black arrows, and the main path in dashed lines. Stable isotopes are shown in gray with regular outlines and unstable isotopes with dashed outlines and shaded gray. For Sr, pure *p*-process isotopes are shown in red, the *s*-process in blue, the *r*-process in green, and radioactive decay in orange. Figure modified from Liu et al. (2015). **28**
- Figure 6:** Schematic isochron diagram. Different minerals (open circles) evolve with different Rb/Sr ratios and form an isochron as displayed with the filled circles. **31**
- Figure 7:** Mass fractionation-corrected  $^{84}\text{Sr}/^{86}\text{Sr}$  (a) and  $^{87}\text{Sr}/^{86}\text{Sr}$  ratios (b) for the SRM 897 Sr standard for setups #1, #2, and #3. For each setup, results for static measurements from individual lines and the results of the corresponding dynamic measurements are shown. Squares denote static results for line 1, diamonds for line 2, and triangles for line 3. Dashed lines show the external reproducibility ( $\pm 2$  s.d.) of the dynamic measurements. Right vertical axes provide parts-per-million deviations of measured isotope ratios from the mean of the dynamic results. **43**
- Figure 8:** Mass fractionation-corrected  $^{84}\text{Sr}/^{86}\text{Sr}$  and  $^{87}\text{Sr}/^{86}\text{Sr}$  ratios for NIST SRM 987 measured with different magnet settings (Table 1) and using Faraday cups with extensive pre-usage (setup #1) and new cups (setup #2). Also shown are expected variations if the cup efficiency factor of the center cup is set to 0.9999, while the factor for all other cups is 1. These expected variations are in good agreement with the measured isotope ratios using

setup #1. Horizontal grey bands show dynamic results for  $^{84}\text{Sr}/^{86}\text{Sr}$  and  $^{87}\text{Sr}/^{86}\text{Sr}$  with their respective external reproducibility ( $\pm 2\text{s.d.}$ ). **44**

**Figure 9:** Comparison of  $^{84}\text{Sr}/^{86}\text{Sr}$  ratios for NIST SRM987 measured in this and in prior studies. Note the good agreement of the results except if  $^{86}\text{Sr}$  is collected in the center cup. Small crosses and bold line denote the modelled results from Figure 8. For details see text. **46**

**Figure 10:** Mass fractionation-corrected  $^{53}\text{Cr}/^{52}\text{Cr}$  (a) and  $^{54}\text{Cr}/^{52}\text{Cr}$  ratios (b) for the SRM 3112a Cr standard for static measurements using setup #1 and setup #2, and multi-static measurements using setup #3. Right vertical axes provide parts-per-million deviations of measured isotope ratios from the start of measurements using setup #2. **47**

**Figure 11:** Mass fractionation-corrected  $^{53}\text{Cr}/^{52}\text{Cr}$  and  $^{54}\text{Cr}/^{52}\text{Cr}$  ratios of NIST SRM 3112a from static measurements using setup #1 (a) and setup #2 (b, c). Note the strong correlation of  $^{53}\text{Cr}/^{52}\text{Cr}$  and  $^{54}\text{Cr}/^{52}\text{Cr}$  obtained using setup #1 (a), which disappears entirely for the initial measurements using setup #2 (2 months) (b), but reappears relatively quickly after (8 months) (c). (d) Multi-static mass fractionation-corrected  $^{53}\text{Cr}/^{52}\text{Cr}$  and  $^{54}\text{Cr}/^{52}\text{Cr}$  ratios for NIST SRM3112a measured using setup #2. As for the static measurements, there is residual correlation between  $^{53}\text{Cr}/^{52}\text{Cr}$  and  $^{54}\text{Cr}/^{52}\text{Cr}$ , but this correlation is of smaller magnitude and does not reflect a temporal change in the measured ratios. As such, this correlation is probably due to residual mass fractionation effects. The color-coding of the data points indicates the time of individual measurements for each setup, demonstrating that the correlation of  $^{53}\text{Cr}/^{52}\text{Cr}$  and  $^{54}\text{Cr}/^{52}\text{Cr}$  ratios reflects a temporal drift of both ratios to higher values over time. The axis lengths were adjusted to display equal ranges. **48**

**Figure 12:** Effect of changing Faraday cup efficiency on mass fractionation-corrected  $^{53}\text{Cr}/^{52}\text{Cr}$  and  $^{54}\text{Cr}/^{52}\text{Cr}$  ratios. Calculations assume that the cup efficiency of only the center cup changes and show that a factor of 0.9999, and 0.99995 instead of 1 results in a positive correlation between  $^{53}\text{Cr}/^{52}\text{Cr}$  and  $^{54}\text{Cr}/^{52}\text{Cr}$  ratios similar to the correlation observed. **49**

**Figure 13:** Average  $\mu^{84}\text{Sr}$  values of terrestrial, lunar, and meteoritic samples measured in this study. Uncertainties are 95% conf. for  $n \geq 4$  and 2 s.d. for  $n < 4$ . Grey box represents inner solar system average of  $\mu^{84}\text{Sr} = 5 \pm 4$  (95% conf.). Arrows indicate effect of excesses and deficits in  $s$ -,  $r$ -, and  $p$ -process Sr on  $\mu^{84}\text{Sr}$ . **60**

**Figure 14:** Schematic plots illustrating the mixing model of this study. a) Plot of  $\mu^{50}\text{Ti}$  vs.  $\mu^{54}\text{Cr}$  showing the location of the three components used in the mixing model:  $IC$ ,  $NC_{low}$ ,  $NC_{high}$ . Fractions  $f_{IC,NC}$  and  $f_{IC,CC}$  can be calculated by assuming that  $NC_{high}$  and CI are mixtures

of  $NC_{low}$  and  $IC$  (see text for details). b) Plot of  $\mu^{94}\text{Mo}$  vs.  $\Delta^{95}\text{Mo}$ . For definition of  $\Delta^{95}\text{Mo}$  see text. Variations in  $\Delta^{95}\text{Mo}$  reflect  $r$ -process variations, whereas variations in  $\mu^{94}\text{Mo}$  mostly reflect  $s$ -process variation. The position of the mixing endmembers  $IC$  and  $NC_{low}$  are indicated, as well as the resulting compositions of  $NC_{high}$  and  $CI$ . For details about the model see text. **63**

**Figure 15:** Fraction of  $IC$  material in the  $NC$  and  $CC$  reservoirs calculated using equations 7 and 9. Data used in these calculations are summarized in Table A3.1. **64**

**Figure 16:** Expected  $\mu^{84}\text{Sr}$  anomalies for enstatite chondrites ( $EC$ ), ordinary chondrites ( $OC$ ), angrites, and ureilites resulting from only  $s$ - and only ( $r$ -,  $p$ -)-process variations. These variations lead to  $\mu^{84}\text{Sr}$  variations of opposite sign but similar magnitude, and so no resolvable  $\mu^{84}\text{Sr}$  variations remain among  $NC$  meteorites. Measured  $\mu^{84}\text{Sr}$  values for  $EC$ ,  $OC$ , and angrites are shown for comparison and are well reproduced by the model. There are no  $\mu^{84}\text{Sr}$  data for ureilites, but they are also predicted to have  $\mu^{84}\text{Sr} \approx 0$ . Grey band represents the inner solar system average  $\mu^{84}\text{Sr} = 5 \pm 4$  (95% conf.). Data is summarized in Table A3.2. **65**

**Figure 17:**  $\text{Rb-Sr}$  isochron diagram for  $\text{FANs}$ . Reference isochrons were calculated using a bulk lunar  $^{87}\text{Rb}/^{86}\text{Sr} = 0.018$ , and relative to an age of 4.36 Ga for  $\text{FAN 60025}$ . **75**

**Figure 18:**  $\text{Rb-Sr}$  model ages for the time of Moon formation calculated for four different impact scenarios. No discrete peak is obtained for the canonical impact scenario, but all other scenarios provide a consistent Moon formation age of  $4.502 \pm 0.020$  Ga, or  $65 \pm 20$  Ma after solar system formation. **80**

## List of Tables

<b>Table 1:</b> Cup settings for Sr-isotopic measurements.	<b>40</b>
<b>Table 2:</b> Cup settings for Cr-isotopic measurements.	<b>42</b>
<b>Table 3:</b> Sr isotope data for terrestrial and lunar samples and meteorites.	<b>58</b>
<b>Table 4:</b> Rb-Sr isotopic data for ferroan anorthosites.	<b>74</b>
<b>Table 5:</b> Parameters for calculating Rb-Sr model ages.	<b>91</b>
<b>Table 6:</b> Parameters for $x_{\text{Theia}}$ and $f_{\text{Theia}}$ according to different impact models (Canup et al., 2023).	<b>92</b>
<b>Table 7:</b> Parameters for Rb/Sr of proto-Earth and Theia.	<b>92</b>



## Declaration of Author Contributions

Author contributions are listed for chapters of this thesis that are published, submitted, or in final preparation for submission to peer-reviewed scientific journals according to CRediT (Contributor Roles Taxonomy; <https://credit.niso.org/>).

### Chapter 2:

**Schneider, J. M.** and Kleine, T. (2024), Effects of Faraday cup deterioration on Sr and Cr isotope analysis by thermal ionization mass spectrometry. *Journal of Analytical Atomic Spectrometry*. submitted – under review

*Jonas M. Schneider:* Conceptualization, Formal analysis, Investigation, Methodology, Visualization, Writing – original draft, Writing – review & editing. *Thorsten Kleine:* Conceptualization, Funding acquisition, Project administration, Resources, Supervision, Writing – review & editing.

### Chapter 3:

**Schneider, J. M.**, Burkhardt, C., Kleine, T. (2023), *Distribution of s-, r-, and p-process Nuclides in the Early Solar system Inferred from Sr Isotope Anomalies in Meteorites*. *The Astrophysical Journal Letters*, 952: L25. <https://doi.org/10.3847/2041-8213/ace187>

*Jonas M. Schneider:* Conceptualization, Formal analysis, Investigation, Methodology, Visualization, Writing – original draft, Writing – review & editing. *Christoph Burkhardt:* Supervision, Investigation, Writing – review and editing *Thorsten Kleine:* Conceptualization, Funding acquisition, Project administration, Resources, Supervision, Writing – review & editing.

### Chapter 4:

**Schneider, J. M.**, and Kleine, T. (2024), *Strontium Isotopic Evidence for formation of the Moon ~ 4.5 billion years ago*. will be submitted to *Science Advances*

*Jonas M. Schneider:* Conceptualization, Data curation, Formal analysis, Investigation, Methodology, Software, Visualization, Writing – original draft, Writing – review & editing. *Thorsten Kleine:* Conceptualization, Formal Analysis, Funding acquisition, Project administration, Resources, Supervision, Writing – review & editing.



# Acknowledgements

Looking back a few years ago, I would never have thought I would be writing a doctoral thesis in cosmochemistry. This was only made possible with the help and support of several people, for which I am deeply grateful.

First of all, I would like to thank my supervisor Thorsten Kleine for introducing me to the field of cosmochemistry and entrusting me with a doctoral thesis in your group. When I started studying geoscience, I would have not expected to contribute to such a fascinating field of research, for example, working with Apollo samples. I especially want to say thank you for always being available for any kind of question, problem, discussion or doubt and always having an open door and ear – this is not a given. Your guidance helped me to keep the bigger picture in mind, while simultaneously placing value on the details. I have learned a lot during these years.

I also want to thank Christoph Burkhardt. You were always there for any kind of advice or help during my MSc and PhD. You introduced me to lab work, data processing, calculations, daily trouble-shooting and so much more. Your knowledge and your attitude made my PhD a lot more pleasant and my manuscripts a lot better. I will certainly miss a skate session in between conference talks with my supervisor.

Additional thanks go to Andreas Pack for taking over the task of being a referee of this thesis after our move to Göttingen and to the rest of my committee, especially Doris Breuer and Thomas Kruijer for making the journey for me – thank you! Also, I want to thank Erik Scherer for helping me with the Rb-Sr spike and all the people providing samples for this study, which include the Apollo 15&16 astronauts, NASA JSC, the Museum National d'histoire naturelle de Paris, the National History Museum London, and the Senckenbergmuseum.

I thank all the past and current cosmotopes! All of you contributed to this thesis through discussions or coffee (or beer) breaks, darts or pool, test talks or help in the lab. Thank you Timo, Jan H., Jan R., Emily, Quinn, Greg B., Greg A., Gerrit, David, Nina, Miles, Maxime, Shengyu, Aryavart, Matthias, Christian, Silvia and all of those I forgot. A very special thank you for making this thesis possible belongs to my fellow PhD buddies aka the rest of the 'trio infernale': Fridolin and Elias. I cannot understate, that you made this PhD a very memorable and joyful time in my life, I am not sure I would have made it without you two.

Furthermore, special thanks go to my parents for always encouraging and supporting me and enabling me to go my own way – I know I can always count on you. Finally, my greatest thanks go to Sarah. Thank you for always supporting me, for bringing so much joy into my life, and for trusting in me on so many levels. Life is just so much better with you.



# Curriculum Vitae

**Jonas Michel Schneider**

---

Date and place of birth: 24.08.1993, Stralsund

## Education

---

- 09/2022-06/2024 Max-Planck-Institut for Solar System Research Göttingen  
Universität Göttingen**  
*Doctoral Studies at the Department for Planetary Science, **continued***  
Thesis: 'High-precision Strontium Isotope Measurements - From the Early Solar system to the Age of the Moon'  
· *Integrated Research Training Group TRR 170  
'Late Accretion onto Terrestrial Planets'*  
· *International Max Planck Research School for Solar system Science at the University of Göttingen (IMPRS)*
- 04/2019-09/2022 Universität Münster**  
*Doctoral Studies at the Institute for Planetology*  
Thesis: 'High-precision Strontium Isotope Measurements - From the Early Solar system to the Age of the Moon'  
· *Integrated Research Training Group TRR 170  
'Late Accretion onto Terrestrial Planets'*
- 10/2016 - 01/2019 Universität Münster**  
*Master of Science*  
Thesis: 'Early Solar system Dynamics as inferred from Chromium Isotopes in individual Chondrules'
- 02/2018 - 07/2018 Adam Mickiewicz University Poznan, Poland**  
Erasmus+ stipendium
- 10/2013 - 09/2016 Universität Münster**  
*Bachelor of Science*  
Thesis: 'The sedimentary Sulfur Cycle in the Benguela Upwelling System - a multiple Sulfur Isotope Study'
- 06/2012 Johanneum zu Lübeck**  
*Abitur*

## Peer Reviewed Publications

---

**Schneider, J. M.** and Kleine, T. (2024), *Effects of Faraday cup deterioration on Sr and Cr isotope analysis in thermal ionization mass spectrometry*. Journal of Analytical Atomic Spectrometry. *under review*

Jansen C. A., Burkhardt C., Marrocchi Y., **Schneider J. M.**, Wölfer E. and Kleine T. (2024) *Condensate evolution in the solar nebula inferred from combined Cr, Ti, and O isotope analyses of amoeboid olivine aggregates*. Earth and Planetary Science Letters 627, 118567. [doi.org/10.1016/j.epsl.2024.118567](https://doi.org/10.1016/j.epsl.2024.118567)

**Schneider, J. M.**, Burkhardt, C., Kleine, T. (2023), *Distribution of s-, r-, and p-process Nuclides in the Early Solar system Inferred from Sr Isotope Anomalies in Meteorites*. The Astrophysical Journal Letters, 952: L25. [doi.org/10.3847/2041-8213/ace187](https://doi.org/10.3847/2041-8213/ace187)

Hellmann, J.L., **Schneider, J. M.**, Wölfer, E., Jansen, C.A., Drazkowska, J., Hopp, T., Burkhardt, C. Kleine, T., (2023), *Accretion of Carbonaceous Chondrites in a Pressure Bump of a Structured Proto-planetary Disk*. The Astrophysical Journal Letters 946: L34. [doi.org/10.3847/2041-8213/acc102](https://doi.org/10.3847/2041-8213/acc102)

Windmill, R. J., Franchi, I. A., Hellmann, J. L., **Schneider, J. M.**, Spitzer, F., Kleine, T., Greenwood, R. C., Anand, M. (2022), *Isotopic evidence for pallasite formation by impact mixing of olivine and metal during the first 10 million years of the Solar system*. PNAS Nexus, (1), 1–11. [doi.org/10.1093/pnasnexus/pgac015](https://doi.org/10.1093/pnasnexus/pgac015)

Metzler, K., Hezel, D. C., Barosch, J., Wölfer, E., **Schneider, J. M.**, Hellmann, J. L., Berndt, J., Stracke, A., Gattacceca, J., Greenwood, R. C., Franchi, I. A., Burkhardt, C., Kleine, T. (2021), *The Loongana (CL) group of carbonaceous chondrites*. Geochimica et Cosmochimica Acta, 304, 1–31. [doi.org/10.1016/j.gca.2021.04.007](https://doi.org/10.1016/j.gca.2021.04.007)

**Schneider, J. M.**, Burkhardt, C., Marrocchi, Y., Brennecka, G. A., Kleine, T. (2020), *Early evolution of the solar accretion disk inferred from Cr-Ti-O isotopes in individual chondrules*. Earth and Planetary Science Letters, 551, 116585. [doi.org/10.1016/j.epsl.2020.116585](https://doi.org/10.1016/j.epsl.2020.116585)

## Conference Contributions

---

Burkhardt, C., Jansen, C., Marrocchi, Y., Villeneuve, J., Wölfer, E., **Schneider, J.M.**, Kleine, T. (2024), *Isotope genealogy and Al-Mg chronology of individual OC chondrules*. Metsoc Conference, Brussels.

**Schneider, J.M.**, Kleine, T. (2024), *Chronology of lunar crust formation inferred from Rb-Sr systematics of ferroan anorthosites*. 55<sup>th</sup> Lunar and Planetary Science Conference, Houston, Abstract #1456.

**Schneider, J.M.** Burkhardt, C., Kleine, T. (2023), *Origin of Strontium-84 homogeneity in the inner solar system*. Goldschmidt Conference, Lyon.

Burkhardt, C., Jansen, C., Marrocchi, Y., **Schneider, J.M.**, Wölfer, E., Kleine, T. (2023), *Isotopic evidence for a common origin of CAIs and AOAs*. Goldschmidt Conference, Lyon.

**Schneider, J.M.**, Burkhardt, C., Kleine, T. (2022), *Strontium-84 homogeneity of the inner solar system*. MetSoc Conference, Glasgow.

**Schneider, J.M.**, Burkhardt, C., Kleine, T. (2022), *Strontium-84 anomalies in the early solar system revisited*. 53<sup>rd</sup> Lunar and Planetary Science Conference, Houston, Abstract #2494.

Wölfer, E., Burkhardt, C., **Schneider, J.M.**, Budde, G., Kleine, T. (2021), *Dynamic evolution of the solar system inferred from Ti, Cr, and Mo isotope anomalies in meteorites*. 53<sup>rd</sup> Lunar and Planetary Science Conference, Houston, Abstract #2468.

**Schneider, J.M.** and Kleine, T. (2021), *Terrestrial planet formation inferred from Sr isotope anomalies in meteorites*. Goldschmidt Conference, Lyon.

**Schneider, J.M.**, Burkhardt, C., Brennecka, G.A., Kleine, T. (2019), *Complex mixing of nebular materials from combined O-Ti-Cr isotope variations in individual chondrules*. Paneth Colloquium, Nördlingen.

**Schneider, J.M.**, Burkhardt, C., Brennecka, G.A., Kleine, T. (2019), *Insights to early solar system mixing dynamics from chromium and titanium isotope systematics in individual chondrules*. 50<sup>th</sup> Lunar and Planetary Science Conference, Houston, Abstract #2303.

**Schneider, J.M.**, Burkhardt, C., Brennecka, G.A., Kleine, T. (2019), *Early Solar system dynamics inferred from nucleosynthetic anomalies in individual chondrules*. Goldschmidt Conference, Barcelona.